PHYSIK-DEPARTMENT

Photoresponsive Molecular Architectures at Interfaces

Doktorarbeit

von

Juan Li

TECHNISCHE UNIVERSITÄT MÜNCHEN

TECHNISCHE UNIVERSITÄT MÜNCHEN

Lehrstuhl E20-

Molekulare Nanowissenschaften & Chemische Physik von Grenzflächen

Photoresponsive Molecular Architectures at Interfaces

Juan Li

Vollstädiger Abdruck der von der Fakultät für Physik der Technischen Universität München zur Erlangung des akademischen Grades eines Doktors der Naturwissenschaften (Dr. rer. nat.) genehmigten Dissertation.

Vorsitzender:		Univ. -Prof. Dr. Michael Knap
Prüfer der Dissertation:	1.	Univ. -Prof. Dr. Johannes Barth
	2.	Univ. -Prof. Dr. Reinhard Kienberger

Die Promotion wurde am 22. 03. 2016 bei der Technischen Universität München eingereicht und durch die Fakultät für Physik am 07. 04. 2016 angenommen.

路漫漫其修远兮，吾将上下而求索。

“The road ahead will be long and our climb will be steep.”

Qu Yuan (340-278 BC)

Abstract

Highly crystalline natural-occurring and synthetic two-dimensional materials (2DMs) present intriguing features for emerging organic/inorganic hybrid architectures.

In this thesis, we demonstrate the fabrication and characterization of complex 2DM-based device elements. Specifically, we combine molecular assemblies with graphene or molybdenum disulfide (MoS_2) 2DMs to afford complex photoresponsive nanosystems. We initially self-assemble a bicomponent supramolecular network on a transparent graphene-decorated diamond platform. Subsequently, a larger conjugated molecule, a terrylene-based dye, is employed in a molecular network configuration and the photoresponse of the supramolecular assembly is readily recorded by means of a modified scanning tunneling microscope (STM). Finally, we employ a photoswitchable self-assembled monolayer anchored on a gold substrate to electronically switch the transport properties of molybdenum disulfide (MoS_2). Because molecular architectures on 2D platforms provide a route to precisely organize different functional units at well-defined interfaces, our achievements contribute to the emerging field of molecularly precise optoelectronic technology and devices.

Kurzzusammenfassung

Hochkristalline, sowohl natürlich vorkommende und künstlich hergestellte zweidimensionale Materialien (2DMs) zeigen interessante Eigenschaften, insbesondere für organisch/anorganisch hybride Strukturen.

In der vorliegenden Arbeit wird die Herstellung und Charakterisierung von komplexen 2DM-basierten Bauelementen dargestellt. Durch molekulare Selbstorganisierung entstehen diese photoempfindlichen Nanosysteme auf Graphen oder Molybdändisulfid. Zuerst wird ein Netzwerk aus zwei Komponenten, auf einem transparenten, mit Graphen beschichteten Diamanten gebildet. Im nächsten Schritt wird ein höher konjugiertes Molekül, ein terrylenbasierter Farbstoff, in der molekularen Netzwerkanordnung verwendet. Der entstehende Photostrom dieses supramolekularen Netzwerkes wird mit einem modifizierten Rastertunnelmikroskop gemessen. Abschließend wird eine photoschaltbare selbstorganisierende Monolage an einem Goldsubstrat verankert, um die Transporteigenschaften von Molybdändisulfid elektronisch zu verändern. Molekulare Strukturen auf zweidimensionalen Substraten bieten eine neue Möglichkeit um funktionelle Gruppen auf klar definierten Grenzflächen anzuordnen. Die Ergebnisse leisten einen Beitrag im Bereich molekular präziser optoelektronischer Bauteile und den damit in Zusammenhang stehenden Technologien.

Contents

Chapter 1

Introduction

Nature employs self-assembly to fabricate the most complex molecularly precise machinery known to man. Extended heteromolecular architectures[1] provide a route to spatially organize different building blocks relative to each other, enabling synthetic molecularly precise fabrication[2]. Such emerging technology is expected to lay the foundations for a new generation of device elements, where active constituents are fabricated not only with high interfacial and chemical control but also with exquisite spatio-temporal precision. The aim of this thesis is to demonstrate proof-of-principle optoelectronic function from molecular architectures at interfaces, whose spatial precision has been *a priori* characterized through scanning tunneling microscope (STM) and atomic force microscope (AFM).

Chapter 1 briefly introduces the related interfacial chemistry and physics fields consisting of preparation of molecular architectures (section 1.1), scanning probe microscope (section 1.2) and molecular optoelectronic device elements (section 1.3). In section 1.1, the concepts of supramolecular self-assembly and multicomponent molecular architectures, especially surface-confined molecular systems are presented. In section 1.2, an insight into the development and principle of the scanning probe technology referring to scanning tunneling microscope (section 1.2.1) and atomic force microscope (section 1.2.2) are given. Subsequently section 1.3 broadly introduces molecular devices toward to advanced optoelectronics of prototype molecularly precise devices. The structures and potential prospects of molecular photovoltaics (section 1.3.1), especially based on organic molecules and molecular photoswitches (section 1.3.2) are discussed as representatives in this field.

Chapter 2 gives a detailed description of the interfacial materials and methods. It consists of three main parts: substrates (section 2.1), adsorbates (section 2.2) and transistor device fabrication (section 2.3). Firstly the properties and processing methods of five different substrates used in this thesis are introduced. Secondly the molecular adsorbates employing for self-assembly and substrate functionalization are discussed in the areas of chemical synthesis and characterization by scanning probe microscope (STM). Thirdly the consecutive process to fabricate a transistor device based on self-assembled monolayer and monolayer 2D materials are described in details.

Chapter 3 discusses the characterization of bicomponent supramolecular network on an all carbon transparent platform. The morphology and mechanism of the network based on melamine and naphthalenetetracarboxylic diimide (NTCDI) are investigated through scanning tunneling microscope (STM) at the solid-liquid interface.

Chapter 4 addresses the self-assembled supramolecular system based on terrylene diimide (TDI) towards advanced photovoltaics devices. The photocurrent response is characterized by scanning tunneling spectroscopy (STS).

Chapter 5 introduces a 2D semiconductor and self-assembled monolayer (MoS_2-azobenzene) photoswitchable diode device. The electrical characterizations of the MoS_2-azobenzene-Au hybrid system are discussed and elaborated through conductive atomic force microscope (c-AFM) and kelvin probe force microscope (KPFM).

At last, in Chapter 6, the thesis ends with a summary and perspectives.

1.1 Surface-confined molecular architectures

The areas of nanoscience and nanotechnology have been experiencing exponential growth in the past decades. One of the promising routes to electronic devices in nanometer scale is the autonomous ordering and assembly of atoms and molecules on well-defined substrates. Common to all bottom-up strategies for the fabrication of nanostructures at surfaces, they are centered around guided assembly phenomena. Atoms or molecules or both of them are deposited on the substrate in different conditions (in vacuum, ambient atmosphere or solution) and nanometer-scale structures evolve as a result of a multitude of atomistic processes.[1] A major advantage of molecular self-assembly at interfaces is that the molecular layer can have a variety of structures and potential functionalities on many length scales, depending on the choice of building blocks. Two-dimensionally (2D) extended, crystalline supramolecular[3, 4] or covalent[5-8] multicomponent architectures represent ideal systems for testing the foundations of modular three-dimensional (3D) architectonic at well-defined interfaces[9, 10]. One commonality of these complex highly correlated materials is that they are giant (supra)molecules or massive (multicomponent) molecular architectures (MMAs) for general. MMAs are by-design matter with a defined, yet complex multi-elemental chemical formula and high molecular weights. The advantage of borrowing concepts from 2D polymers[11, 12], crystal engineering[13] and molecular tectonics[14] to define a common set of complex and artificial materials as massive molecular entities with a defined chemical formula is simple: anticipating the smallest functional scale of technology, a defined connectivity, stoichiometry and geometry at the atomic level impacts the function of the entire architecture. Figure 1.1 shows three different functional surface-confined molecular architectures towards molecularly precise technology.

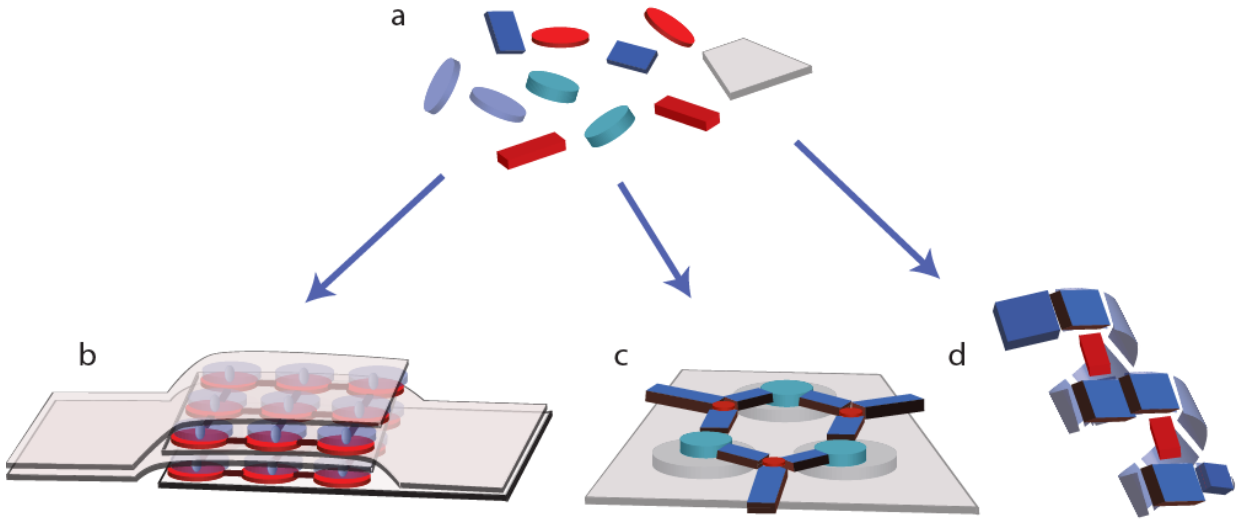

Figure 1.1 Scheme of molecularly precise technology. (a) Modular molecular components assemble to form massive molecular architectures (MMAs) leading to several molecularly precise devices. (b) A tandem bilayer donor-acceptor photovoltaic device. (c) A half-adder device. (d) A piezoelectric actuator.

Nowadays, the self-assembly of artificial architectures is widely studied at solid-liquid and solid-vacuum interfaces. The former interface is of special interest because of its accessible sample preparation and its analogy to biological processes: upon adsorption at interfaces, (supra) molecules undergo spontaneous assembly to produce functional architectures. The thesis aims at large-area, artificial molecularly precise devices fabrication which are assembled by molecular architectures from the bottom-up[15] on different substrates. Self-assembled supramolecular[16, 17], metal-organic[18] or covalent[19] multi-component surface-confined networks have already provided a route to organize different building blocks relative to each other very precisely in two dimensions (2D). These 2D surface assemblies can be engineered[1, 20] with increasing prediction[21, 22] level for self-fabrication on specific substrates. In addition, 2D networks can act as a basic template for the growth of 3D networks[23], paving the road towards vertical heteromolecular control by means of monolayer-by-monolayer assembly and growth. In fact, such architectures can feature interpenetrated morphologies[24] with ideal specific nanoporous and columnar order, which have been considered optimal configurations and expected for organic solar cells[25].

Moreover, besides engineering of molecular architectures, the substrates can be also tailored to provide other specific functional properties for fabricating the whole devices.

Among the diverse surface-confined molecular architectures, we concentrate on novel molecular porous networks which have potential applications in electronics[26, 27], optoelectronics[28, 29] and energy storage[30, 31]. Two-dimensional molecular porous networks are mostly constructed by organic molecules with various functional groups. They represent a family of model systems possessing different types of voids and symmetries that can be further utilized to engraft sophisticated ensembles. It is known that porous networks have many potential applications, such as templates to host guest species for molecular photovoltaics or chemical and biological sensors and so on. The controllability, predictability, stability and applicability of these porous networks are associated with the grand challenges of molecular devices.[32] The assembling process at interface can be carried out either under ultrahigh vacuum conditions or in the liquid under ambient conditions. The formation of molecular networks results from balanced interactions between molecule and molecule, molecule and substrate, molecule and solvent. In this respect, hydrogen bonds have been intensely scrutinized due to their universal presence in natural chemical structures and significance in supramolecular systems.[33] Therefore, in this work the supramolecular structures we studied are all formed by hydrogen bonding which provides both high selectivity and directionality[34] for functional molecular architecture fabrication. It has been demonstrated that hydrogen-bonded architectures are especially prominent in solution, molecular crystals and two-dimensional self-assembly.[3, 35-39] For instance, as shown in Figure 1.2, model hydrogen bonds, e.g. (COOH···H)[40-43] or (N···H)[44-46], have been widely employed. Some of these novel supramolecular nanostructures are generated at different surfaces on the basis of this concept.[16, 20, 47-51]

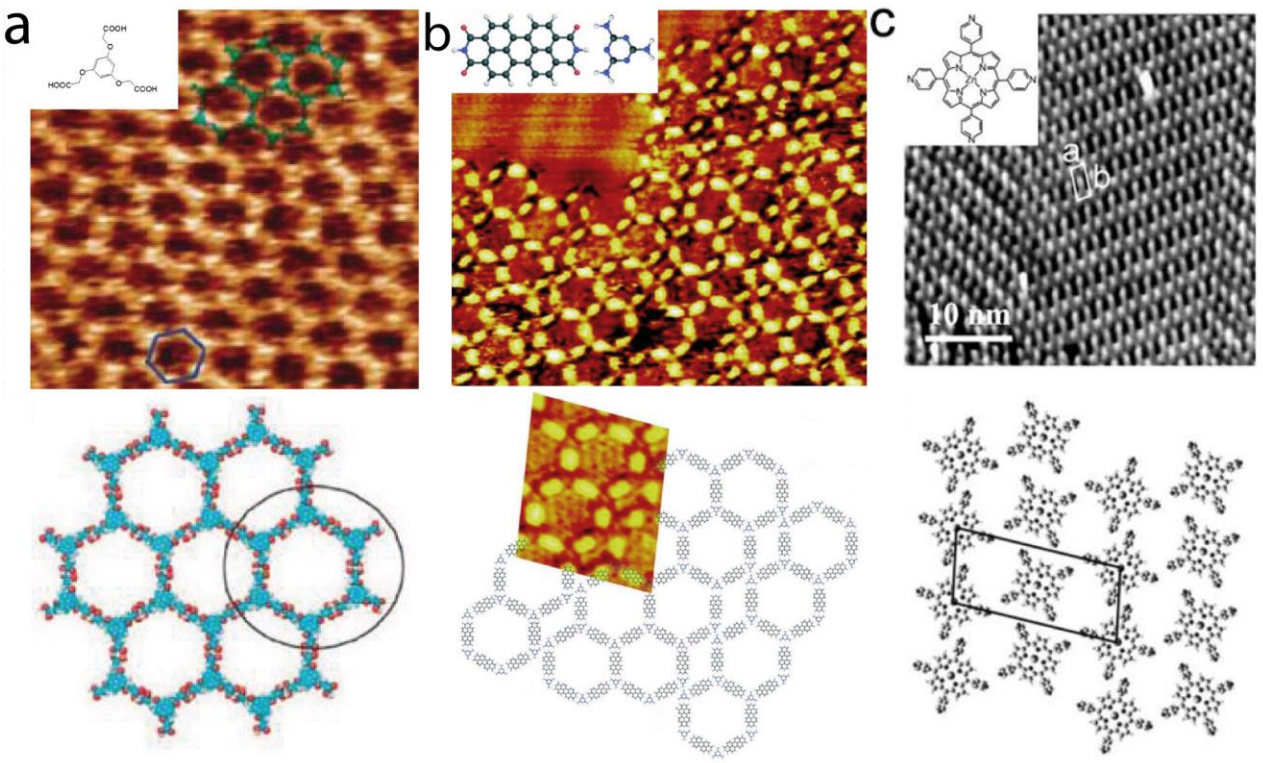

Figure 1.2 Examples of networks formed by hydrogen bonds and the corresponding molecular models. (a) Hydrogen bonded network of 1,3,5-tris(carboxymethoxy)-benzene (TCMB) on HOPG surface.[43] (b) Hydrogen bonded network of perylenetetracarboxylic diimide (PTCDI)-melamine on an Au(111) surface.[46] (c) Network of zinc-5,10,15,20-tetra(4-pyridyl)porphyrin on an Au(111) surface.[44]

1.2 Scanning probe microscopes

Scanning probe microscopy (SPM) comprises a large and growing collection of techniques to investigate the properties of a sample, at or near the sample surface. The SPM instrument has a sharp probe (with radius of curvature typically in the nanometer or tens of nanometer range) that is in near-contact, intermittent contact, or perpetual contact with the sample surface. In SPM techniques, the sharp probe (tip) is scanned across a sample surface. Alternative, the surface is

scanned beneath the tip. Interactions between the tip and sample are detected and mapped. Different techniques sense different interactions, which can be used to describe surface topography, adhesion, elasticity, electrostatic charge, etc. In this work, scanning tunneling microscope (STM) and atomic force microscope (AFM) are the main characterization techniques which will be used for investigating supramolecular self-assemblies and molecular electronics.

1.2.1 Scanning tunneling microscope

The earliest, widely-adopted SPM technique is scanning tunneling microscope (STM) which was invented by Binnig and Rohrer.[52, 53] Scanning tunneling microscope (STM) is a surface science instrument that provides imaging with atomic-scale resolution at interfaces under vacuum, air, water and various other surroundings. In STM, a bias voltage is applied between a sharp conducting tip and the sample. When the tip approaches the sample, electrons tunnel through the narrow gap, either from the sample to the tip or vice versa, depending on the bias voltage. Changes of only 0.1 nm in the separation distance between tip and sample can cause an order of magnitude difference in the tunneling current, giving STM a remarkably high precision.[54] Figure 1.3 shows a schematic of its essential elements. A probe tip, usually made of tungsten (W) or platinum-iridium (Pt-Ir) alloy, is attached to a piezo tube which consists of three mutually perpendicular piezoelectric transducers: x piezo, y piezo and z piezo. Upon applying a voltage, a piezoelectric transducer expands or contracts. By applying a sawtooth voltage on the x piezo and a voltage ramp on the y piezo, the tip scans on the xy plane. Then taking advantage of the coarse positioner and the z piezo, the tip and the sample are brought into the place within a fraction of a nanometer gap.[54, 55]

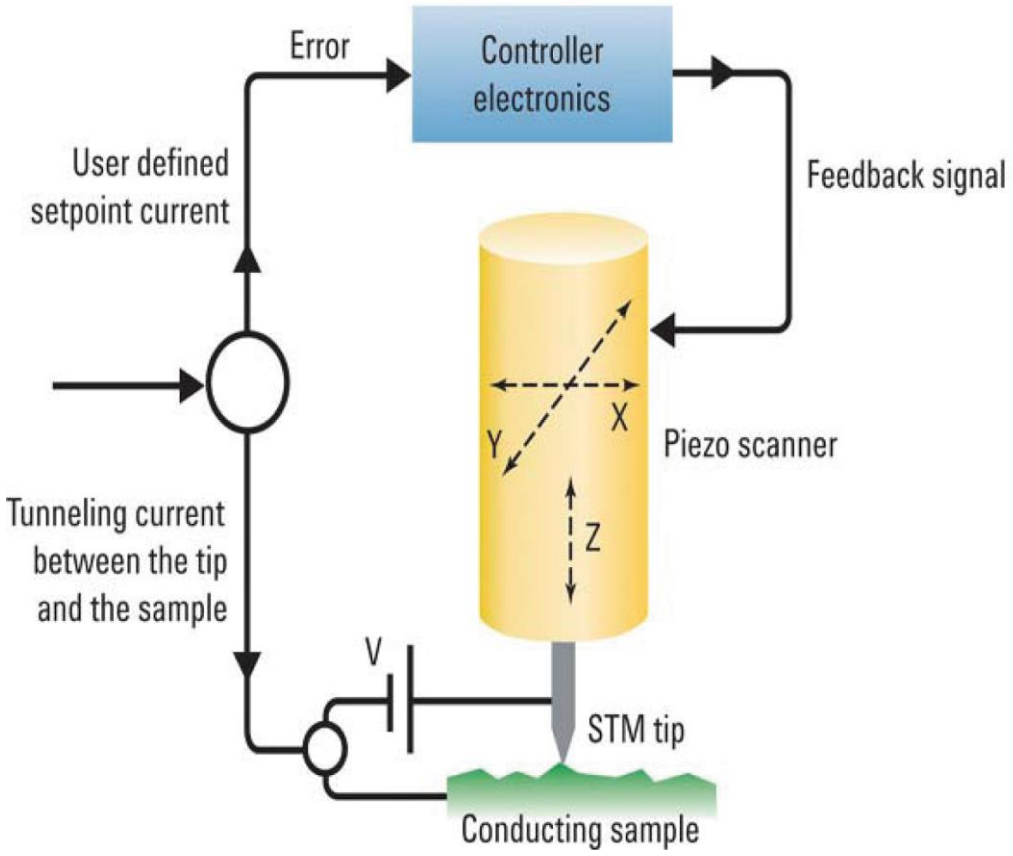

Figure 1.3 Basic STM schematic.[55]

By means of x piezo and y piezo, the tip scans over the sample surface line by line. According to whether the feedback loop controlling the z piezo is enabled or not, the STM may be operated in two different modes: the constant current mode and the constant height mode (shown in Figure 1.4 respectively). In constant current mode, the tunneling current (and thus the gap width between tip and sample) is always kept constant at a preset setpoint value under the feedback control circuit. Since the current is also proportionally related to the local density of states (DOS) of the surface, the tip follows a convolution between the height and DOS contour during scanning. Subsequently the topographic image of the surface is generated by recording the vertical position of the tip. In the constant height mode, the feedback loop is turned off and hence the vertical position of the tip is fixed accordingly. The tunneling current as a function of its lateral position represents the surface image. Moreover, in this mode, a prominent advantage is

that STM can be operated at a high scanning frequency to obtain higher resolution images compared with the constant current mode. However, the sample surface has to be relatively even and clear of dislocation defects to prevent the tip from colliding with the surface.

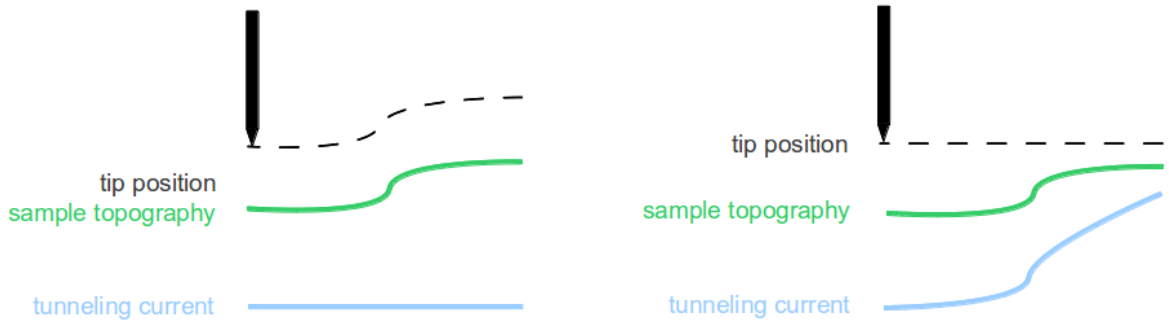

Figure 1.4 Illustration of constant current (left) and constant height (right) STM modes.[56, 57]

The underlying basic physics of STM is quantum tunneling[54, 58] - a quantum mechanical phenomenon, where a particle passes a potential barrier which has a higher energy than its own, and is, therefore, classically not expected to be surmounted. In quantum mechanics, in regions where $E < U(z)$ (Figure 1.5), an electron is described by a wave function $\psi(z)$, which satisfies the Schrödinger equation

$$-\frac{\hbar^2}{2m}\frac{d^2}{dz^2}\Psi(z) + U(z)\Psi(z) = E\Psi(z) \tag{1.1}$$

where m is the electron mass, E is the energy of the electron and $\hbar$ is the reduced Planck constant. Considering the forbidden region inside the potential barrier, where $U(z) > E$, the solution of the Schrödinger equation is

$$\Psi(z) = \Psi(0)e^{\pm kz} \tag{1.2}$$

where

$$k = \frac{\sqrt{2m(U-E)}}{\hbar} \tag{1.3}$$

which is the decay constant. This equation describes the electron's wave function decaying exponentially with *z* inside the potential barrier. Moreover, it shows that the electron may penetrate the potential barrier. The probability of the electron inside the barrier is given by

$$P = |\Psi(z)|^2 = |\Psi(0)|^2 e^{2kz} \tag{1.4}$$

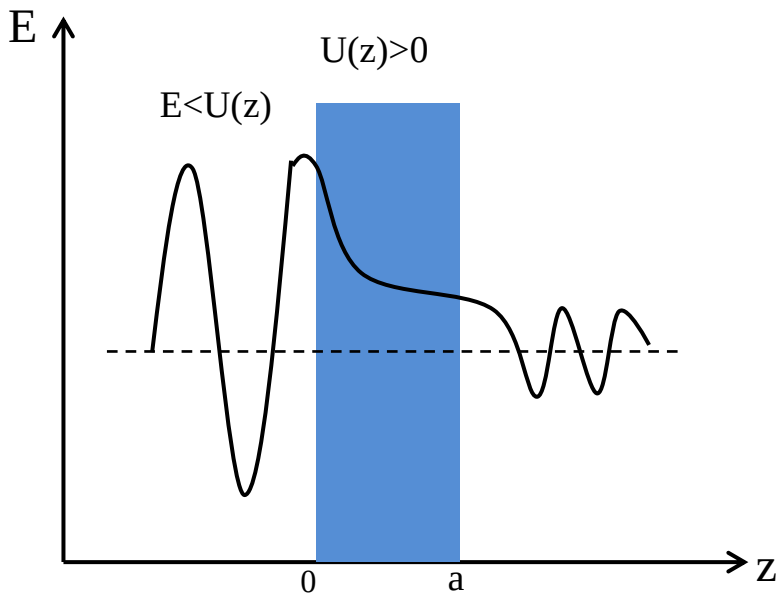

Figure 1.5 Sketch of an electron wave function with the energy *E* tunneling through a potential barrier of *E* < *U(z)* in quantum mechanics.[54]

We can explain some basic features of metal-vacuum-metal tunneling as depicted in Figure 1.6. For a metal surface, the minimum energy required to remove an electron from the bulk to the vacuum level is defined as the work function ϕ. The Fermi energy is thus $E_F = -\phi$.[54] The work functions of sample material and tip are assumed to be the same, their chemical potentials being in equilibrium through the external circuit. When applying a voltage *V*, it leads to a net tunneling

current. Hence, as the probability of an electron to tunnel from sample to tip, summing up over all sample states between E_F - eV_b and E_F leads to the formulation for the tunneling current

$$I_t \propto \sum_{E_F - eV_b}^{E_F} |\phi_n(z)|^2 \tag{1.5}$$

Assuming a constant local density of states (LDOS) for the tip as well as low voltages and $T = 0$, in this case I_t can be written as

$$I_t \propto V\rho(0, E_F)e^{-2ka} = V\rho(0, E_F)e^{\frac{-2d\sqrt{2m\Phi}}{\hbar}} \tag{1.6}$$

where $\rho(z, E_F)$ is the local density of states (LDOS). It is obvious that the tunneling current is directly proportional to voltage and the LDOS, but it exponentially depends on the distance between sample and tip. Accordingly, retracting the tip from the sample approximately one Ångström can lead to an order of magnitude decrease in the tunneling current. Thus, it is very sensitive to the tip-sample distance or rather the change between the distances.

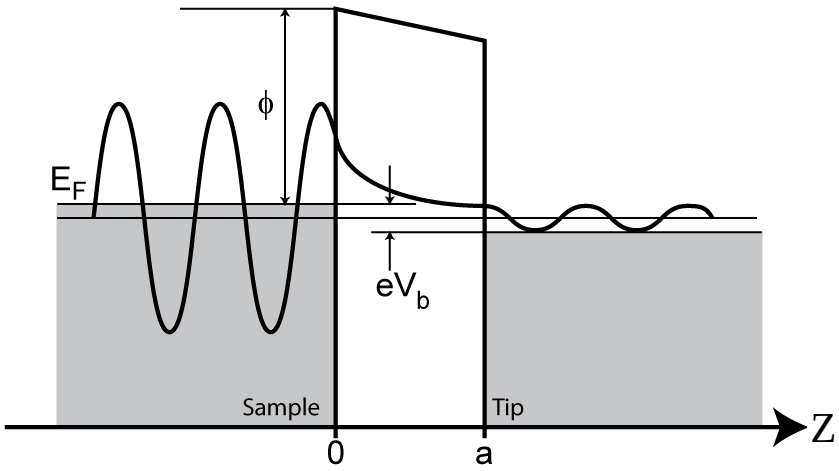

Figure 1.6 A one-dimensional metal-vacuum-metal tunneling junction. The sample and the tip are modeled as semi-infinite pieces of free-electron metal. The vacuum tail of a sample state can penetrate into the region of the tip when the distance between sample and tip is small enough.[54]

When the formalism of Bardeen[59] is taken into account, tip and sample have different wave functions and there is a matrix element, which describes the overlap of the two wave functions at a separation surface. Evaluating the matrix element by employing the ansatz of Tersoff and Hamann[60] leads to a correlation in which the main tip state involved in the tunneling process is an s-state and the two wave functions do not influence each other. For small bias voltage V, the tunneling current I_t is directly proportional to the LDOS of the sample.

$$I_t \propto V e^{-2kR} \rho_t(E_F) \rho_s(E_F, r_0) \tag{1.7}$$

with

$$k = \frac{\sqrt{2m\Phi_t}}{\hbar} \tag{1.8}$$

where R is the tip radius, ϕ_t is the barrier height and r_0 is the position of the center of the tip's curvature. The last equation of the tunneling current implies that the information shown in a STM image is not only obtained from the LDOS and the topography of the sample, but also from the LDOS and the shape of the tip.

By means of STM another powerful technique to investigate the properties of a surface is scanning tunneling spectroscopy (STS). When the feedback is turned off, the separation gap between tip and surface is fixed and the resulting tunneling current is recorded while the bias voltage is varied. The change of tunneling current is a necessary parameter for investigating the LDOS. From these *IV* (tunneling current at corresponding bias voltage) curves, the normalized derivative $(dI/dV)/(I/V)$ can be calculated: assuming the transmission probability and the tip density of states to be nearly constant, one can estimate the local density of states of the sample to be proportional to the tunneling conductance (the increase of tunneling current with voltage). Hence the normalized derivative is

$$\frac{dI_t}{dV} \propto \rho_s(E_F - eV) \tag{1.9}$$

The tunneling current in STM flows in a region with a diameter of only a few Ångströms[61] - tiny compared to other surface spectroscopy techniques which average over a large surface region. Hence the tip can be placed directly over a molecule so as to allow the selective study of its electronic properties like HOMO-LUMO energy gap, band bending and chemical bonding.

1.2.2 Atomic force microscope

Motivated by the observation of atomic forces in STM experiments and its visible influence on the images, Binnig, Quate, and Gerber introduced an instrument similar to the STM, the atomic force microscope (AFM) for resolving individual atoms on conductive or nonconductive surfaces.[54] The technique makes it possible to image *in-situ*, in liquid, under controlled temperature and in other controlled environments as well.

The conventional working principle of AFM, as shown in Figure 1.7, consists on a sharp tip at the free end of a cantilever (the "probe") which is brought into contact with the surface of sample. The cantilever is bended once the tip interacts with the surface. The interaction of the tip with the sample is recorded through movement of the cantilever. A laser spot is reflected from the cantilever onto a position-sensitive photodiode detector. As the cantilever bends, the position of the laser spot also changes. The cantilever typically has a low force constant which allows for precise control of the force between the tip and sample[62]. The shapes of cantilever can be either rectangular or triangular and the typical material is silicon or silicon nitride. The mechanical properties of cantilevers are characterized by the spring constant and the resonance frequency. The top side is coated with a reflective material such as gold or aluminum to increase the reflectivity of the laser into the photodiode. Similar to the current-image mode in STM, the AFM can also be operated in force-image mode. There are two definitions of force spectroscopy: distance-dependent or bias-voltage dependent force spectroscopy.

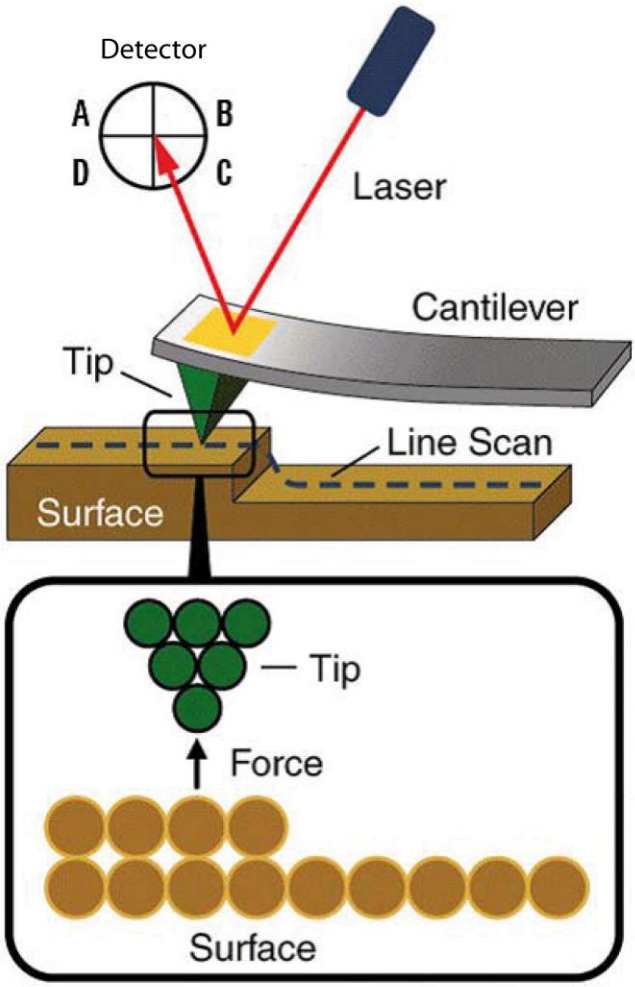

Figure 1.7 Basic AFM principles.[55]

The interactive forces (van-der-Waals, electrostatic or Pauli repulsion forces) between the tip and the surface shown in Figure 1.8 can be either attractive or repulsive depending on the distance between tip and surface. At the right side of the curve, the tip and sample are separated by large distance within an area of no interaction. As they approach, first the tip is attracted by the surface due to, e.g. a dipole-dipole interaction. This zone of interaction is known as the "non-contact" regime. As they go closer still, in the "intermittent contact" regime, the repulsive force predominates. The forces balance and the net force drops to zero when the distance between tip and sample is just a few Ångströms. When the total force becomes positive (repulsive), the atoms

are in the "contact" regime.[55] The van-der-Waals potential energy of two atoms, located at a distance *r* from each other, can be modeled according to a Lennard-Jones potential[63]

$$U(r) = \alpha\left(\frac{1}{r^6} - \frac{1}{r^{12}}\right) \tag{1.10}$$

The theory of Lennard-Jones potential allows estimating the interaction force of a tip with a sample. Adding elementary interactions for all of the tip and sample atoms, the energy of the tip-sample system can be derived.

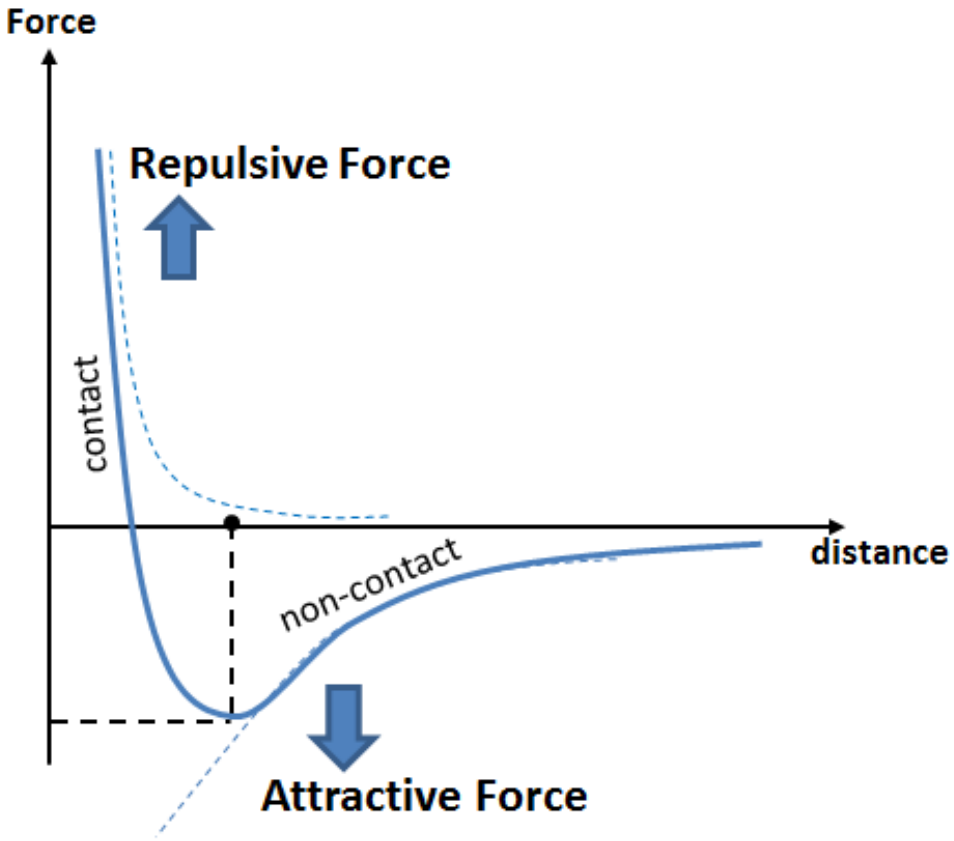

Figure 1.8 Regimes of attractive and repulsive force interactions as the tip approaches the sample.

The basic AFM operation modes include contact mode and intermittent contact mode as shown in Figure 1.9. In contact mode, the AFM tip is attached to the end of a cantilever with a low spring constant with the typical value of 0.001 - 5 nN/nm[55]. The tip makes gentle contact

with the sample in close repulsive contact with the surface of the sample. The scanner features on top of the sample causes the cantilever bending due to the changes in topography or the probe-sample forces. AFM can be conducted in either constant force or constant height modes. In constant force mode, the feedback loop keeps the cantilever deflection constant by adjusting the height of the sample. The height is fluctuated by extending or retracting the piezo along the z axis. The output of the feedback circuit is used to generate the topography image. In constant height mode, the height of the surface is kept constant and the cantilever deflection is monitored. Constant height mode is often used for two cases: generating atomic-resolution images of atomically flat surfaces where the cantilever deflections are small and recording real-time images of changing surfaces where high scan speed is essential. Constant force mode is more typically used than constant height mode as it is able to image surface within a greater height variability. However the speed of scanning is limited by the response time of the feedback circuit. Because of the inherent noise in the piezo feedback circuit, the resolution of this mode is also lower than constant height mode.

Intermittent contact mode AFM is typically referred to as AC mode due to the alternating contact of the tip to the surface. In AC mode, the cantilever is driven to oscillate at or near one of its resonance frequencies.[55] During each oscillation cycle, the tip moves through an interaction potential that consists of long-range attractive and short-term repulsive components when the cantilever and sample are close. The changes in amplitude, phase and resonance frequency of the oscillating cantilever are caused and varied by the complex tip-sample forces. Hence, topography, amplitude and phase can be collected simultaneously. The major advantage of using the AC mode is to reduce working time on the surface. Owing to the lower interaction between tip and surface, it results in a better resolution of the topographical image. Another important advantage is that in AC mode the sensitive samples can be imaged without any damage or serious image deformation. In addition, during working in AC mode, trapped electric charges on the surfaces are eliminated. Since one of the important aims of this study is to characterize the electrical properties of the sample, measuring the current of a conductive sample, AC mode offers limited advantages.

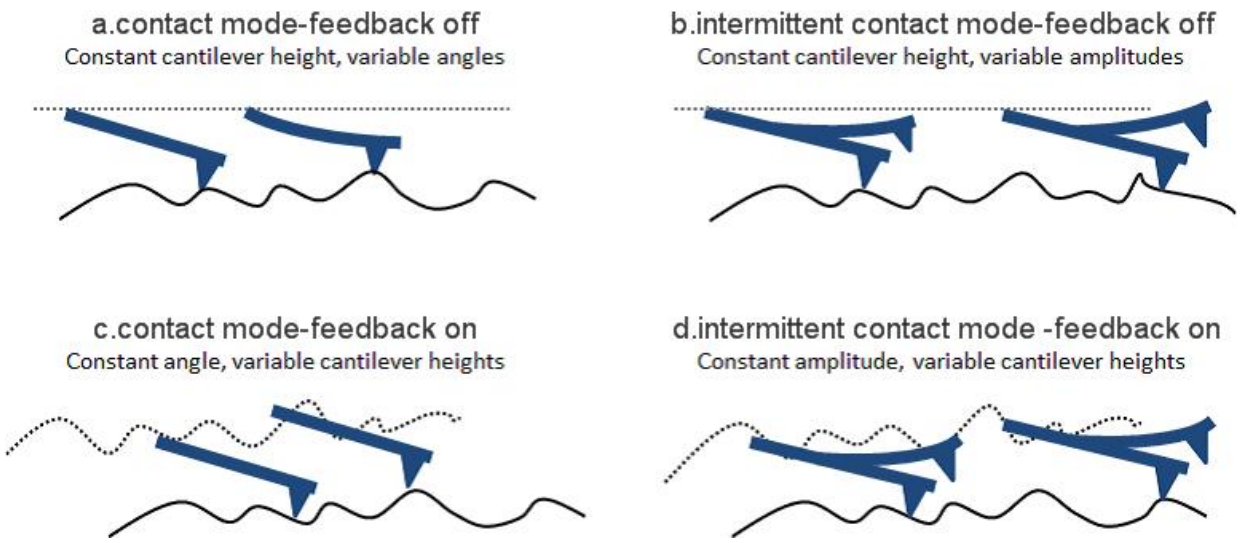

Figure 1.9 Schematics of AFM modes: (a) contact mode without feedback, (b) intermittent contact mode without feedback, (c) contact mode with feedback, (d) intermittent contact mode with feedback.

In order to characterize the local electrical surface conductivities on micro- and nanometer scale, conductive atomic force microscope (c-AFM) is employed. The c-AFM[64-66] is an effective current sensing technique by using with standard AFM contact mode for the electrical characterization of the conductivity changes in resistive samples and it can be probed either in imaging or spectroscopic mode. In imaging mode, the electrical current image can be obtained. In spectroscopy mode the current-voltage spectra and the current-force spectra can be obtained. The big advantage is that we can record morphology and current map of the same area and can directly compare the features in height and current. Figure 1.10 shows the scheme of the electrical circuit in c-AFM. When applying a DC bias voltage between the conductive tip and the sample, the tip scans along the sample surface in contact mode. The deflection of the cantilever is kept constant via a feedback loop and the local height of the sample is measured consequently. We use the ORCA module of *MFP-3D(TM) AFM System* (*Asylum Research Company*) which consists of a specially designed cantilever holder (shown in Figure 1.10 inset) with a transimpedance amplifier. The gain of the amplifier can be chosen by user with the values ranging from 5×10^7 to 5×10^9 V/amp. The conductive AFM Pt-Ir coated probes are combined

with the special cantilever holder to make the measurements. When operated in contact mode, the conducting tip can then close the loop to form an electrical circuit. The AFM head contains the special cantilever holder, for applying voltages; as well as a transimpedance amplifier, which can measure small currents in the circuit. The cantilever holder has a current sensitivity of 2 nA/V and a resolution of 0.5 pA. Current can be measured in the range from -20 nA to 20 nA.[67] The ORCA module of the *MFP-3D* provides a low-noise and flexible transport measurement at the nanoscale. The technique is useful in molecular recognition studies and can be used to spatially resolve electronic and ionic processes across cell membranes. It has proven useful in joint *IV* spectroscopy and contact force experiments as well as contact potential studies.

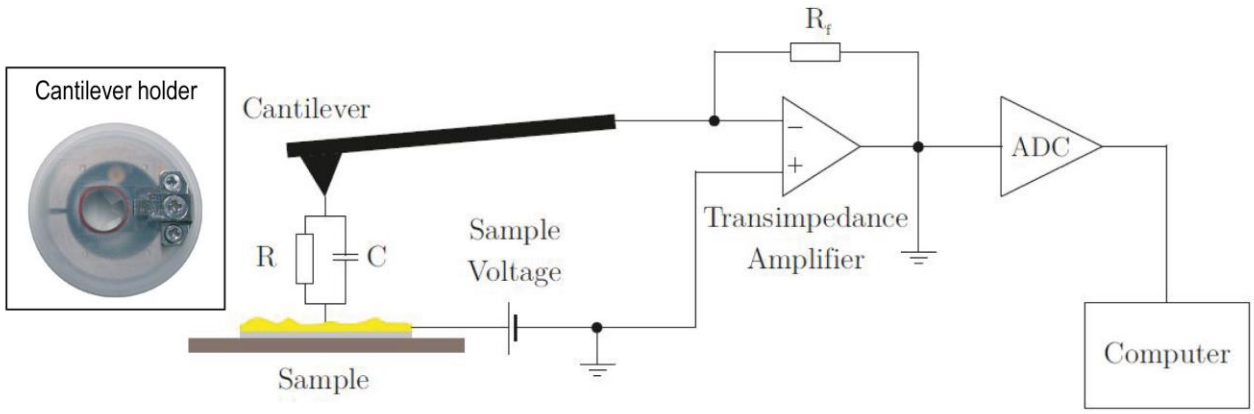

Figure 1.10 Schematic of the electrical circuit of conductive AFM. An applied bias between cantilever and sample leads to a tunneling current between tip and sample. This current signal is sent from the tip to a transimpedance amplifier, which converts the current into a voltage. An analog to digital converter (ADC) changes this voltage into a signal created into a picture by a computer. Inset: ORCA cantilever holder.

Figure 1.11 shows a sample of MoS_2 flake which is the main material measured by AFM in this thesis. The topographic images of MoS_2 in contact mode are shown in Figure 1.11 (a) and (b). The current image of (b) measured by c-AMF is shown in (c). The tip was positioned in the center of the colored dots and then the bias voltage is swept from -1V to 1 V and the response current is measured, where the resulting *IV* characteristics are shown in (d). The conductivity

curves give consistent results with the contrast observed in (c). Especially, the conductivity of the thinner layer marked with red dot is higher.

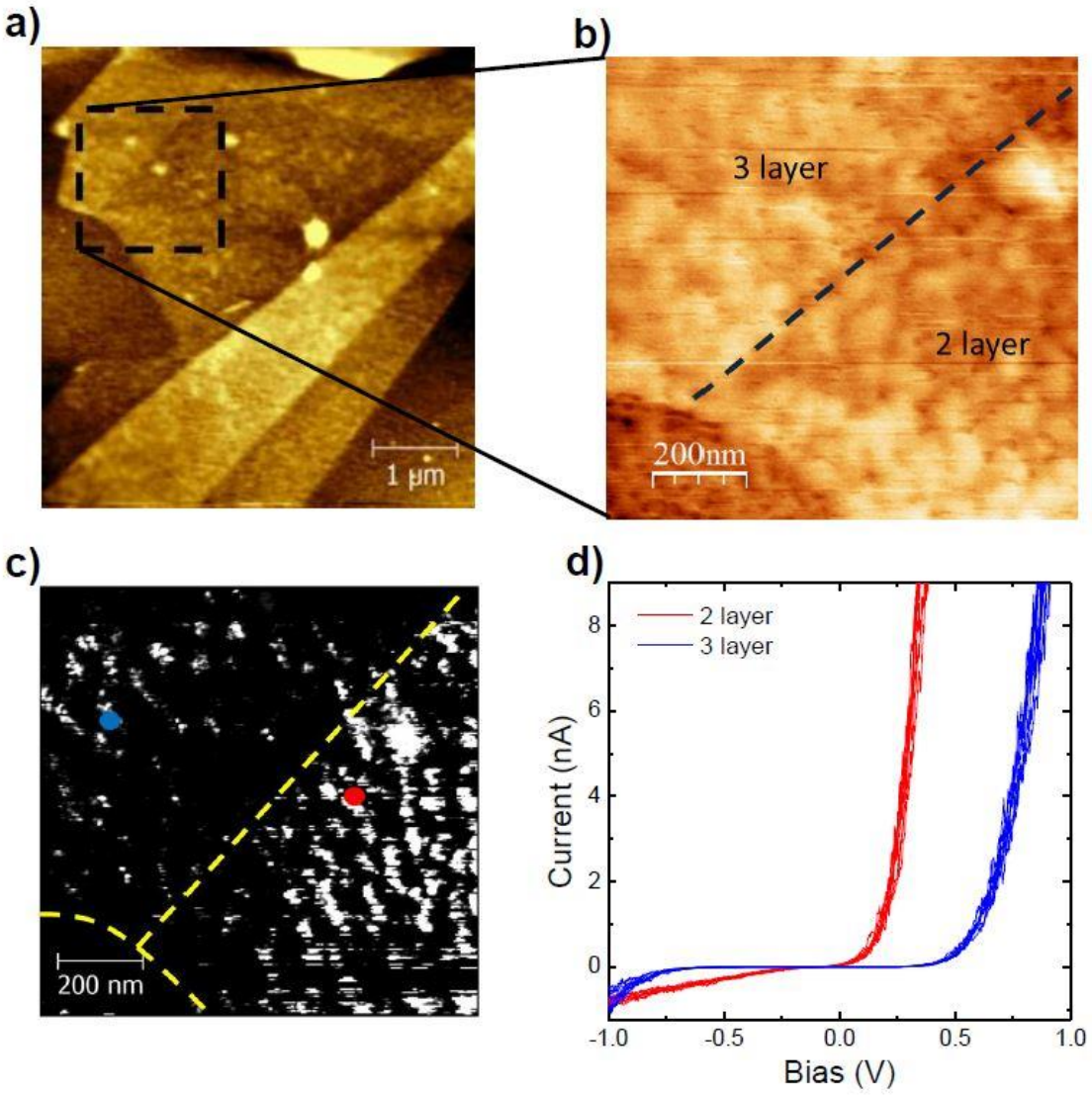

Figure 1.11 (a) Topography images of a MoS_2 sample in 5 × 5 μm. (b) 1 × 1 μm zoom-in image of (a). (c) The current image of (b). (d) The corresponding *IV* curves recorded at two specific positions indicated in (c). The conductivity curves are compatible with the current contrast observed in (c).

1.3 Molecular optoelectronic devices

Molecular optoelectronic devices of organic semiconductors are of great interest because organic semiconductors have many fundamental advantages over their inorganic counterparts.[68-71] For example, their low cost and mechanical flexibility are ideal advantages for large-area applications. However, the most attractive prospect is their incorporation of functionality by molecular design.[72] So far, the first generation of organic semiconductor devices for e.g. light emitting diodes[73] and photovoltaics[74], are based on (macro)molecules processed with a wide range of methods in an effort to make them compatible with the scientific capabilities of the semiconductor industry. In order to allow a transition to a second generation of multi-component molecularly precise devices, improved control must be achieved. In other words, devices must be fabricated where the absolute location of different molecular components is controlled and precisely known *a priori*.

1.3.1 Photovoltaics

Photovoltaics (PVs) convert solar energy into current electricity through semiconducting materials that exhibit the photovoltaic effect[75]. The photovoltaic effect was discovered in 1839 by Edmond Becquerel: when he shined light onto an AgCl electrode in an electrolyte solution, a voltage was induced by the light.[76] The photovoltaic effect refers to photons of light exciting electrons into a higher state of energy, allowing them to act as charge carriers for an electric current. Referring to the growth of photovoltaics, the first generation of PVs, mono/multi-crystalline silicon photovoltaic systems, have an average efficiency of 14%.[77] After that, the cadmium telluride is one of the fastest-growing thin film based solar cells which are collectively known as second generation devices. And in the beginning of the 19th century, organic and polymer photovoltaics (OPVs) have been pursued as the third generation PVs with the observation of photoconductivity in solid anthracene[78, 79]. OPVs are one type of photovoltaics that uses conductive organic polymers or small organic molecules[80] for transport electrons or light absorption to produce electricity from sunlight by the photovoltaic effect, which has the rich

potential due to their light weight, thin, flexible, and simple fabrication advantages.[81, 82] A common characteristic of both the small molecules and polymers (as shown in Figure 1.12) used as the light absorbing material in photovoltaics is that they all have extended π-conjugated organic systems.

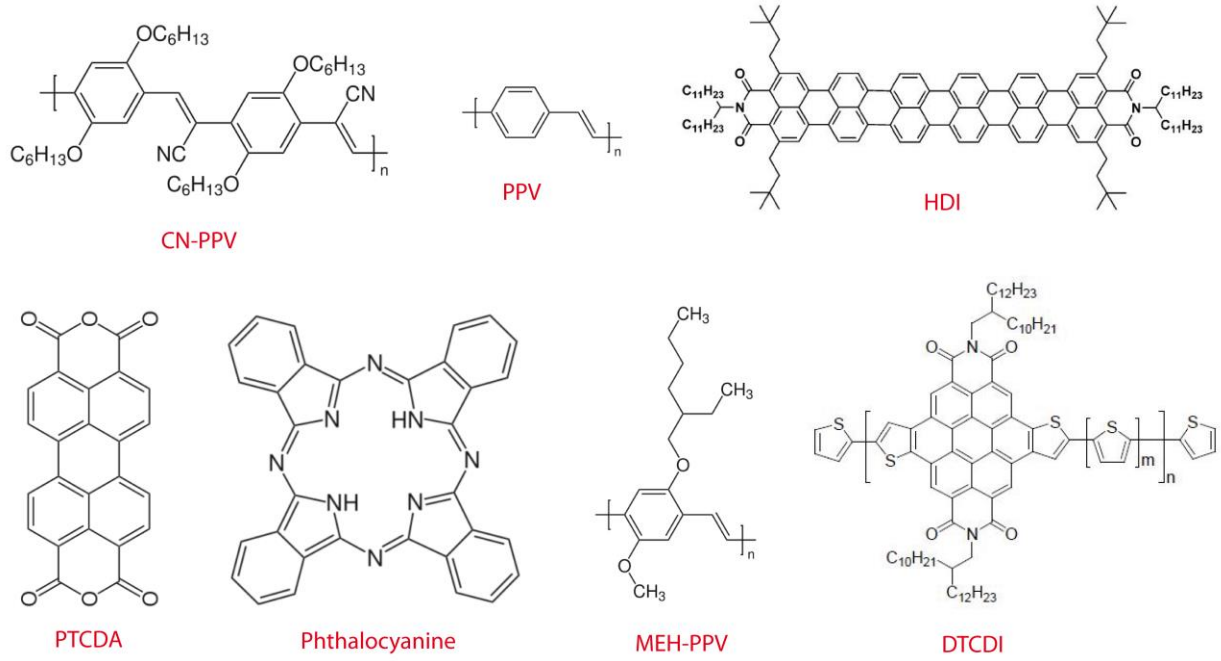

Figure 1.12 Examples of organic photovoltaic materials.

In our work, the organic molecules of rylene derivatives are exclusively introduced and applied in photovoltaic devices owing to their outstanding chemical, thermal and photochemical stability and non-toxicity.[83, 84] Rylene diimides (Figure 1.13) are a series of polycyclic hydrocarbons based on naphthalene units that are linked in the peri-position such as terrylene, quarterrylene. The simplest and most intensively investigated rylene diimide systems are perylene-3,4:9,10-tetracarboxylic diimides (PDIs) and naphthalene-1,8:4,5-tetracarboxylic diimides (NDIs) which are shown in Figure 1.13. In addition to their good chemical, thermal and photochemical stability, rylene diimide-based polymers also exhibit high electron affinity and high electron mobility derived from the electron accepting imide groups, thus making the polymers act as promising candidates for various organic electronic fields.[85-87] PDI has been known for nearly a century, however, the PDI-based small molecules and polymers have attracted

interest as alternative electron-transport materials in OPVs since they exhibit large optical absorptivities, high electron mobilities and electron affinities similar to those of fullerenes which are the most commonly used acceptors. Mikroyannidis *et al.*[88] obtained a photon-to-current efficeincy (PCE) of 2.3% under white-light illumination by using an alternating PDI-phenylenevinylene copolymer acceptor and poly(3-phenyl hydrazone thiophene) donor in OPVs. Compared to the PDI-based counterparts, NDI-based molecules initially showed relatively poor features as acceptors because of their small fused-ring unit, large band-gap.[85] However, in later studies polymerization of NDI units increases the conjugation length and enhances the PCE of device.[86]

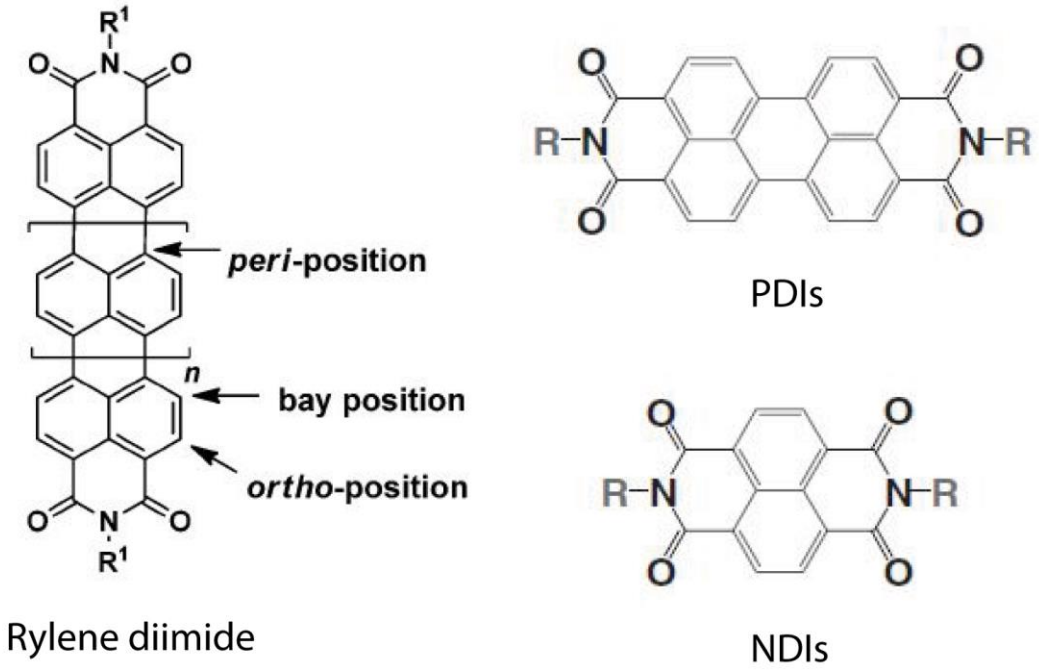

Figure 1.13 Chemical structures of rylene diimide, PDIs and NDIs.

A π-conjugated system is formed when carbon atoms covalently bond with alternating single and double bonds. Electrons in p_z orbitals interact and form a π orbital with a π* antibonding orbital. In the simplest approximation, the delocalized π orbital is the highest occupied molecular orbital (HOMO), and the π* orbital is the lowest unoccupied molecular orbital (LUMO). In organic semiconductor physics, closely-spaced orbitals near the HOMO take the role of the

valence band while close-spaced orbitals near the LUMO serve as the conduction band. The energy separation between the HOMO and LUMO energy levels is the energy gap of organic electronic materials and is typically in the range of 1 - 4 eV.[89] Figure 1.14 provides schematics of basic energy level diagrams used to describe OPVs. The ionization potential (IP) of a neutral organic material is the energy required to remove an electron from its highest occupied molecular orbital (HOMO) to vacuum. The electron affinity (x) is a measure of a material ability to act as an electron acceptor, and is often approximated as the LUMO level relative to vacuum of an organic material. The HOMO-LUMO gap (E_g) of a conjugated organic material is the minimum energy required to promote an electron from its HOMO to its LUMO. When the light is absorbed by the organic material, an electron is promoted from its highest occupied molecular orbital (HOMO) to its lowest unoccupied molecular orbital (LUMO) forming an exciton. Then electron is collected at the Al electrode and the left hole is collected at the ITO electrode. In order to achieve charge separation, an electrical field is necessary, provided by the asymmetrical ionization energy/work functions of the electrodes. This asymmetry is the reason why electron-flow is more favored from the low work function electrode to the high work function electrode (forward bias), a phenomenon referred to as rectification.[81, 90, 91]

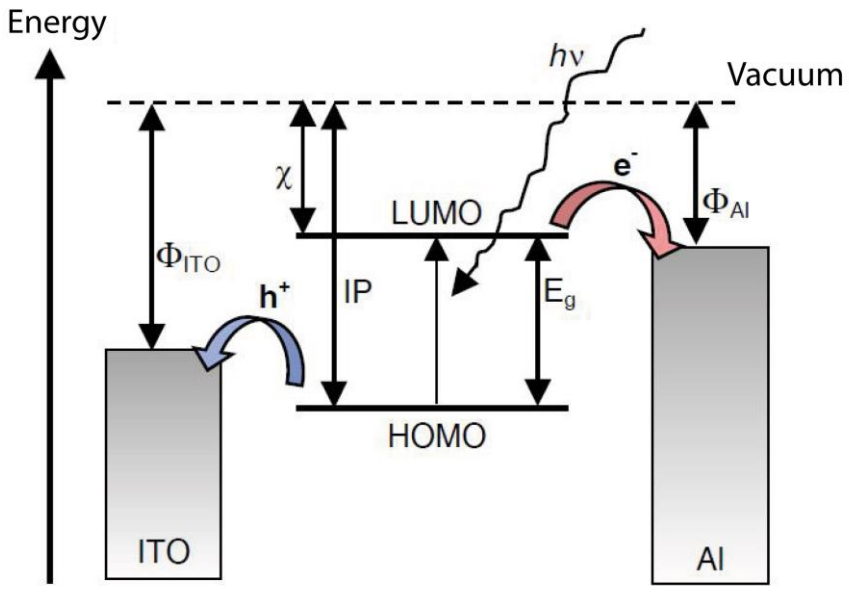

Figure 1.14 Energy levels and light harvesting.[81]

Organic photovoltaics (OPVs) have been fabricated in flat heterojunction[92] and bulk heterojunction[93] solar cells according to the configuration of the active layer. The organic materials of the active layer in the devices consist of three main types: small molecules[94], polymers[95] and hybrid organic-inorganic materials[96]. The key to increase the power conversion efficiencies with organic solar cell technologies is the engineering of spatial order alongside investigation of new materials which fulfill the multiple parameters necessary for the OPVs purpose, such as light harvesting, charge transfer, and charge transport.

1.3.1.1 Flat-heterojunction cells

The idea behind a heterojunction is to use two layers with different electron affinities and ionization energies because excitons do not dissociate readily in most organic semiconductors. The flat-heterojunction cells contain two layers in between the conductive electrodes (Figure 1.15). The materials are chosen to make the differences of electron affinities and ionization energies large enough that these local electric fields are strong, which split excitons much more efficiently than single layer photovoltaic cells. The layer with higher electron affinity and ionization potential is the electron acceptor. This technology has been applied since the emergence of the first organic p-n junction solar cell which was built by Tang by sequential vacuum deposition of perylenedibenzimidazole and copper phthalocyanine (CuPc).[74] This simple bilayer device yielded an efficiency of about 1%. Generally, flat-heterojunction cells are fabricated in the sandwich structure and the structure is also called a planar donor-acceptor heterojunction.[91, 97-99]

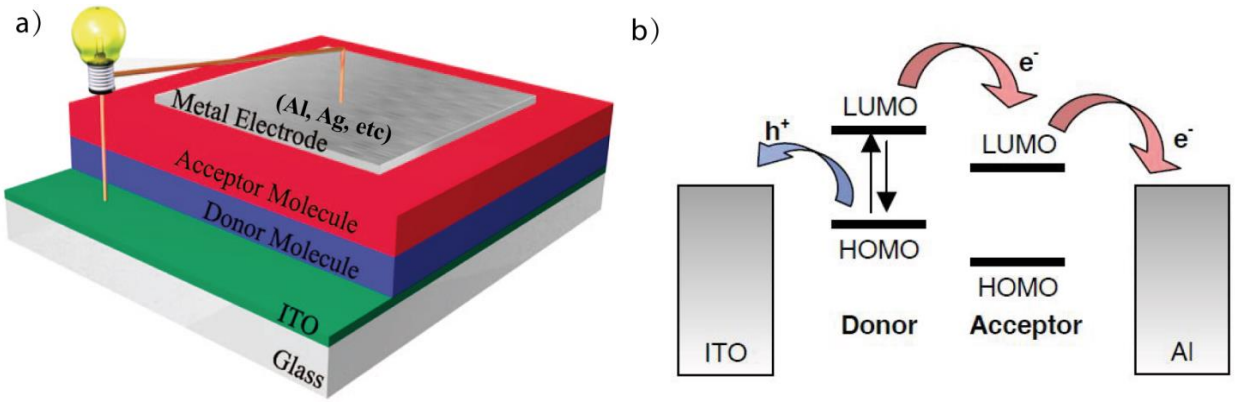

Figure 1.15 (a) Sketch of a bilayer organic photovoltaic cell[91]. (b) The exciton dissociation at the donor-acceptor interface. The electron goes to the acceptor while the hole stays on the donor.[81]

As shown in Figure 1.15 (a), the donor and the acceptor compounds are deposited on the indium tin oxide (ITO) coated glass substrate layer by layer. Then the most common metal electrode such as silver or aluminum is deposited under vacuum on top of the acceptor layer. When the active layers are exposed to light, excitons are formed where the electrons and holes are bound by Coulombic forces. Subsequently, the excitons (electron-hole pairs) diffuse to the interface of donor-acceptor materials where they dissociate into electrons and holes. Afterwards, the free charge carriers move to their corresponding electrodes: holes reach to ITO and electrons reach to Al electrode with the help of the internal electric field. (Figure 1.15 (b))

In these bilayer solar cells, due to the small interfacial area of the separated layer structure of donor and acceptor, the amount of absorbers which can actually contribute to the photocurrent is limited. Actually only those excitons extremely close to the interface of the donor and acceptor junction will be able to dissociate prior to dissipative recombination. Unfortunately, the exciton diffusion length is generally much less than the optical absorption length, which limits the quantum efficiency of such devices.[91]

1.3.1.2 Bulk-heterojunction cells

Compared with flat-heterojunction cells, one possibility to improve the efficiency is to enlarge the donor-acceptor interface area, where excitons are dissociated.[100] Hence the so-called bulk-heterojunction cells appear consisting of a nanoscale blend of donor and acceptor materials. In this blend structures where the donor phase is intimately intermixed with the acceptor phase, the excitons can reach an interface with short lifetimes and subsequently dissociate to holes and electrons.[101] The free charge carriers will then move to their corresponding electrodes by following the continuous route of either donors or acceptors. In 1995, the first solution-processed polymer heterojunction structures using polymer-fullerene and polymer-polymer blends were presented by the groups of Heeger[93] and Friend[24] respectively. It was quickly recognized the important significance of mixtures of conjugated polymers and also that mixtures of a conjugated polymer with a soluble fullerene derivative solidify as bulk-heterojunctions from solution. The donor and acceptor segregate into separate phases and form an interpenetrating bicontinuous network which could compensate for the limited diffusion length.

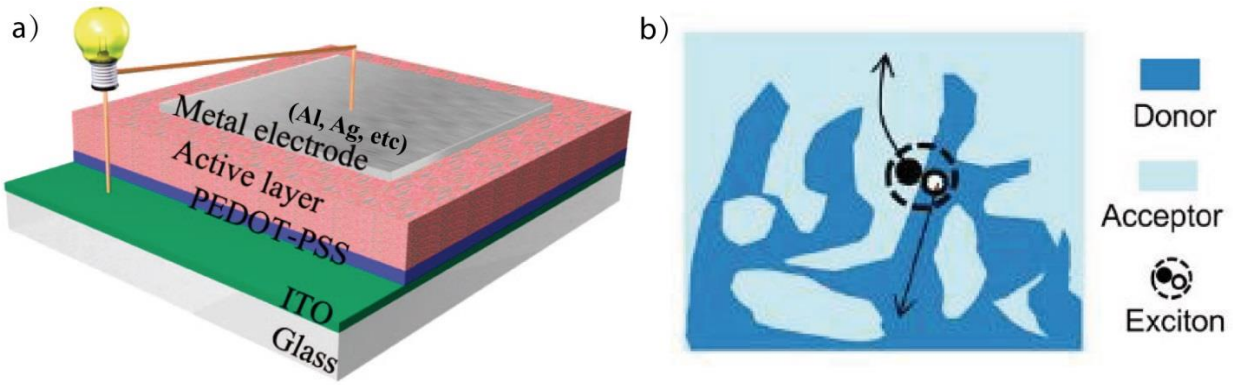

Figure 1.16 (a) Sketch of a bulk-heterojunction cell. The PEDOT:PSS layer improves the interface between the active layer and the ITO.[91] (b) Cross-section of the mixed bulk heterojunction.[101] Charge separation readily occurs at the donor-acceptor interface area.

The schematic of bulk-heterojunction cell and its charge separation process are shown in Figure 1.16. In Figure 1.16 (a), a typical bulk-heterojunction solar cell containing an active layer

and two electrodes is shown. One of the electrodes for photon absorption is an ITO-coated glass substrate which is as same as the one used in flat-heterojunction cells. Especially the substrate is covered by a transparent and conductive polymer which is most often poly(3,4-ethylenedioxythiophene):polystyrene-sulfonate (PEDOT:PSS).[102, 103] In this kind of bulk-heterojunction cells, the PEDOT:PSS layer provides an improved interface between the active layer and the ITO electrode that consequently improves the performance of the solar cell devices. The highly conductive PEDOT:PSS layer can be obtained by spreading its aqueous dispersion of gelled particles on the ITO substrate, generally by spin-coating and driving out the water by heat. After that, printing the mixture of the conjugated polymer with fullerene on top of PEDOT:PSS layer to form the active layer of the device. Finally, an aluminum or silver film is covered on the active layer as the counter electrode via the vacuum deposition. As illustrated in Figure 1.16 (b), it reveals how the charge separation occurs at the small donor-acceptor interface area. The high interfacial area between the donor and acceptor materials facilitates the exciton diffusion process, even for active layers significantly thicker than the exciton diffusion lengths. Although the concept of bulk-heterojunction brings a powerful solution to address the issue of exciton dissociation, the nanostructural morphology of bulk heterojunctions is still critical to achieve the optimal spatially distributed exciton dissociation interfaces and proper charge transport channels for collecting the electrons and holes effectively.[104, 105] The preferred morphology of bulk-heterojunctions is a bicontinuous interpenetration donor-acceptor network like Figure 1.16 (b). It has been proven that after thermal or solvent annealing, the donor-acceptor structures will become more apparent with a typical feature size of ~ 10 nm, as a result of the increased crystallinity of either donors or acceptors, which can benefit the charge transport in the active layers and hence improve the power conversion efficiencies of the device.[92, 101, 106]

1.3.1.3 Recent advances and aim of the thesis in OPVs

In the last two decades, the field of organic photovoltaic materials and devices has expanded enormously and attracted researchers in many disciplines. Aside from the basic flat- and bulk-heterojunction structures, other novel device architectures have been demonstrated, including double flat-heterojunction cells[107], mixed flat-heterojunction cells[108] and controlled bulk-heterojunction cells[109, 110], all of those target an improved balance between potentially conflicting

mechanisms. It is known that the development of OPVs has always been accompanied by innovations in materials science. Many polymers with the higher performance have been developed very fast in these years. For instance, poly[2,6-(4,4-bis-(2-ethylhexyl)-4*H*-cyclopenta[2,1-*b*;3,4 *b*']dithiophene)-alt-4,7-(2,1,3-benzothiadiazole)] (PCPDTBT), it is a low-bandgap polymer whose absorption extends up to 900 nm. The modified OPVs made from this polymer by incorporating alkanedithiol additives have showed an efficiency of around 5.5%.[111] One of the effective approaches improving the power-conversion efficiency (PCE) is to develop novel acceptors.[112, 113] In 2011, Hashimoto *et al.* reported a polymer solar cell based on six different kinds of PDI-based polymers, and achieved the best PCE of 2.23% by optimizing the solvent.[114] In 2012, Neher *et al.* reported an improved PCE of 1.4% by using P3HT and P(NDI2OD-T2) as the donor and acceptor materials by changing the solvent to *p*-xylene and chloronaphthalene.[115] In 2003, Jenekhe *et al.* synthesized the NDI-selenophene copolymer acceptor PNDIS-HD and achieved a PCE of 3.3% by using PSEHTT as the donor.[116] In the same year, Zhao *et al.* fabricated an inverted polymer solar cell with a PCE of 2.17% by using the first 1,7-regioregular PDI-dithiophene copolymer and P3HT as the acceptor and the donor,[117] and then they enhanced the PCE beyond 4.4%, the highest value for PDI-based polymers, by the side-chain engineering of low band gap donor polymers in 2014.[118] Very recently, Jenekhe *et al.* achieved a new PCE record of 7.7% for NDI-based polymers by employing an acceptor material of PNDIS-HD and a donor material of PBDTT-FTTE in 2015.[119] Although the rylene-based polymers exhibit the advantages of good thermal, chemical, and photochemical stability in OPVs, the PCEs of rylene-based OPVs do not yet rival the fullerene-based systems. There are still lots of improvements and optimizations have to be made to achieve enhanced device performance. The aim of this thesis is to introduce new device geometries with molecular resolution for OPVs. This will be achieved by sensitizing atomically-flat, transparent electrodes with engineered molecular networks of near-infrared absorbing dyes. Building on the introduction above, such molecular architectures at interfaces have the potential of linearly scaling PCEs through tandem device fabrication, thereby achieving long absorption lengths, sub-nanometer scale exciton-dissociation lengths, and ballistic charge transport at interfaces.

1.3.2 Photoswitches

Molecular switches are a special type of molecular machines that can be switched between at least two distinct states by applying an external stimulus. One advantageous stimulus is light due to its high spatial and temporal resolution, allowing for true remote control.[120] Switchable molecules gained considerable interest in the last years owing to their possible applications in optoelectronic devices. Especially, small organic molecules, capable of undergoing efficient and reversible photochemical reactions to make them switchable between two metastable isomers associated with significant different properties, are impacting the materials world. Such molecular photoswitches are being implemented in a variety of application products ranging from photoresponsive polymers to the optical devices with macroscopic properties that can be externally manipulated by light[121]. Today's photoswitches exhibit an ultrafast, clean, and highly reversible photochemistry, which provides sufficient fatigue resistance for technical applications and also render these systems environmentally friendly. Several exciting examples of the incorporation of switches in device applications in the areas of microelectronics and material sciences are already available.[122, 123]

Photochromic compounds[124] are particularly interesting molecular switches, which are a special type of photoswitches that undergo a reversible transformation by resonant absorption of radiation between two stable forms. Several exciting examples of synthetic molecular photoswitches have been designed. The devices can undergo a reversible change upon the irradiation with light. They are commonly characterized by the absorption maxima of their isomeric configurations, as well as the photostationary state.[125]

1.3.2.1 Azobenzene switches in this thesis

Azobenzene molecules represent some of the most extensively studied molecular switches.[121, 126-133] They are organic compounds featuring a diazo moiety (N=N) linking two phenyl rings together.[134] Azobenzene molecules exist in two isomeric states which are *trans* and *cis* states (Figure 1.17). The most interesting property is the possibility to controllably switch between these two states. This property has been successfully applied to control ion

complexation[135], electronic properties[136] and catalysis[137], and to modify structural organization in monolayers and thin films[138].

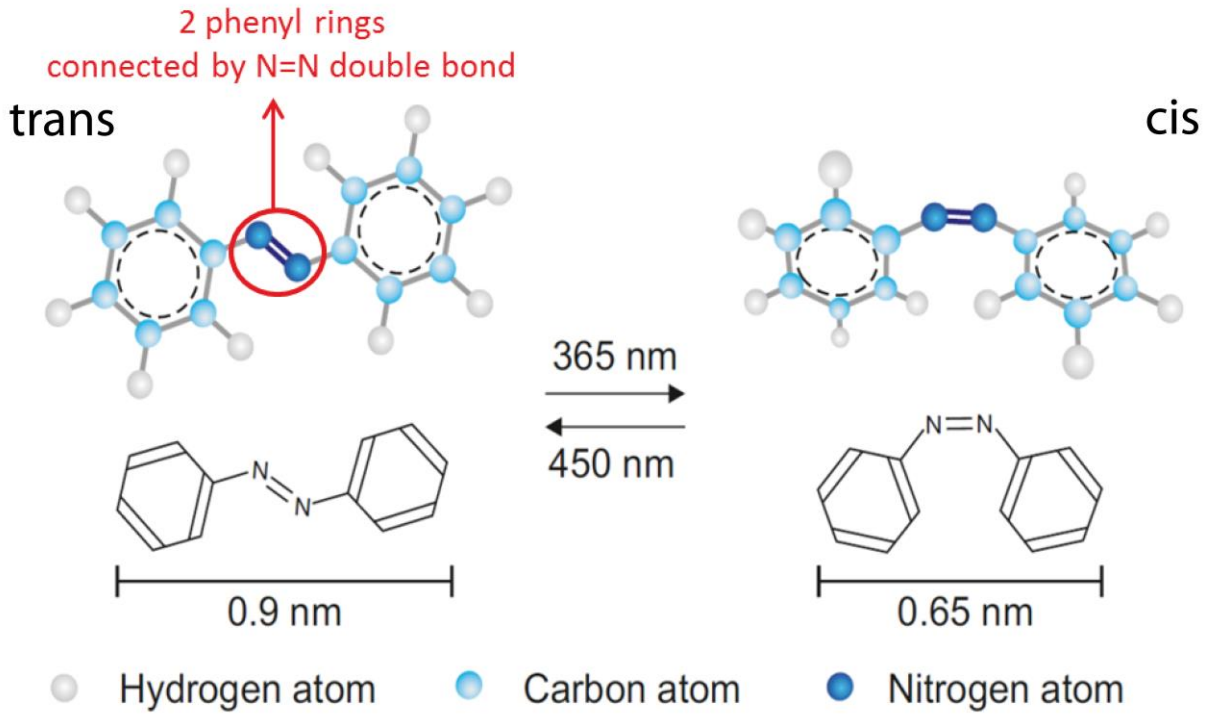

Figure 1.17 Azobenzene *trans* and *cis* photoisomerization respectively.

The transition between two states of azobenzene is related to their electronic structures. The important factors of the switching are the ground state and the first and second excited singlet state. The energy of the excited states differs in the different isomers of the azobenzene (*trans* and *cis*). These two isomers show different absorption spectra. For unsubstituted azobenzene, the *trans* isomer absorbs in the visible spectral region at around 450 nm and it is the ground electronic state of azobenzene molecules. Unlike the *trans* isomer, the *cis* isomer absorbs in the UV spectral region and more precisely at 365 nm. A typical absorption spectrum of the azobenzene is shown in Figure 1.18 (a). The stronger peak around 360 nm is resulting from the symmetry which allowed π-π* transition and the weaker peak around 450 nm indicative of the symmetry forbidden n-π* transition.[125] The UV resonances of azobenzene *trans-cis* conformations correspond to the excitation of an electron from the azobenzene electronic ground state S_0 to the first or second excited state (S_1, S_2), as shown in Figure 1.18 (b). The S_1 excited

state (n, π), results from an electronic transition and/or an occupied non-bonding nitrogen atom lone pair (n) to an unoccupied N-N anti-bonding π orbital (π*). The S_2 excited state (π, π*), results from an electronic transition and/or an occupied N-N bonding π orbital (π) to an unoccupied N-N anti-bonding π orbital (π*). Therefore, azobenzene is characterized by a low-lying S_1 (n, π*)-state and a large energy gap between lower S_1 and the next higher S_2 (π, π*)-state[139]. To date, azobenzenes remain the most widely used photoswitches in photoelectrical applications because of their ease of synthesis, relatively high photostationary states and quantum yields, fast photoisomerization, and low rate of photobleaching.[140] Because of these reasons, in this thesis we will explore self-assembled azobenzenes monolayers on gold surface to reversibly modify the vertical transport properties of absorbed 2D crystalline, atomically flat electrodes. Because 2D crystals are platforms for the growth of molecular architectures, this approach will provide means to regulate charge and energy transport to and from molecular architectures. We foresee such photoswitchable platforms acting as heat sinks or tailored electron- or hole-blocking layers at interfaces towards ultraefficient organic photovoltaics, sensors and transistors.

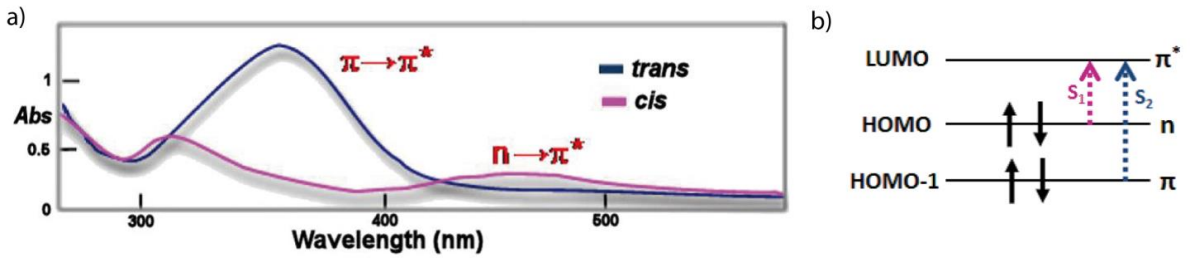

Figure 1.18 (a) Representative example of an UV spectrum of the azobenzene: blue line and magenta line represents the *trans* the *cis* isomer respectively.[141] (b) Electronic structure of azobenzene.[139] Electron spin configuration (black arrows) denotes the electronic ground state (S_0). Red and blue arrows denote the electronic excitation from S_0 to both S_1 (first excited state) and to S_2 (second excited state), respectively.

Chapter 2

Experimental Methods

In this chapter, the substrates, molecules, 2D materials and methods which are used to characterize the molecular assemblies and device fabrication in all experiments will be introduced in detail. The chapter consists of three sections, where the first section focuses on the substrates for molecular self-assembly and *IV* characteristics. The second section contributes the description of the adsorbates which mainly consist of self-assembled monolayer (mixed SAMs) based on HS-C_6 azobenzene and spacer molecules and supramolecular networks. Finally, the chapter ends with the explanation of the transistor device fabrication mainly based on MoS_2 mono- and multi-layer 2D crystals.

2.1 Substrates

2.1.1 Highly oriented pyrolytic graphite (HOPG)

The HOPG crystal is a popular substrate for STM due to its flat cleavage surface and its inert nature, which make it possible to obtain images in air with atomic resolution.[142] Graphite is formed by layers of honeycomb atomic array of carbon atoms. The layers are held together by van-der-Waals forces and they present an ABAB stacking sequence. This stacking sequence gives rise to a 4-carbon atom unit cell with two nonequivalent atomic sites: the α-sites, atoms with neighbors directly above and below in adjacent layers, and the β-sites, atoms without such neighbors[143] (in what follows α and β atoms, respectively). The electrons in the layers are sp^2-hybridized, and thus the carbon-carbon σ-bonding within the sheets is strong with an interatomic distance of 1.42 Å, in comparison to the weak π-π interactions between the sheets, mediated by out of plane p_z-hybridized orbitals[144] with an interlayered distance of 3.35 Å.

The schematics of ABAB stacking graphite structure which clearly describe different atomic sites are shown below.

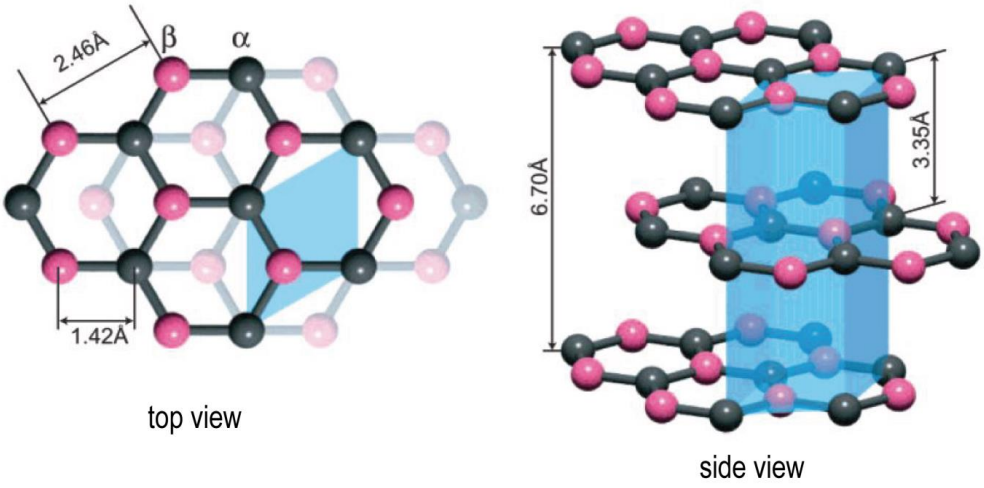

Figure 2.1 Schematics of ABAB stacking of graphite structure. Only the β sites are visible in the STM images.[145]

Due to the higher local density of states (LDOS) of the β site atoms compared with α site atoms near the Fermi level, there exists an asymmetry in the interlayer interaction in the bulk graphite. For low-bias voltages, only β site atoms are visible as a consequence of such asymmetry. Constant current STM performed on graphite only resolves the β site atoms which often called triangular structures has a unit cell length of about 2.46 Å corresponding to the periodicity of the lattice. An experimental HOPG STM image with atomic resolution is presented in Figure 2.2. The image is acquired by constant current mode under ambient conditions. The sample is freshly peeled off by using an adhesive tape in air before scanning. Here the triangular structure is visualized from one of the lattice sites with the unit cell of a = b = 2.3 Å and 60°, which is in good agreement with previously theoretical values.

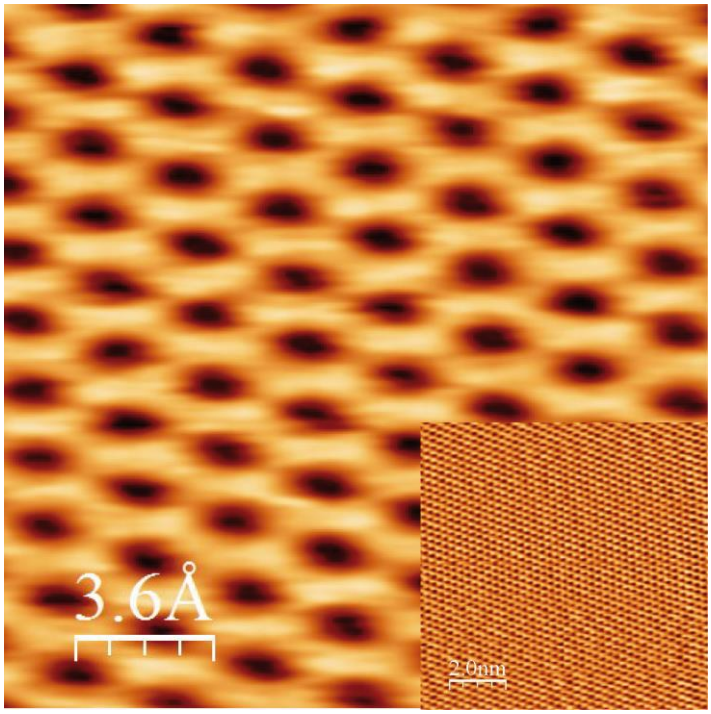

Figure 2.2 A high resolution experimental HOPG STM image. Inset: The large area of HOPG topography image.

2.1.2 Gold

In the thesis, gold is chosen as the metal material to support functionalized self-assembled monolayers (SAMs) in our experiments because it's reasonably inert[146], has a low surface roughness and a highly affinity for thiol chemisorption[147]. To obtain gold films, we evaporate a 10 nm titanium layer for adhesion and a 50 nm thick gold layer on top by using a *Leybold L560* electron beam evaporator for evaporation process. Before evaporation, intensive cleaning of the substrates (eg. silicon wafer) is important to avoid any possible contamination. In this regard, all cleaning steps are carried out in a clean room. A first step of cleaning is done with a sonicator of 80 W output power in acetone, isopropanol and distilled water for 15 minutes respectively. Then oxygen plasma cleaning is implemented at a power of 200 W for 15 minutes. After the cleaning of the substrates, the metallization of the substrates is executed by the electron beam evaporator. This process is performed in a vacuum chamber with a pressure of ~ 10^{-8} mbar. Electrons are accelerated over a voltage of 15 kV and bundled into an electron beam, which heats up crucibles, containing the material used for the evaporation. The sources are evaporated and deposited onto the substrates. By changing the power of the electron beam, the rate of evaporation can be controlled between 0.5 - 0.8 nm/s, which is an important parameter to avoid increasing the surface roughness. It has been proven that atomic force microscope measurements show a root-mean-squared (RMS) surface roughness of 1.5 nm of the gold on a Si/SiO_2 substrate. The typical size of the gold grains is 1 - 2 nm in height and 20 - 80 nm in lateral size.

The atomic resolution of gold surface is difficult to achieve by scanning tunneling microscope under ambient conditions. Figure 2.3 shows a STM image of a gold film (500 × 500 nm) deposited by electron beam evaporation, where the gold grains are clearly resolved and the topographical heights in the z direction are expressed by the color scale of the image, where white denotes the highest feature and black denotes the lowest one.

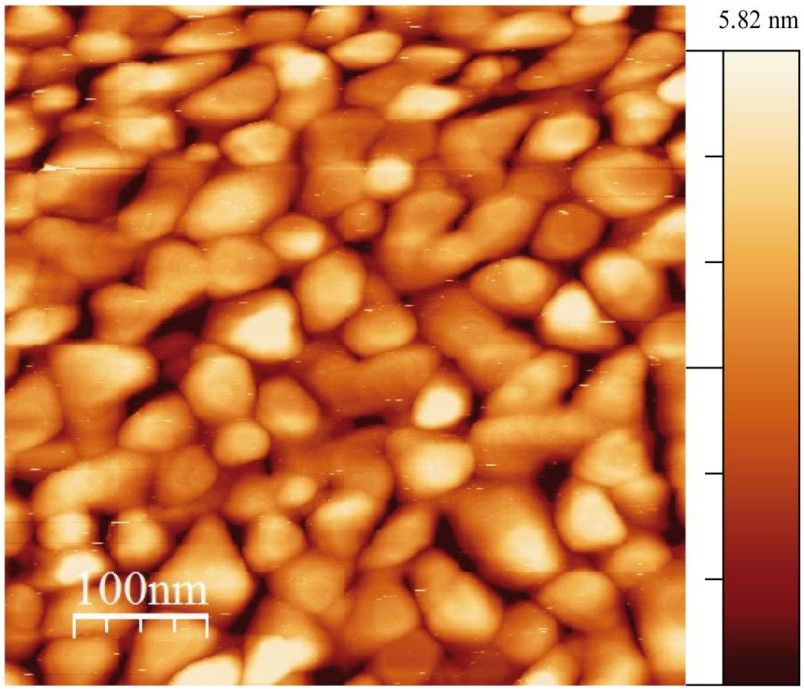

Figure 2.3 STM image of 500 × 500 nm gold film deposited on Si/SiO_2 substrate by electron beam evaporation.

2.1.3 Molybdenum disulfide (MoS_2)

One of the major objectives of this thesis is to investigate the optoelectronic properties of 2D crystals when interacting with photochromic molecules (azobenzene). Specifically, MoS_2 is a semiconductor dichalcogenide compound which has a layered hexagonal crystalline structure made from both transition of metal molybdenum (Mo) and chalcogen non-metal sulphur (S).

The diagrams of the lattice structure of MoS_2 and its stacking orders are shown in Figure 2.4. In each single layer of 2D material, Mo atoms are covalently bonded to S atoms. A single layer forms only if the Mo atom is placed in the center and S atoms placed at the edges.[148] Every single layer is bonded weakly to surrounding layers by electrostatic dipole forces and van-der-Waals forces, providing the possibility to exfoliate them to 2D sheets. In addition, MoS_2 has a transition from indirect to direct band-gap when scaling down the number of layer thickness. The two

stacking orders (2H-AB and 3R-ABC) of MoS_2 are given in Figure 2.4 (b) and (c) respectively. The 2H-AB stacking is a structure where the unit cell is tetragonal consisting of two sulfur atoms and one molybdenum atom. When the first layer is formed, the second layer is rotated by 180° according to the first layer. Consequently the sulfur atom takes place in the position of the molybdenum and vice versa. The third and the fourth layers follow the same arrangement of the first two layers. In other words, each two layers as a unit to be repeated to form this stacking order, which is called AB. The thickness of monolayer originated from this structure is about 6.5 Å[149]. Another stacking order, called 3R-ABC is shown in Figure 2.4 (c). Here, the layers stay in the same order where the minimum unit of stacking order consists of three layers known ABC. The next fourth layer stays in the same position as the first layer again. On the other hand, the second layer shifts as its sulfur atoms are placed directly above the first layer's molybdenum atoms and similarly on the third layer. The main difference between these two configurations is the spin orbit splitting where the 2H structure is about 30% larger than the 3R structure[150].

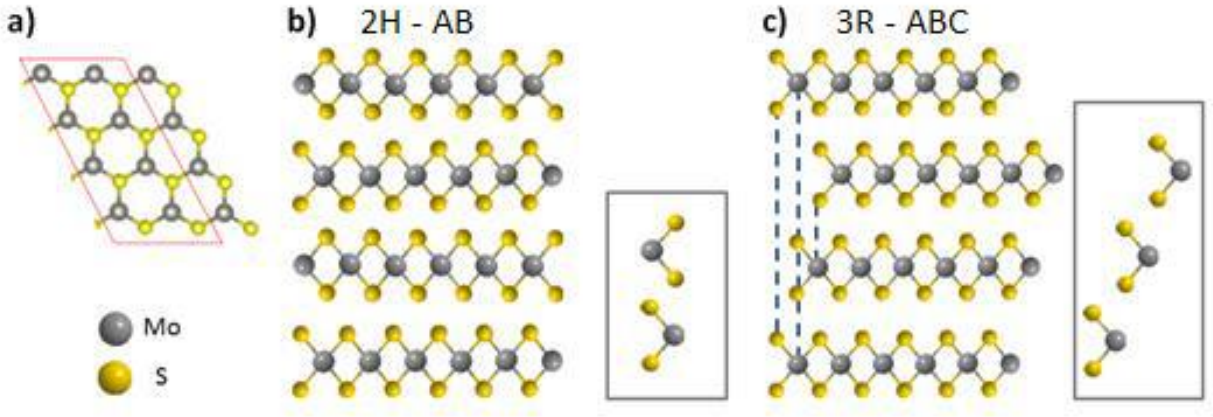

Figure 2.4 (a) The lattice structure of a monolayer MoS_2. (b) 2H-AB stacking structure of MoS_2. (c) 3R-ABC stacking structure of MoS_2.

The presence of an energy gap in MoS_2 with field effect on/off ratios[151] exceeding 10^8, makes it be a promising material for developing the next generation of few atom-thin logics, photodetectors[152] and light emitting diodes[153]. The ability to modulate the optoelectronic response by means of external stimuli is one of the key requirements in the field of micro- and nano-

electronics. In this regard, optical switchable devices based on MoS_2 stand as a promising technological paradigm, due to the possibility of ultra-fast photoswitching[154] and post-binary logic[155, 156]. That is why MoS_2 is chosen as a proof-of-concept semiconductor material for our optoelectronic switching study. Figure 2.5 (a) presents a typical optical microscope photo of MoS_2 flake with different layers exfoliated on silicon wafer. The thickness of flake can be recognized from the contrast difference on the Si substrate, where the region with a lower contrast respect to the substrate is identified as the thinnest layer. In order to identify precisely the number of flakes corresponding to the contrast difference, a useful investigation can be done by using AFM with the height profile as shown in Figure 2.5 (b). It shows the height of single layer with about 2 - 3 nm thickness.

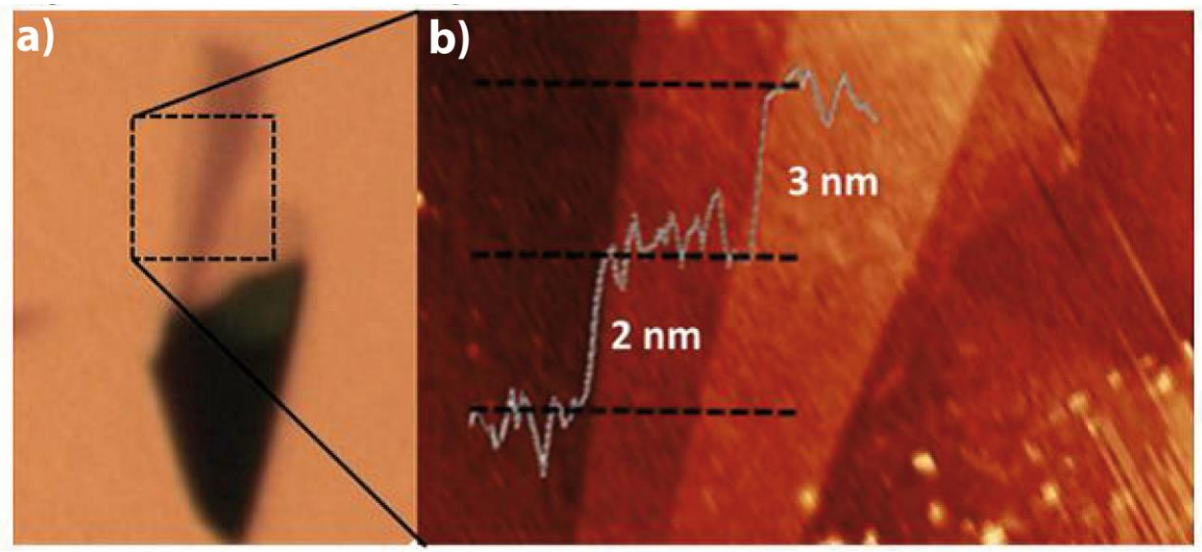

Figure 2.5 (a) A typical optical micrograph of MoS_2 on Au substrate at different thicknesses. (b) AFM morphology image picture with a height profile inset of the flake at about 2 - 3 nm thickness.

2.1.4 Diamond

Diamond is one of carbon allotropes where all of the atoms are connected via sp^3 orbitals. At room temperature diamond has a behavior of insulator with a 5.47 eV indirect band gap.

However the hydrogenated diamond surface becomes a *p*-type electrical semiconductor[157-159] whereas the bulk diamond is an almost perfect insulator. Figure 2.6 shows the model of H-C(100) surface and the corresponding AFM image[160] of the surface showing the hydrogen atoms rows.

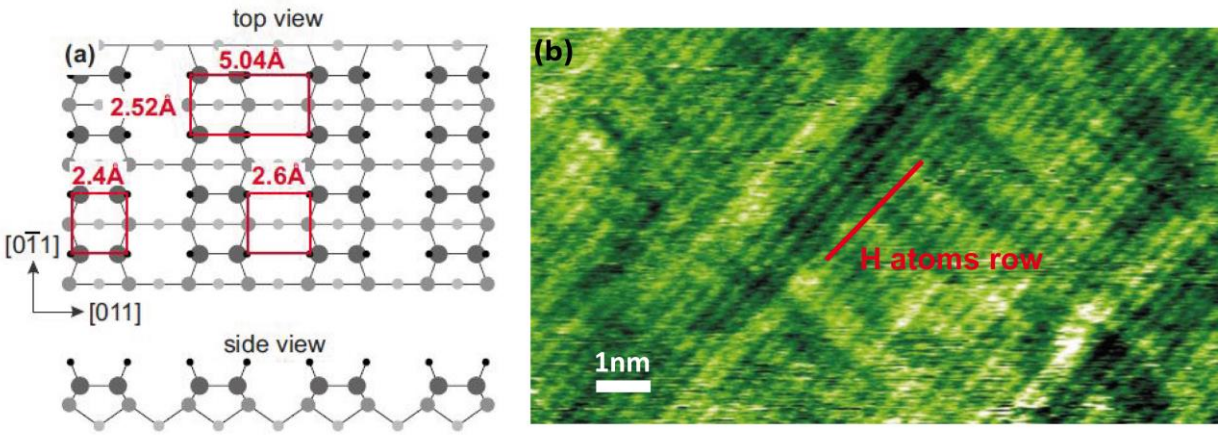

Figure 2.6 (a) Model of hydrogen terminated diamond H-C(100). (b) An AFM image of the H-C(100) surface in UHV condition.[160]

In this work, a high purity CVD diamond plate (*Element Six*, lateral dimensions: 4.5 × 4.5 mm, thickness: 500 μm) is used as the substrate for transferring graphene. Impurity concentrations of less than 1 ppb for nitrogen and 1 ppb for boron, and a surface roughness of less than 1 nm are an excellent basis to investigate electronic properties. First of all, the diamond substrate is cleaned with a mixed solution of hydrochloric acid (HCL, 36%, *VWR*) and nitric acid (HNO_3, 69%, *VWR*) followed by concentrated sulfuric acid (H_2SO_4, 96%, *VWR*) mixed with potassium nitrate (KNO_3, *Merck Millipore*). Oxidation of the substrate is conducted with an oxygen microwave plasma (*TePla 100-E*) for 300 s at 200 W load coil power and a pressure of 1.4 mbar. To ensure a high quality conductive termination, hydrogenation of the diamond surface is performed in a quartz tube reactor (*Seki Technotron Corp.*) of a microwave-coupled *ASTEX Plasma System* with three steps: first, the diamond substrate is heated to 700°C prior to exposure. At 700°C a constant hydrogen flow of 100 sccm at 50 mbar pressure is fed into the chamber. After ignition, the plasma is operated at a microwave power of 750 W for 15 minutes. To finish the process, the power is slowly decreased to 230 W at a reduced pressure of 10 mbar for 10

minutes to allow a slow continuous cool down, which has been found to be necessary for a high quality hydrogen termination.

Noncontact AFM (NC-AFM) image atomically reveals the individual hydrogen atom on the hydrogenated diamond (100) surface and the C-C dimers on the pure diamond (100) surface[160]. In contrast, STM is sensitive to the electronic structure whereas the AFM senses interaction forces. Thus, the AFM offers the potential of providing further structural details in cases where the electronic structure is delocalized. Figure 2.7 (a) shows the STM topography of the H-C(100) surface where rows correspond to CH-CH dimer[161] of the reconstructed surface[160], with average apparent roughness of ~ 0.5 Å on a length scale of 100 nm. The dimer rows run in orthogonal directions due to the existence of nm-sized surface domains. The spectrum depicted in Figure 2.7 (b) is obtained from the diamond surface with hydrogen termination and shows a zero-current inflection point at around -1.2 V in good agreement with previous studies from Lud *et al.*[162], which is tentatively assigned to the material's *p*-type doping.

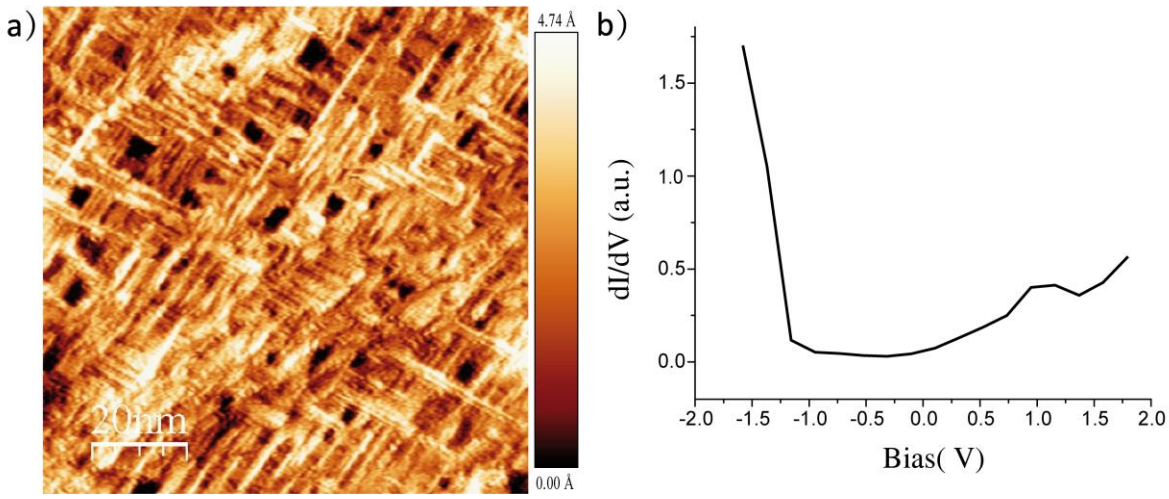

Figure 2.7 (a) High resolution STM image of a hydrogenated diamond surface obtained under ambient conditions with tunneling parameters of I_t = 8 pA, V_t = 300 mV. (b) Differential conductance *dI/dV* versus sample bias spectra for the hydrogenated diamond surface shown in (a).

2.1.5 Graphene/hydrogenated diamond (100)

Graphene is a single layer of carbon atoms, connected in hexagonal rings to form a 2D crystal. Its unique physical, mechanical, and electrical properties have drawn a lot of interest among scientists. Therefore, because its properties such as low resistivity, high transmittance and atomically flat, we chose it as a surface for hydrogenated diamond substrate to fabricate the optoelectronic device elements. In particular, the fabrication of graphene-based device provides an impetus to the planar sp^2-sp^3 carbon-on-carbon technology.[163, 164]

In order to obtain the graphene/hydrogenated diamond (H-C(100)) substrate used in this study as an atomically-flat, transparent interface, we transfer a single layer of CVD graphene sheet from the original copper foil to the hydrogenated diamond as followed as Figure 2.8. Polymethylmethacrylate (PMMA) is spin-coated on the CVD-grown graphene on Cu foil[165] and then the stack is cured on a hot plate at 100°C for 1 minute to fix. After that, the Cu foil is etched in the 0.1 M aqueous ammonium persulfate ($(NH_4)_2S_2O_8$) solution overnight, resulting in the PMMA/graphene layer delamination of the Cu foil. Afterwards, the PMMA/graphene film is transferred by a clean glass slice and rinsed in the distilled water to remove away the residual etchant and placed on the hydrogenated diamond substrate. The PMMA/graphene/diamond stack is air-dried overnight and then heated up to 55°C for 2 hours. In order to dissolve PMMA completely, the sample is dipped into acetone at 55°C for 1 hour and overnight at room temperature. Because the PMMA residual exists even after cleaning by acetone or NMP, the CVD graphene transferred on H-C(100) diamond (G/H-C(100)) features limited roughness at the micrometer scale. In this regard, annealing is also performed to reduce the PMMA residual and improve the surface quality.

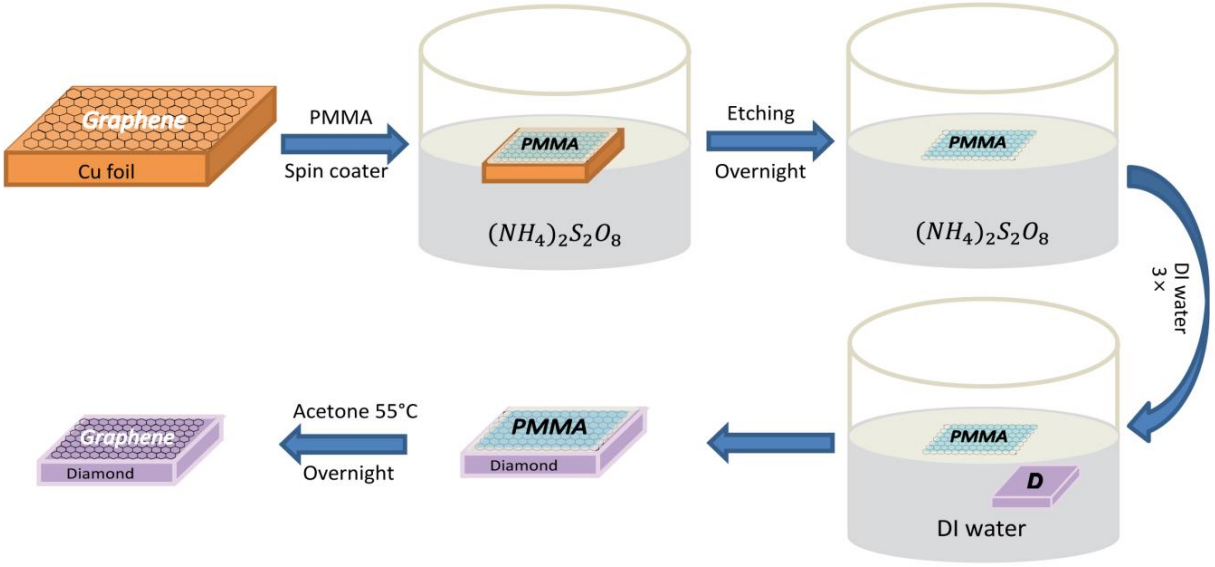

Figure 2.8 Illustration for the transfer process of a CVD-grown graphene film.[23] PMMA is spin coated on a graphene layer and cured at 100°C for 1 minute. The PMMA/graphene membrane is then detached from the substrate in aqueous ammonium persulfate bath and subsequently deposited on the target substrate. Finally, the PMMA is dissolved using acetone at 55°C for 2 hours and then rinsed in room temperature acetone overnight.

After cleaning the graphene sheet and transferring, as shown in Figure 2.9 (a), G/H-C(100) surface features a much lower roughness, making it ideal for long-range macroscopic patterning of molecularly precise self-assemblies for optoelectronic device fabrication. Differential *IV* curves for graphene are presented in Figure 2.9 (b). Compared with diamond STS, the G/H-C(100) conductance signature exhibits a clearly different behavior with a rather symmetric onset of the transport characteristics.

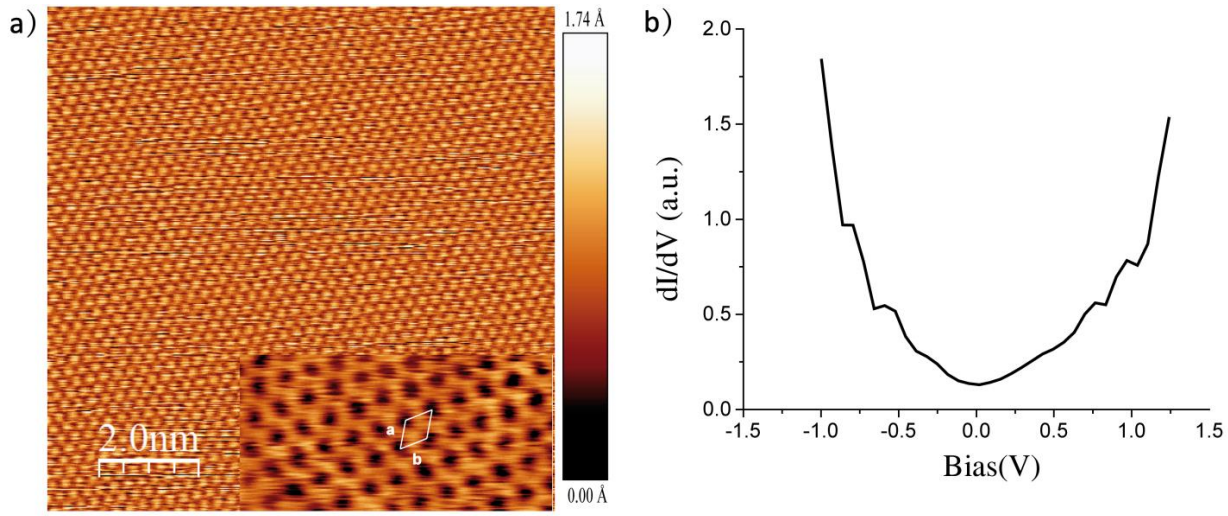

Figure 2.9 (a) STM image of transferred CVD-grown graphene on the hydrogenated diamond surface with tunneling parameters of I_t = 80 pA, V_t = 20 mV. Inset: Close-up of honeycomb structure of graphene with the unit cell of a = 2.37 ± 0.1 Å and b = 2.43 ± 0.1 Å (b) Differential conductance *dI/dV* versus sample bias spectra for the G/H-C(100) template shown in (a).

2.2 Adsorbates

2.2.1 Azobenzene-SAMs

To form layers of azobenzene on a surface, we combine azobenzene molecule with other chemical groups, to form derivatives, which allow the molecules to bond on the desired surfaces like gold. There are plenty of such derivatives reported, for example $HSC_{11}H_{22}O$-azobenzene or $HSC_6H_{12}O$-azobenzene.[166] Among these derivatives, azobenzene moieties with an alkyl chain underneath are very common. In our case we use a HS-C_6H_{12}-O-azobenzene derivative, which will be referred to HS-C_6 azobenzene or just azobenzene for simplicity.

Self-assembled monolayers (SAMs) are organic assemblies with crystalline structures of molecules, which have organized spontaneously after they adsorbe on the target surface. In order to form the azobenzene-SAMs, we mix the azobenzene molecules with 6-mercapto-1-hexanol

molecules named as spacer molecules, to create enough space to allow the azobenzene molecules to undergo the conformation switching. Our azobenzene molecules consist of an azobenzene part and an alkyl chain. The alkyl chain has the same number of carbon atoms as the spacer molecule, therefore it has roughly the same length. It is reported that these spacer molecules provide enough space for the above located azobenzene parts to switch.[167] The schematics of azobenzene and spacer molecules are shown in Figure 2.10. Referring to the spacer molecules (6-mercapto-1-hexanol), the HS-group is the head group, which can covalently bond on a metal substrate, the tail is an alkyl chain (C_6H_{12}) and a hydroxyl group forms the end group. Because of its simple preparation and the high ordering degree of the molecules, SAMs have found applications in numerous systems and became an important tool in nanophysics.[146]

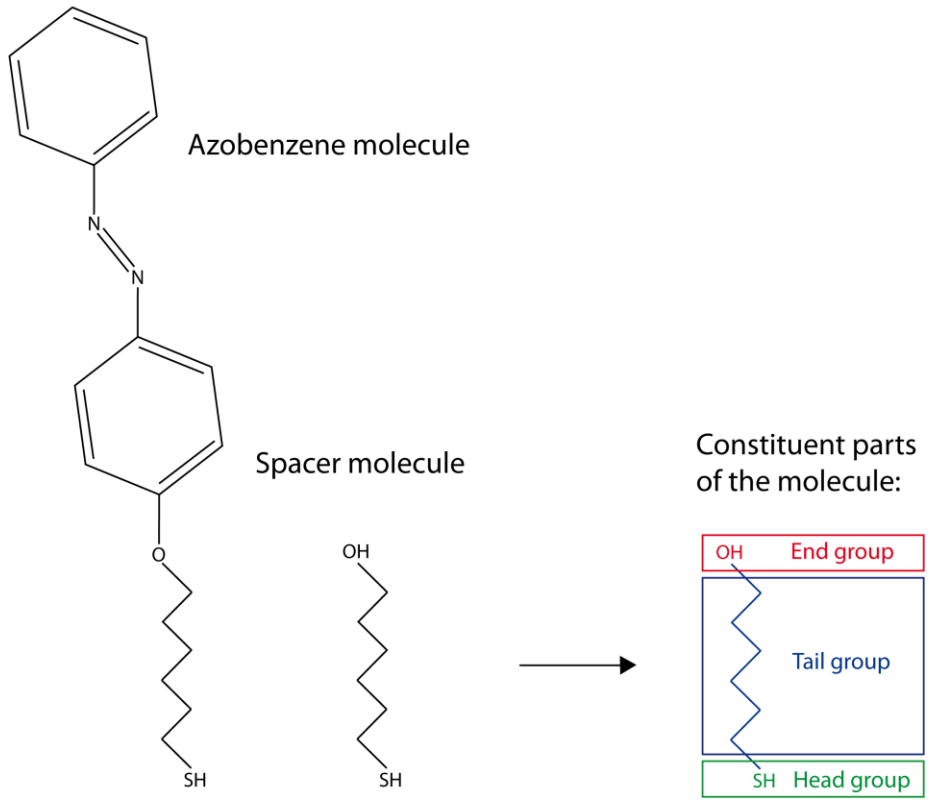

Figure 2.10 Chemical structures of azobenzene and spacer molecule. Chemical valence-bond structures of azobenzene and spacer molecule are depicted on the left side and the different constituent parts of SAM-forming molecule are shown with the example of a spacer molecule on the right side.

In order to fabricate a monolayer of azobenzene molecules, the surface of the gold substrate which as introduced in section 2.1.2 must be as smooth as possible. First of all, the intensive cleaning of the gold substrate is important to avoid contamination. The quality and the reproducibility of the SAMs layer depend on the level of cleaning for the substrate. Here, a piranha solution is used to remove the organic contaminations from the gold surface. Figure 2.11 shows the steps of the surface functionalization which includes the preparation method. Here, the piranha solution is prepared as a mixture of distilled water with 31% hydrogen peroxide (H_2O_2) and ammonium hydroxide (NH_4OH) in a ratio of 5 : 1 : 1. Since the piranha solution is extremely corrosive upon contact with the skin or eyes, all experiments are performed under the fume hood. The piranha solution is heated up to 80°C by using a hotplate and the samples are placed into the solution for 6 minutes. It is observed that some bubbles from the gold surface start to arise immediately after the sample is placed into the solution. Subsequently, the samples are taken out, washed with distilled water and dried with a dry nitrogen gun and heat at 120°C for 10 minutes in the end.

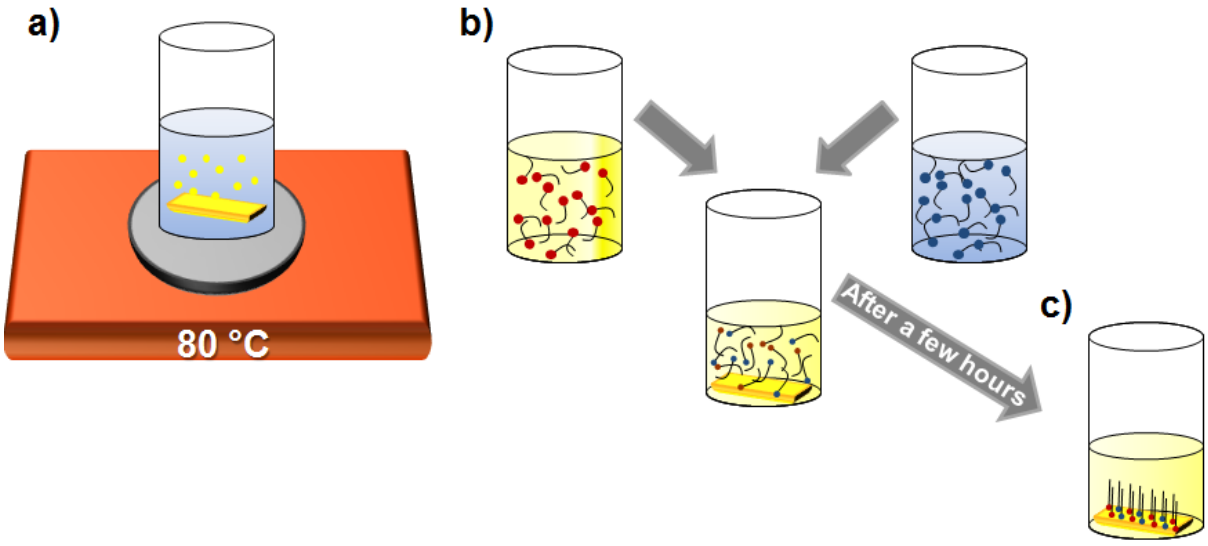

Figure 2.11 Functionalization of gold surfaces with azobenzene-SAM. (a) Cleaning of the gold surface by piranha solution. (b) Preparation of the mixture of azobenzene and spacer molecules. (c) Formation of mixed azobenzene-SAMs after 8-10 hours.

Meanwhile, the mixture of the azobenzene-SAM molecules is prepared as shown in Figure 2.11 (b). The HS-C_6 azobenzene molecules are acquired from *Prochimia Surfaces Company*. To obtain 1 mM mother solution, 7.3 mg powder of azobenzene is mixed with 25 ml of tetrahydrofuran (THF) solution. THF is an organic and colorless solution which is generally used to dissolve both nonpolar and polar chemicals. A SAMs of the azobenzene molecules only would constrain the molecular switching capability because they are too densely bonded on the surface. Herein, a mixture of the azobenzene molecules with spacer molecules is used, that is 3.2 µl of liquid 6-mercapto-1-hexanol spacer molecules are mixed with 25 ml of tetrahydrofuran (THF) solution to obtain 1 mM solution. Afterwards, the samples are submerged into this mixture solution containing the azobenzene solution and spacer solution with a volume ratio of 1 : 1. This is the final step used to functionalize the sample. The process to form the monolayer on the surface involves two stages. The first stage is grafting of the SAMs on the surface which takes a few minutes; the second step is a slow reorganization step which may last in hours (Figure 2.11 (c)). To enhance the quality and get a uniform distribution of the SAMs, the samples are kept in the solution for 8 - 10 hours. Finally, to finish the process, the samples are gently sonicated for 10 minutes in pure ethanol to remove the possible multilayers of molecules. The functionalization process is done in a clean room and all the samples are stored in a nitrogen box to avoid any further contamination.

2.2.2 Supramolecular 2D networks

In this thesis, we designed two different bicomponent nanoporous network structures bonded by hydrogen bonds for self-assembling by scanning tunneling microscope (STM) on HOPG and all-carbon transparent and atomically flat hybrid platforms, i.e., commercial graphene (G) on copper foil and monolayer graphene transferred on a hydrogenated diamond H-C(100) surface. One of the networks is a model system formed by the organic semiconductor naphthalenetetracarboxylic diimide (NTCDI) and melamine (Mel). The second target network is built with a chromophore, consisting of a terrylene diimide derivative (TDI) and melamine (Mel).

2.2.2.1 Melamine and NTCDI

Assemblies in the form of two-dimensional open networks are of particular interest for possible applications because well-defined porous structures can be employed as host templates for the precise localization and confinement of guest entities such as molecules or clusters, which can add functionality to the supramolecular network.[48] The driving forces for self-assembly of well-ordered supramolecular architectures are the intermolecular and molecule-substrate interactions. Melamine and 1,4,5,8-naphthalene tetracarboxylic diimide (NTCDI) are used to form a bi-component nanoporous network structure via hydrogen bonds. The molecular structures are given in Figure 2.12. Melamine is often used in supramolecular chemistry because of its planar conformation, highly symmetrical triangle shape and ease in forming hydrogen bonds for constructing a molecular self-assembly with other molecules under various conditions.[168] NTCDI is an aromatic diimide which is often used for novel molecular assemblies and supramolecular arrays due to its role as electron acceptor.[10] Therefore, each melamine is linked to three NTCDI molecules through triple hydrogen bonds.

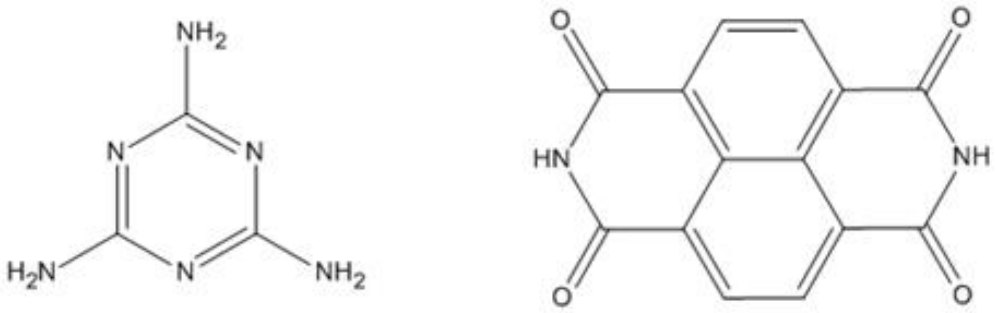

Melamine NTCDI

Figure 2.12 Chemical structures of melamine and naphthalene tetracarboxylic diimide (NTCDI).

Melamine (*Fluka*, *52549*, 99% and *Alfa-Aesar*, *A11295*, 99%) and 1,4,5,8-naphthalenetetracarboxylic diimide (NTCDI, *TCI Chemicals Europa*, *N0536*, 97%) were used as received. Anhydrous 1,2,4-trichlorobenzene (TCB, *Sigma-Aldrich*, 99.9%) and dimethyl sulfoxide (DMSO, *Sigma-Aldrich*, 99.9%) were used as solvents without further purification. The

mother solutions in DMSO were heated to 80°C and the diluted solution series were all prepared in 1,2,4-trichlorobenzene. All of the bilayer formations were observed after few minutes in solutions with several concentration ratios of 2 μM : 5 μM, 5 μM : 8 μM and 8 μM : 12 μM. Besides, methanol (*Alfa-Aesar*, 99.9%) was added to these solutions in some additional experiments. The self-assembly networks were obtained by drop-casting 5 ± 1 μL on the respective surface. Scanning tunneling microscope (STM, *Agilent Technologies 5100*) in constant current mode under ambient conditions was used to probe the bicomponent molecular self-assembly. The scanning tips were prepared by mechanically cutting a Pt/Ir wire (80 : 20%, *Goodfellow*). STM data were analyzed with WSxM software (*Nanotec Electronica S.L.*). Supramolecular bicomponent network based on NTCDI bridging melamine via triple hydrogen bonds was prepared in a solvent mixture of 1,2,4-trichlorobenzene/dimethylsulfoxide by dropping 6 μL on HOPG (0001). The molecular self-assemblies were spontaneously accomplished at the liquid phase under ambient conditions. A mixture solution of melamine : NTCDI (5 : 12 μM) was used to study the equilibrium state at the solid-liquid interface on HOPG initially. This concentration of solution was chosen due to the formation of a long range highly ordered pattern with a honeycomb structure.

2.2.2.2 Melamine and TDI

For the second hydrogen bond network, we chose melamine and TDI molecules as adsorbates. The network is built with a chromophore, consisting of the TDI derivative which chemical structure is shown in Figure 2.13.

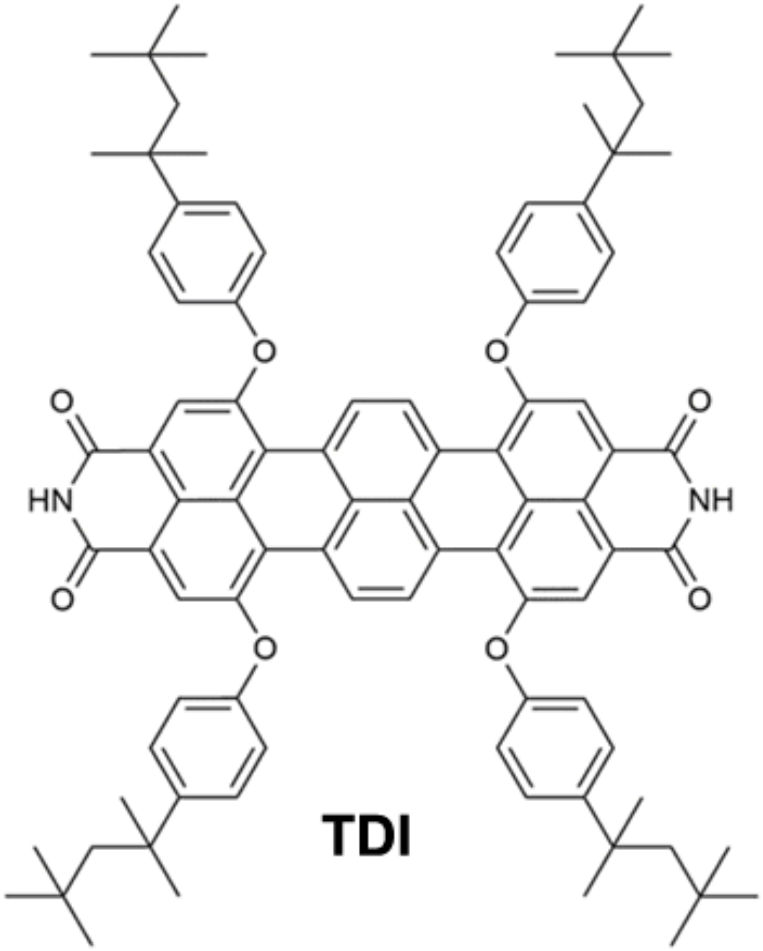

Figure 2.13 Chemical structures of terrylene diimide tetracarboxylic acid derivative (TDI).

The preparation process of melamine is as same as mentioned in section 2.2.2.1. Heteromolecular recognition between tritopic melamine and complementary ditopic linkers via hydrogen bond formation is introduced to achieve the highly crystalline hexagonal supramolecular architectures[169]. By proper chemical design, the complementary linker can be engineered[170, 171] to self-assemble to the architectures, decreasing the existence of poorly ordered and glassy phases. For instance, the peripheral substitution of the linker favors the formation of networks over tightly-packed patterns have previously shown.[172] Furthermore the linker can be imbued with specific functional properties. Rylene dyes are poly(peri-naphthalene)s[83] showing a high photostability[173] which make them become the preferred molecules for optoelectronic

devices application. Extending the π-system of the molecule allows for tuning its optical properties and shifting the absorption maximum to the higher wavelengths. Since rylenes are known to be amongst the most efficient organic absorbers[83, 174], thus, they become the promising candidates for infrared photovoltaics with high transparency in the visible spectrum to use in the next generation of façade and window building technology[175]. By introducing diimide terminations, the rylene molecules acquire the supramolecular moiety necessary for triple hydrogen bonds complementary recognition with the melamine cornerstone. Substituents at the bay position of the rylene molecules are used to improve the solubility[83] and favor porous structure formation. Accordingly, a novel terrylene diimide (TDI) bearing NH groups in the imide structure was provided by MPIP Mainz according to Figure 2.14. The NH groups make the solubility of the molecule poor and the purification of the rylene dyes is rather difficult. Therefore we use bulky 2,6-diisopropylphenyl groups in the starting "one-pot" reaction of perylene monoimide **1** and naphthalene monoimide **2** to create the soluble compound TDI **3**. After bromination and phenoxylation steps, tetra(t-octylphenoxy) substituted **5** is obtained with an outstanding solubility[176]. Hydrolysis of the imide groups under basic conditions results in bis-anhydride **6**, which is reacted with ammonium acetate to afford the target TDI **7**. In both cases, the purification and processing are possible due to the presence of four voluminous *t*-octylphenoxy groups. Comparing with the soluble perylene diimide analogues, TDI has higher absorption coefficient, which render it better light-harvesting efficiency[177]. Moreover, the additional naphthalene unit in the TDI molecule separates the tetraphenoxy groups and makes the TDI molecule less twisted.[178] Thus, improved planarity and increased absorptivity[83, 174] make the engineered TDI supramolecular assemblies advantageous over shorter PDI assemblies[48, 169].

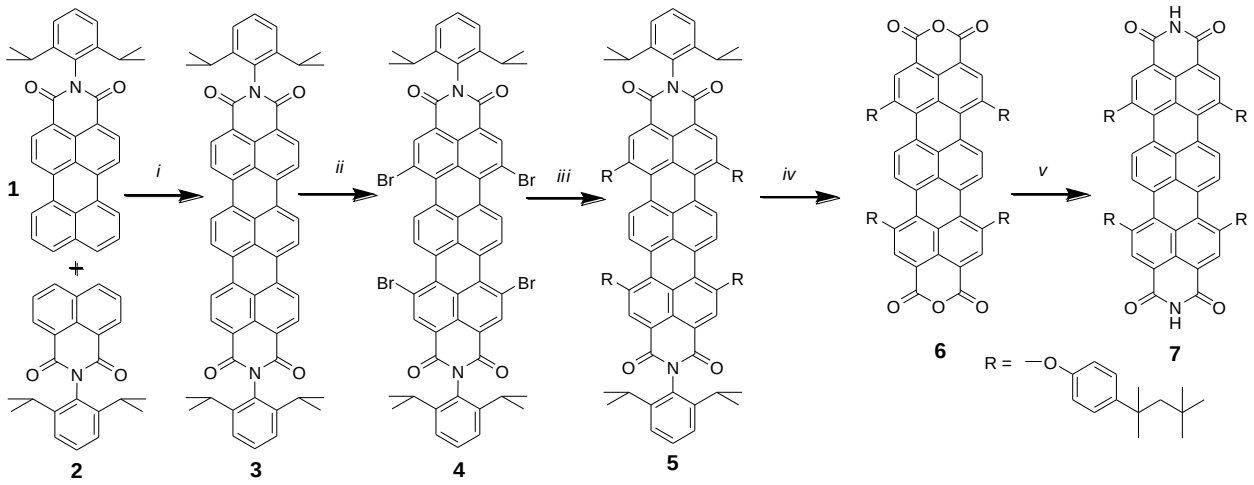

Figure 2.14 Synthesis of novel terrylene diimide TDI **7**. i-iii. Synthetic steps have been detailed elsewhere[176]. iv. KOH, KF, 2-methyl-2-butanol, reflux, 53%. v. Ammonium acetate, propionic acid, reflux, 20%.

2.3 Fabrication of transistor devices

The following section shows the techniques for fabricating the transistor devices based on 2D materials like graphene, MoS_2 and molecular self-assemblies. The electrodes' fabrication method consists on optical lithography, metallization and lift-off. Afterwards, the mono- and multi-layer 2D materials can be transfered/assembled on top of well-defined electrodes.

2.3.1 Electrodes fabrication

For device manufacturing several processing procedures are necessary which consist of optical lithography, metallization and lift-off. The interdigitated or squared electrodes fabrication process by means of top-down optical lithography techniques is shown in Figure 2.15.

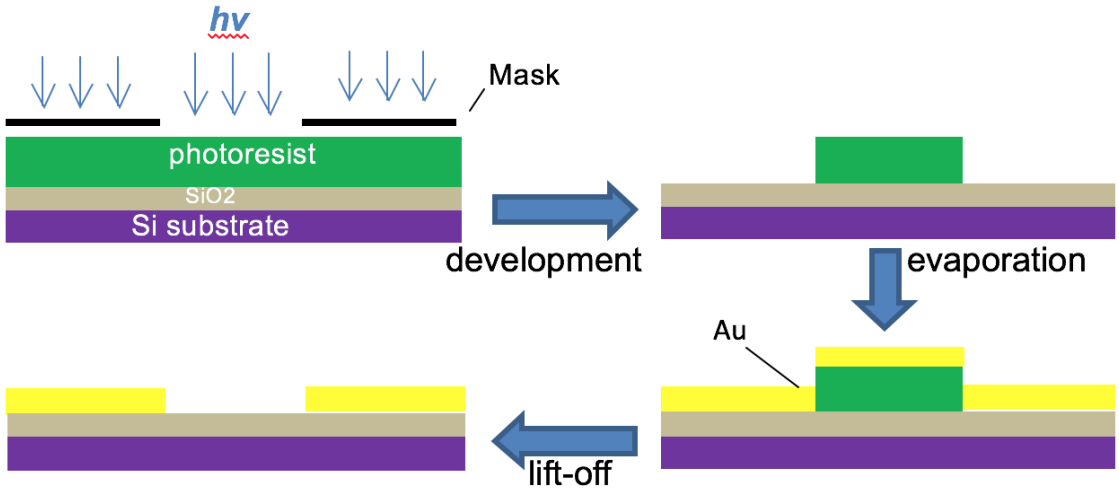

Figure 2.15 Processing steps for electrodes fabrication using an image reversal resist.

Optical lithography

To get two micron electrode channel lengths structures on Si/SiO_2 substrate or diamond substrate, a well-cleaned substrate is very important. A successful optical lithography process contains three main parts - photoresist spin coating, UV exposure and development. Firstly, the sample is cleaned with ultrasound in acetone, isopropyl and distilled water for 15 minutes respectively. To remove the potential water film and enhance the photoresist adhesion on the target substrate, it is necessary to heat the sample on the hot plate at 120°C for 5 minutes. It is noteworthy that the diamond sample has to be oxidized by an oxygen microwave plasma with a power of 200 W for 5 minutes after cleaning. A positive photoresist profile has a positive slope of 75 - 85° depending on the process conditions and the performance of the exposure equipment. This is mainly due to the absorption of the photoactive compound which attenuates the light when penetrating through the resist layer (so called bulk effect). The result is a higher dissolution rate at the top and a lower rate at the bottom of the resist. Hence, for our case of tiny structures, the image reversal photoresist *AZ 5214E* is chosen. When *AZ 5214E* is processed in the image reversal mode this is reversed as higher exposed areas will be crosslinked to a higher degree than those with lower dose. The final result will be a negative wall profile ideally suited for lift-off. After spin-coating at a spin rate of 6000 rpm, we soft-bake the spin-coated photoresist on a hot plate at 110°C for 1 minute guarantees fixing the resist on the substrate. The control of

temperature and time in the soft bake process is critical for next steps that could influence the quality of the final pattern. Then under soft contact mode, photoexposure of the whole sample under mask is carried out for 1.85 s. Subsequent hard bake at 120°C can make the exposure areas thermally crosslinked and insoluble in the developer solution. Then, we apply a flood exposure over 30 s and immerse the substrate into a standard developer solution, i.e. *AZ 400K*, 1 : 4 diluted, for 35 s. A part of the substrate's resist can be removed, another part (that exposed to a high temperature) will be remained with the resist thermally crosslinked on it. The flood exposure is absolutely uncritical as long as sufficient energy is applied to make the unexposed areas soluble. After development, the bare silicon/diamond surface is oxidized by a 200 W oxygen microwave plasma at 1.4 mbar, which is expected to improve metal adhesion. Figure 2.16 (a) and (c) shows optical micrographs of 2 micron structures on Si/SiO_2 and 20 micron structures on diamond after development respectively.

Metallization and lift-off

A 10 nm titanium and 50 nm thick gold layer are deposited by electron beam evaporation, whose process is already explained in section 2.1.2. Electron beam evaporation seems to provide better adhesion to the surface and is therefore used preferentially. In order to remove the gold parts except the electrodes, we have to lift-off the metal where it has photoresist underneath. Since the photoresist can be removed with some chemical solvent, we can easily lift the metal off by rinsing the whole sample in acetone. The sample is dipped into acetone and washed by an acetone flow in a strong flux with a plastic pipette for several minutes. The optical microscope is used to check the result of the electrodes after lift-off. The remaining resist can be removed with a hot N-Methyl-2-pyrrolidone (NMP) solution, followed by a careful rinse in isopropyl alcohol. Using an image reversal resist allows to fabricate resist structures with significant undercut, enabling a lift-off without applying any mechanical force to the metal structure deposited on the surface. After successful lift-off process, the samples are cleaned with acetone, rinsed with isopropyl alcohol and dried with nitrogen. The final interdigitated gold electrodes on Si/SiO_2 and squared electrodes on diamond are shown in Figure 2.16 (b) and (d) respectively.

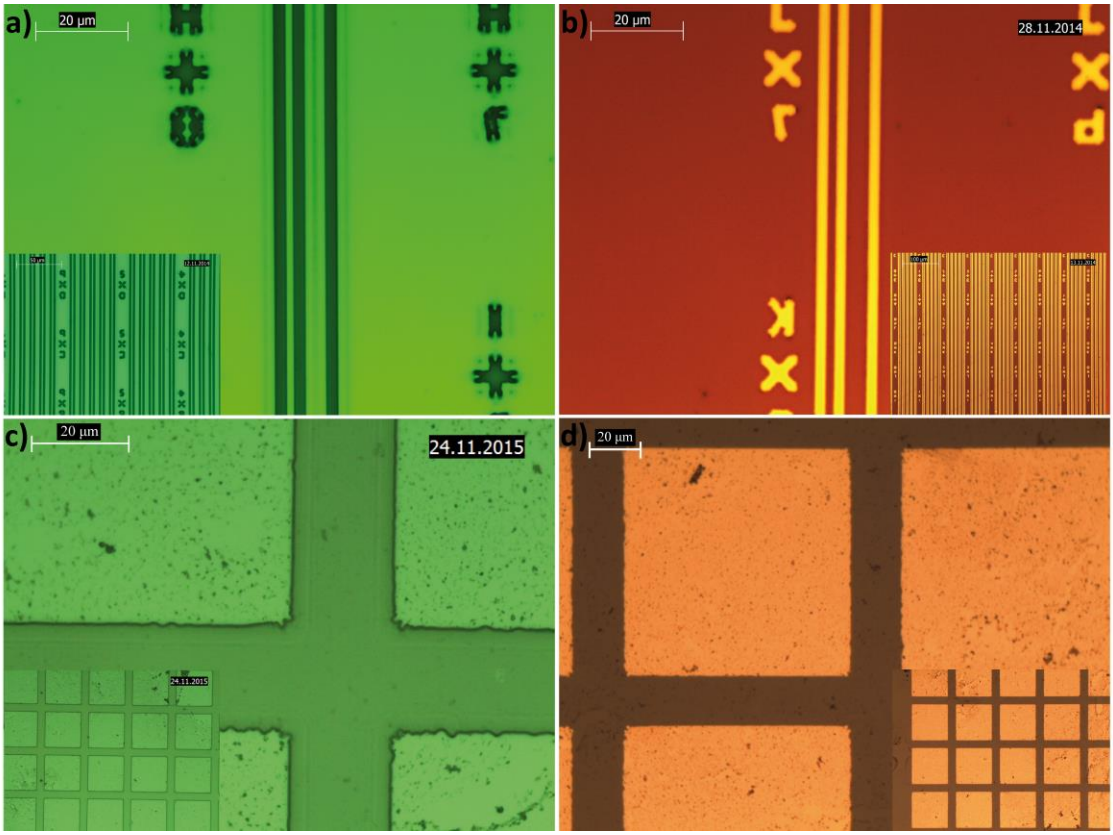

Figure 2.16 (a) Optical micrograph of 2 micron structures on Si/SiO_2 after optical lithography and development. (b) Optical micrograph of the final interdigitated gold electrodes on Si/SiO_2 after metallization and lift-off. (c) Optical micrograph of 20 micron structures on diamond after optical lithography and development. (d) Optical micrograph of the final squared gold electrodes on diamond after metallization and lift-off. Insets: the large scale of ordered electrodes after development and metallization respectively.

2.3.2 Exfoliation and transfer of MoS_2 flakes

In this thesis, we transferred graphene and MoS_2 flakes with this special technique successfully. Here we only illustrate the transfer process of MoS_2 flake as an example of 2D crystals. In Figure 2.17, a near-to-monolayer MoS_2 flake is precisely localized between three electrodes. The transparent part of the material is 2 - 3 layers MoS_2 flake and the left orange part

is a multilayer MoS_2 flake. The near-to-monolayer is on top of three gold electrodes which have the minimum distance of two micron. The MoS_2 exfoliation and transfer is depicted in details below.

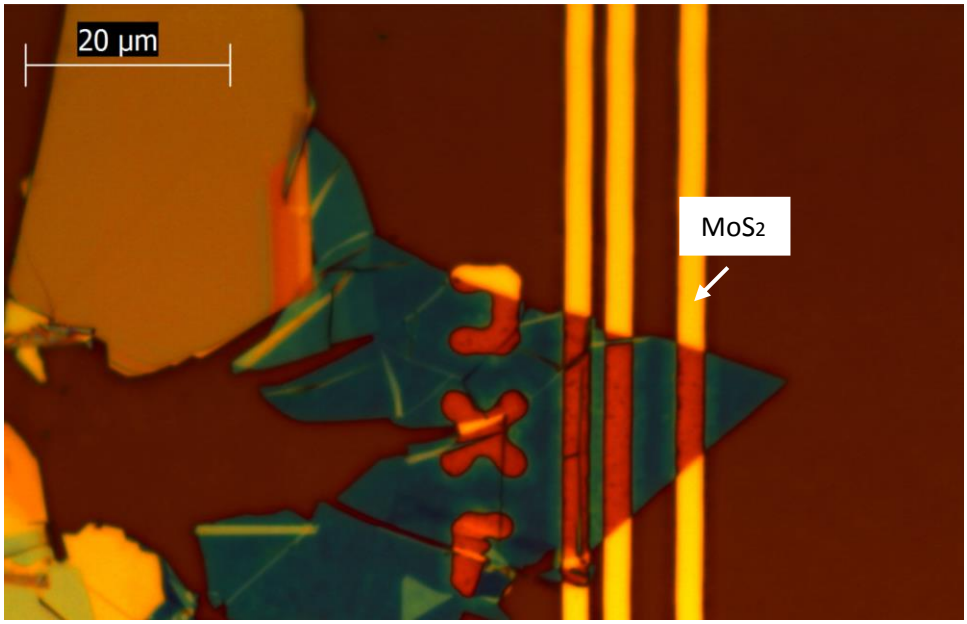

Figure 2.17 Optical micrograph of MoS_2 flake localized between three electrodes with a minimum distance of 2 micron.

The basic idea and the method to exfoliate single atomic layer of MoS_2 is the "scotch-tape" technique that derived from the way to obtain a very high quality of graphene sheet. The necessary components are a scotch tape, plastic tweezers, a clamp and a piece of bulk crystal. MoS_2 is detached from a bulk MoS_2 crystal by using adhesive tape. After peeling it off, the bulk MoS_2 crystal, multiple-layer of the MoS_2 remains on the tape. Then, the scotch tape is pressed together with a new piece of tape. The tapes are aligned between two coverslip, by using the clamp, to get a uniform pressure on the flake and left for 5 minutes every time. The peeling process is performed with an exfoliator to increase the flake size as well as to remove the tapes slowly and simultaneously. MoS_2 is cleaved into several flakes of few-layer MoS_2 by repeating the peeling process of the multiple-layer of MoS_2. Not only the flake thickness is getting thinner, but also the flake size is getting smaller after every each peeling process. Hence, depending on the initial exfoliation step, the optimum number of exfoliation changes. After enough repeated

exfoliation processes, the last exfoliated tape is attached to a PDMS film with the size available for the mask sample in a way described above and left for 15 minutes. Finally one last peeling is done and the tape is removed from the sample very fast. The obtained flakes show significant difference with respect to size and thickness. Here, the sizes range from nanometers to several tens of micrometers for single-layer MoS_2, depending on the preparation. The different layers of flake can be roughly recognized by the optical microscope. Furthermore, in order to exactly identify the number of flake corresponding to the contrast difference, we can use atomic force microscope (AFM) to check the thickness with a height profile on the flake as a reference.

Once the target MoS_2 flake on PDMS film is found under optical microscope, we mark the approximate position of the flake by the focused light and take some photos of magnifying target flake. In order to transfer the target flake from PDMS film to functionalized mask sample, mask aligner is an important tool to perform this process accurately. Firstly, the PDMS film is pasted around the middle of a glass plate, which can be vacuumed by the mask aligner and making sure the flake is on the top side. Meanwhile, we position the functionalized mask sample in the middle of the internal sample holder of mask aligner under the separate mode. We focus the target flake on the mask sample under the microscope on the mask aligner and lift up the sample holder carefully by height screw knob until the PDMS film stick on the sample gradually. We wait for a while very slowly separate the sample away from the PDMS film by screwing the height knob down. The transfer and separation of the PDMS film and sample can be easily judged by the color of sample under optical microscope. When the sample is completely separated from the PDMS film, we can take it out and mark the flake position on the mask sample in detail for the following current measurements on the flake transistor. In the end, to measure this micron device, we have to bond the contact pads of the device onto an electrical chip. For room-temperature applications, the sample is fixed into the carrier with double-sided adhesive tape. Silver conductive paste is used as glue for low-temperature experiments. Subsequently, the samples are wire-bonded by ball or wedge bonding.

Chapter 3

Bilayer Nanoporous Networks of Melamine and NTCDI

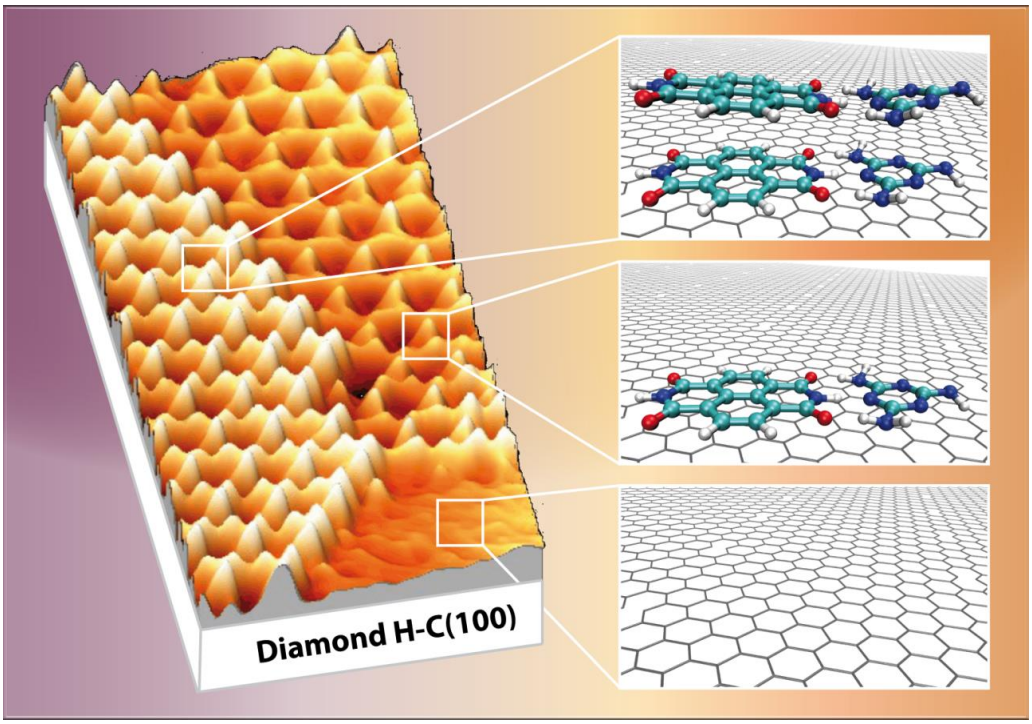

Figure 3.1 3D models of melamine and NTCDI nanoporous network self-assembled on a graphene-diamond, all-carbon, atomically flat and transparent platform.

Extending molecular self-assembly from two- to three-dimensions is an important nanofabrication technique with atomic precision en route to molecule-based electronic components and devices. In this chapter, we design a three-dimensional bicomponent supramolecular architecture on an all-carbon sp^2-sp^3 transparent platform. The platform consists of hydrogenated diamond decorated with a monolayer graphene sheet. The pertaining bilayer assembly of melamine (Mel) and naphthalenetetracarboxylic diimide (NTCDI) supramolecular network exhibiting a nanoporous honeycomb structure is explored via scanning tunneling microscope (STM) initially at the solution-highly oriented pyrolytic graphite (HOPG) interface. On both graphene-terminated copper and an atomically flat graphene/diamond hybrid substrate, an assembly protocol is demonstrated yielding similar supramolecular networks with long-range order. The results suggest that hybrid platforms, (supramolecular) chemistry and thermodynamic growth protocols can converge as a form of *in situ* molecular device fabrication.

3.1 The network of melamine and NTCDI at the solution-HOPG interface

The assembly of the supramolecular bicomponent network[179] based on 1,4,5,8-naphthalenetetracarboxylic diimide (NTCDI) bridging 1,3,5-triazine-2,4,6-triamine (melamine) is first performed on a freshly cleaved HOPG surface in equilibrium with different solutions, in order to investigate the propensity of 3D-vdW stacking similar to previously reported studies[20, 180]. A possible strategy to favor hydrophobic 3D-vdW stacking relies on increasing the polarity of the solvent used for the molecular self-assembly. However, only network architectures without obvious 3D signature are observed when using solutions of up to 20% volume in methanol (Figure 3.2 (a)), as previously reported[179]. In contrast, when using the pristine desiccated solvents for molecular self-assembly (TCB and << 1% DMSO), a bilayer network architecture is easily recognized in Figure 3.2 (b) and the NTCDI-pairing domain boundaries are observed in most places on the image. It can be easily observed that a bilayer starts to form during 2D self-assembling even at sub-monolayer coverage and the formation was investigated at the solid-liquid interface on HOPG by time-controlled experiments. Figure 3.2 (d) shows a time lapse

sequence of STM data, whereby the bilayer crystal growth can be estimated as 1.3 ± 0.3 nm^2 s^{-1} per nm of island perimeter length, or 0.8 molecules nm^{-1} s^{-1}.

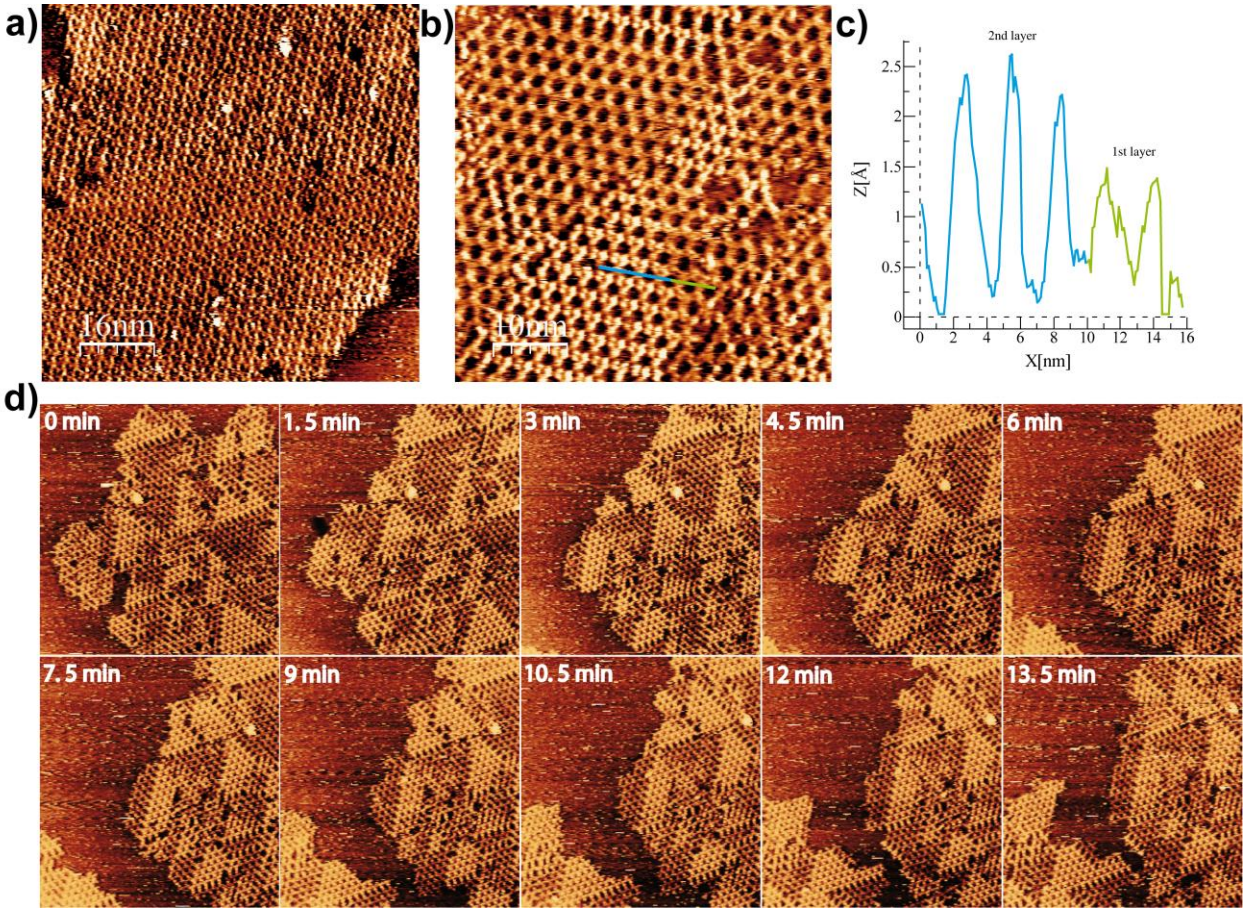

Figure 3.2 (a) STM image of a long-range mono-crystal domain of melamine-NTCDI network. The patterns are from the solution of 6 µL melamine-NTCDI (8 µM : 12 µM) and 20% methanol. Tunneling parameters: I_t = 20 pA, V_t = 300 mV. (b) STM image where a bilayer network (the area drawn the colored lines) without a NTCDI-pairing domain boundary has been located, from a sample preparation without 20% methanol. Notice that NTCDI-pairing domain boundaries are observed in most places on the image. Tunneling parameters: I_t = 20 pA, V_t = 300 mV. The ratio of melamine and NTCDI is 5 µM : 8 µM. (c) Cross-sectional line profile corresponding to the colored solid lines shows different layers (green: first layer; blue: second layer) in (b). (d) Time lapse of STM images depicting the apparent evolution of bilayers on methanol-free solution preparations.

A closer insight is necessary to understand the domain boundary of the bilayer architecture. A large area of a bilayer nanoporous network structure is shown in the STM image in Figure 3.3 (a). A domain boundary along the edges of the bilayer was clearly observed. Such ordered bilayer network of bicomponent molecular assemblies on HOPG surface indicates its stability due to the balance of intermolecular and molecule-substrate interactions. A bilayer formation is observed indicating that a second layer growth is energetically preferred prior to a monolayer structure covering the whole surface. Because the domain boundaries are immobile and the bilayer does not overgrow single layers, we conclude that it preferentially expands as a bilayer. Consequently, whenever the surface shows NTCDI-pairing defects - and hence a domain boundary - the bilayer growth terminates. In Figure 3.3 (b) a close-up of the bilayer domain boundary formed by NTCDI dimer in the first layer is shown. From topographic images, melamine molecules appear darker than NTCDI molecules due to its lower density of states,[181] thus every tetramer made up of one melamine and three NTCDI molecules in a ring structure looks like three spots. The existence of the second layer network which appears brighter is confirmed by the line profiles in Figure 3.3 (c). The HOPG substrate, first layer and second layer of the network are depicted by red, green and blue curves, respectively. It can be observed that in the STM topographic image the apparent height of the second layer with respect to HOPG is twice (~ 2 Å) the distance between the first and second layer (~ 1 Å). Notably, the high resolution in Figure 3.3 (b) allows to resolve empty pores in the line profiles (blue line Figure 3.3 (c)). Such height differences are also seen in architectures without domain boundaries, where a seamless 3D-to-2D transition to single layer islands occurs (Figure 3.2 (b)).

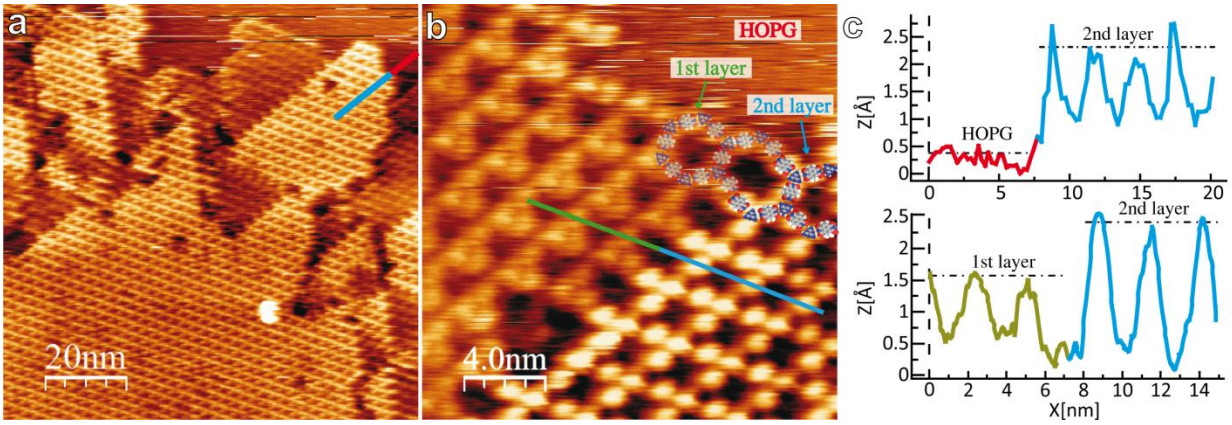

Figure 3.3 (a) Large-scale STM image of bilayer network of melamine-NTCDI on HOPG. (b) Close-up view of bilayer domain boundary showing NTCDI dimer interaction in the first layer. (c) Cross-sectional line profiles with different colors corresponding to the solid lines in (a) and (b). In the graphs, the height of substrate, first layer and second layer are depicted by red, green and blue colors, respectively. Tunneling parameters in all STM images: I_t = 20 pA, V_t = 300 mV. The concentration ratios of melamine and NTCDI are 5 µM : 8 µM using TCB solutions with low DMSO content.

Referring to these bilayer structures, high resolution STM images of the first and the second layer are shown in the Figure 3.4 respectively. Figure 3.4 (a) shows the first layer of melamine-NTCDI network at TCB/HOPG interface with the unit cell parameters of a = 2.82 ± 0.1 nm, b = 2.75 ± 0.1 nm and the pore size is 1.82 ± 0.1 nm. Meanwhile, the tetramers in the second layer of melamine-NTCDI network at TCB/HOPG interface are shown in Figure 3.4 (b).

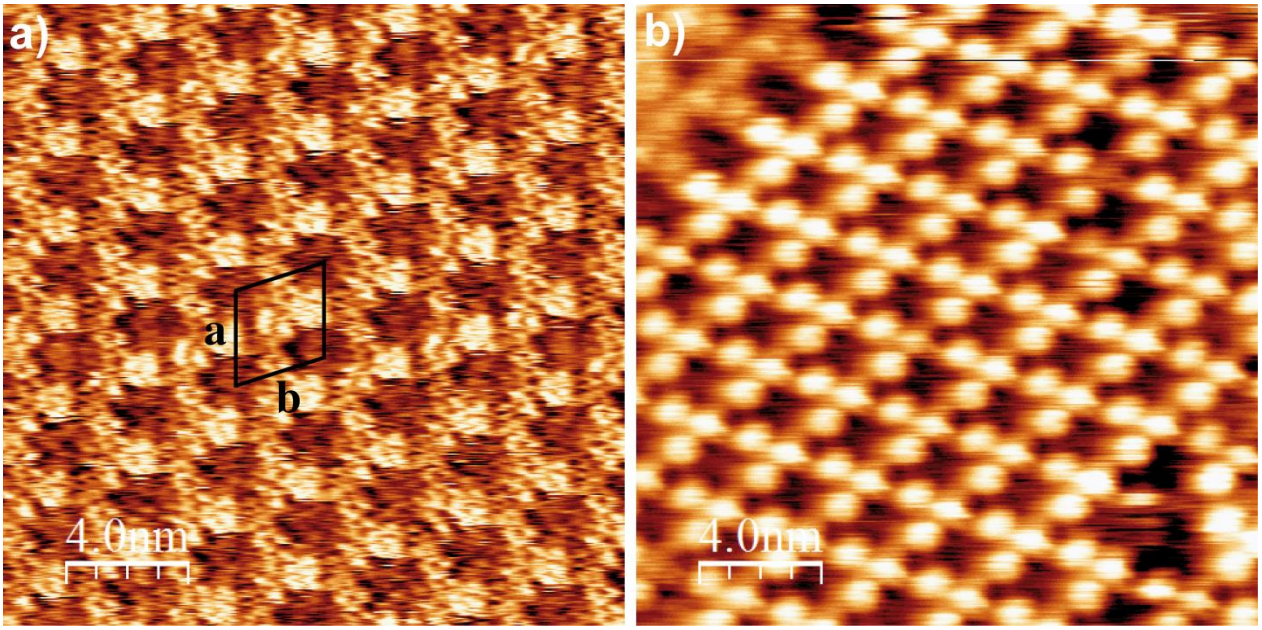

Figure 3.4 (a) High resolution STM image showing the first layer of melamine-NTCDI network at TCB/HOPG interface. (b) High resolution STM image showing the tetramers in the second layer of melamine-NTCDI network at TCB/HOPG interface. Tunneling parameters for all images: I_t = 20 pA, V_t = 300 mV. The ratios of melamine and NTCDI are: (a) 17 µM : 37 µM (b) 5 µM : 8 µM.

STM images with enhanced molecular contrast of the bilayer domain boundary are depicted in Figure 3.5 (a) (b) and illustrate the mechanism of molecular arrangements and the intra- and inter- molecular interactions. As shown by the molecular models in Figure 3.5 (b), (c), (d), every triple hydrogen bond between melamine and NTCDI, two NH⋯O and one NH⋯N, is formed via the combination of the diimide termination on both ends of the NTCDI molecule and melamine.[181] Interestingly, the molecular models shown in Figure 3.5 (b), (c) elaborate that the domain boundaries from the first to second self-assembled layer observed in the large-area structures are formed by NTCDI noncovalent dimerization (via two N-H⋯O=C hydrogen bonds). The length of NTCDI dimer (L_2) is 2.2 ± 0.05 nm, which is just the twice value of a single NTCDI molecule (L_1 = 1.04 ± 0.05 nm, in Figure 3.5 (a)). Note that these domain boundaries were also observed without an accompanying second layer, but never appeared in 20% methanol solutions. This point towards NTCDI-pairing being a first-layer phenomenon which can be

weakened with increased solution polarity. Meanwhile a second layer can fully overlap one or two crystalline domains to the sides of the boundary. The formation of the crystalline domain can be monitored at the HOPG/network peripheries. Interestingly, the bilayer was found to grow directly from bilayer domain peripheries with a single rate constant and no preferred hexagonal symmetry direction on the pristine surface.

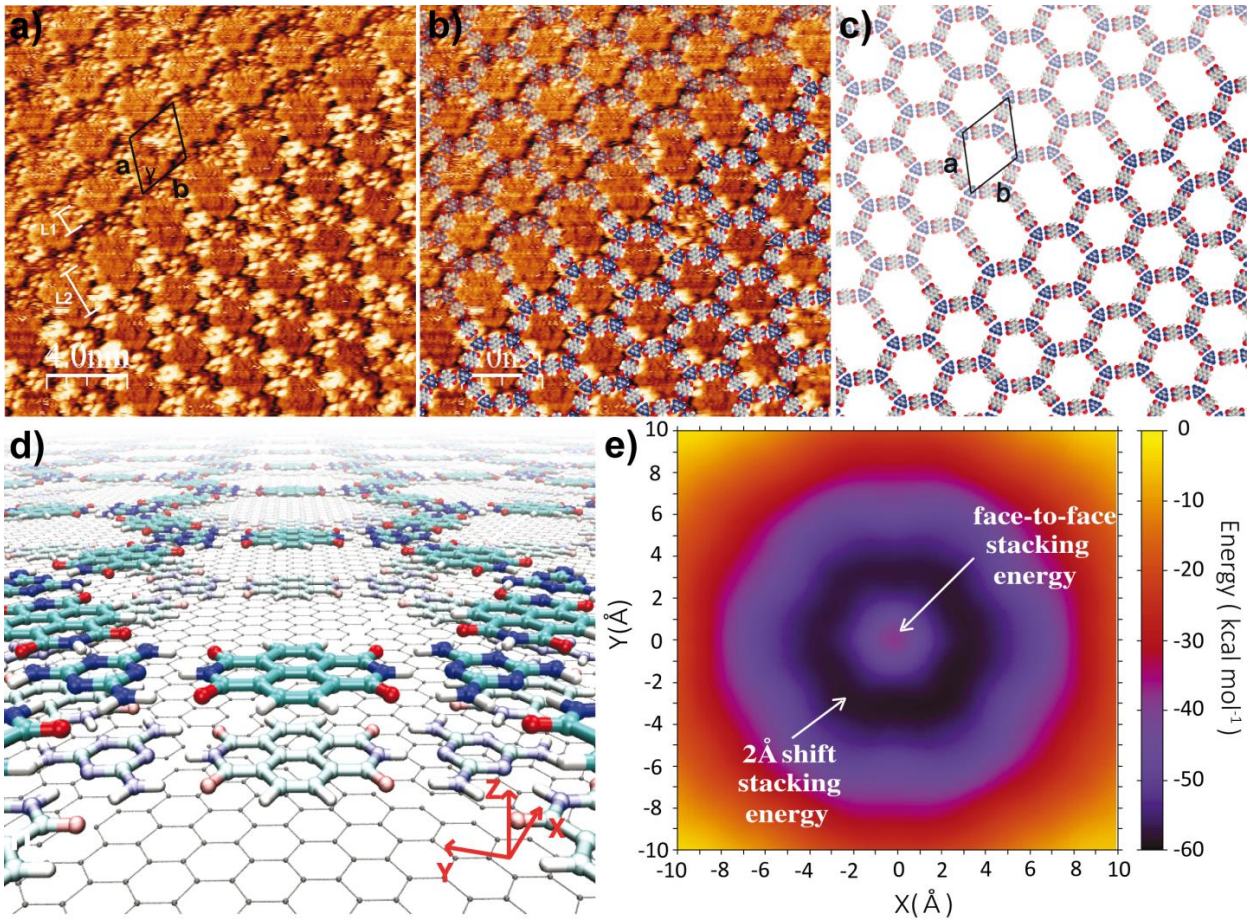

Figure 3.5 (a) STM image with enhanced molecular resolution of the domain boundary. Tunneling parameters of STM image at the solid-liquid interface: I_t = 20 pA, V_t = 300 mV. The concentration ratio of melamine and NTCDI is 2 µM : 5 µM using TCB solutions with low DMSO content. Unit cell: a = 2.8 ± 0.1 nm, b = 2.8 ± 0.1 nm, γ = 59 ± 2°. (b) STM image shown in (a) with the corresponding superimposed molecular models. (c) Bilayer molecular models reveal that the domain boundary formation is exclusively due to pairing of NTCDIs via two hydrogen bonds in the first layer. (d) Perspective molecular rendering of face-to-face (X,Y = 0,0

in (e)) vdW stacking of two melamine-NTCDI dimers. (e) MMFF molecular mechanics energy map of the X,Y translation of a melamine-NTCDI second-layer atop of a monolayer.

Concerning the vdW 2D-to-3D stacking configuration, it is obvious that the pattern of the second layer is as same as the first layer. And the experimental unit cell parameters of the second layer are a = 2.8 ± 0.1 nm, b = 2.8 ± 0.1 nm, which are identical with previously published values[179, 181]. The full overlap (face-to-face) of the second layer on top of the first layer is due to the formation of a domain boundary between first layers as previously discussed. In fact, when a continuous first layer without a domain boundary and featuring a shifted second layer is hypothesized, the STM data does not match plausible pattern models (Figure 3.6). We suggest here that strong H-bonding of the carbonyl moieties with melamine decreases the local electrostatic potential, thereby reducing Coulomb repulsion and allowing eclipsed face-to-face vdW stacking of supramolecular networks, now constituting prototype 3D structures. To give evidence of this, the energy dependence of vdW stacking between one melamine-NTCDI dimer on top of another with the MMFF force field is investigated. After the geometrical minimization of the top dimer fully eclipsing the bottom dimer (Figure 3.5 (d)), the top dimer is translated in X,Y to generate the energy map depicted in Figure 3.5 (e). The most favorable stacking energy during translation is found at a semicircle of ~ 2 Å around the face-to-face stacking position in Figure 3.5 (d). As we expected, this shift is an order of magnitude lower than the one found for the case of shifted vdW adlayers, arising from electrostatic repulsion calculated with the same MMFF force field[20].

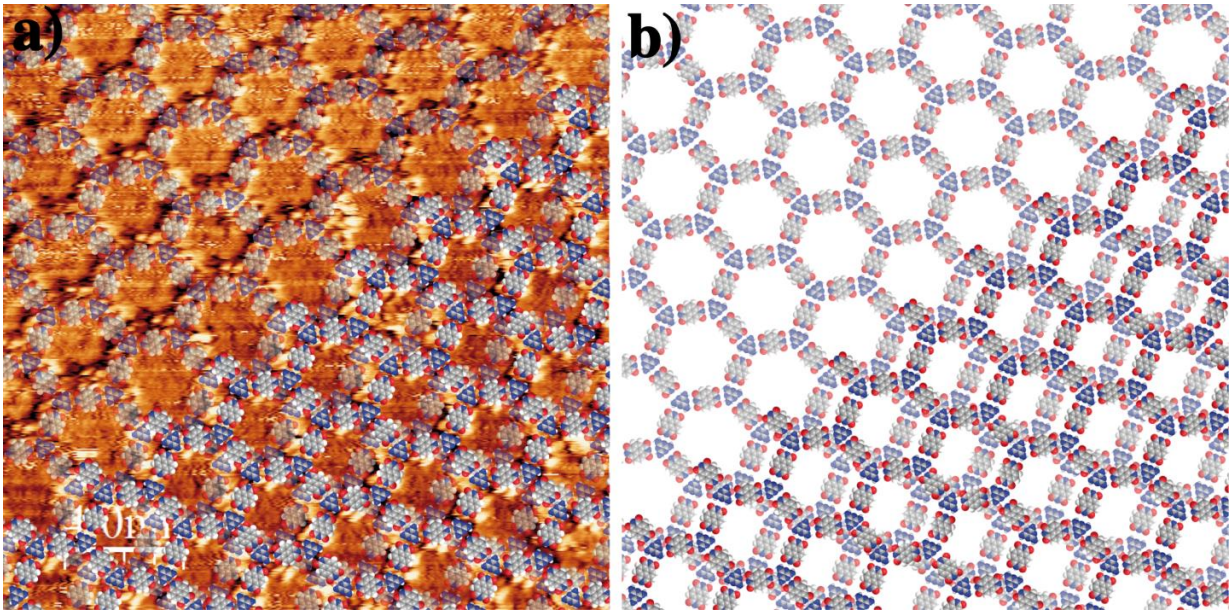

Figure 3.6 Alternative stacking of bilayer molecular models when assuming no NTCDI-pairing domain boundary in the first layer, but rather a continuous first layer and a shifted second layer. It is clear that a continuous first layer with a shifted second layer strongly mismatches the STM image (i.e. NTCDI from the first and NTCDI from the second layer would be clearly observed in the pores of the second layer domain).[23]

Altogether, supramolecular 2D and 2D-to-3D growth with large crystalline domains are developed best in the presence of a polar solvent like methanol (Figure 3.2 (a)) where only the strongest triple hydrogen bond are favored. The interactions between molecules and solvent are weakened as decreasing solution polarity, thereby dispersion forces dominate, which maximize the contact surface between layers. As a result, the aligned vertical growth is induced spontaneously. In addition, a decreasing solution polarity also provokes NTCDI pairing "defect" domain boundaries, constituted by double hydrogen bond only. These boundaries are important topographical references to study the 2D-to-3D growth by STM.

3.2 The network of melamine and NTCDI at the solution-graphene/H-C(100) interface

After successful self-assembly of melamine and NTCDI at the solution-HOPG interface, it is necessary to realize these molecular structures on other novel platforms which can be used for optoelectronic device applications. With a system capable of forming three-dimensional reticular nanoporous networks, self-assembly on technologically relevant platforms can be tackled. We facilitate this task through thinking of the relation between HOPG and multilayer graphene, suggesting that assembly protocols on HOPG can be employed at graphene-decorated substrates. This argument has been verified[182-185] and is elaborated in Figure 3.7. Figure 3.7 (a) shows a typical high resolution STM image of single layer graphene on copper foil (G/Cu) by CVD-grown approach. In contrast to HOPG where every second (β-site) carbon atom is visible by the STM under large tip-sample distances,[186] in graphene, α and β-site atoms are all visible with equal intensity[187]. A few model hexagons are superimposed on the STM image to demonstrate the honeycomb lattice structure of graphene. The corresponding unit cell parameters are a = 2.39 ± 0.1 Å and b = 2.35 ± 0.1 Å, as previously reported in STM investigations.[145, 186, 188] Accordingly, Figure 3.7 (b) reveals that the melamine-NTCDI network forms a continuous and similar 2D porous network on the G/Cu surface, with a unit cell parameters of a = 2.7 ± 0.1 nm and b = 2.8 ± 0.1 nm. Importantly, we find that the melamine-NTCDI network extends seamlessly across the surface defects inherited from the underlying copper substrate (shown in Figure 3.7 (b)).

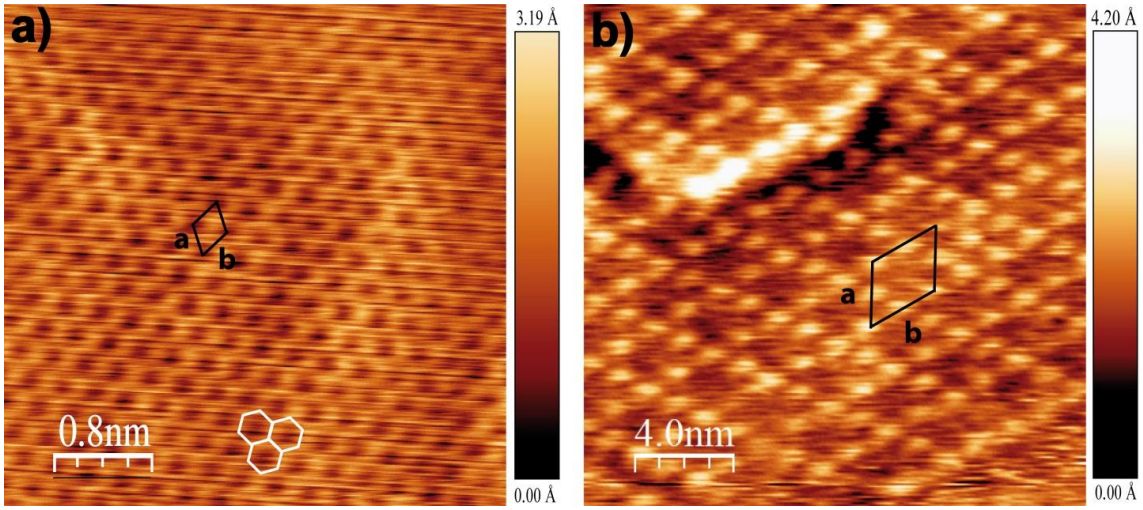

Figure 3.7 (a) High resolution STM image of CVD-grown graphene on copper foil with tunneling parameters of I_t = 80 pA, V_t = 20 mV. (b) Melamine-NTCDI network self-assembled on graphene/Cu with tunneling parameters of I_t = 30 pA, V_t = -50 mV. The ratio of melamine and NTCDI is 5 µM : 8 µM.[23]

Inspired by these findings, the supramolecular network formation can be explored on the graphene/H-C(100) diamond platform that is of technological importance[189-191], transparent, conductive[192] and atomically flat. Particularly, fabrication of these graphene-based devices will provide an impetus to the planar sp^2-sp^3 carbon-on-carbon technology.[163, 164] The approach to transfer a graphene sheet from original copper foil to hydrogenated diamond substrates (H-C(100)) is elaborated in section 2.1.5. The electronic properties of the hybrid system (G/H-C(100)) assessed by tunneling spectroscopy measurements are also explained in section 2.1.5. Despite these peculiar electronic features of the all-carbon hybrid platform, regular melamine-NTCDI networks are readily expressed on this platform, as shown by the exemplary STM data in Figure 3.8 (a). Some height differences in the contrast topography of each NTCDI molecule appear when the melamine-NTCDI network self-assembles onto the desired G/H-C(100) platform (cf. Figure 3.8 (a) inset). And the line profiles shown in Figure 3.8 (c) reveal the layer differences of 1 Å. We tentatively assign the bright spots to the single NTCDI molecules which are vdW-stacked on NTCDI molecules of a large area network layer below. Such aggregation tendency appears to oppose the 3D studies at HOPG surface, where the bilayer is reported to

grow as a single entity. However, also at the HOPG interface, when the molecular network fully covers the substrate, few-molecules with higher apparent heights can be individually observed to adsorb on top of the underlying network (Figure 3.2 (b)). In fact, such aggregation tendency makes extended networks on G/H-C(100) very difficult to image with high resolution by STM. Despite this drawback, nanoporous structures in the first and second layers can be still recognized from Figure 3.8 (a). The corresponding line profile depicted in Figure 3.8 (b) reveals apparent height differences between the bottom and top network with similar values obtained on HOPG: the height of the first layer is around 1.5 Å with respect to the pore holes shown with the green curve; the height of the second layer, depicted in blue color, amounts to 2.6 Å.

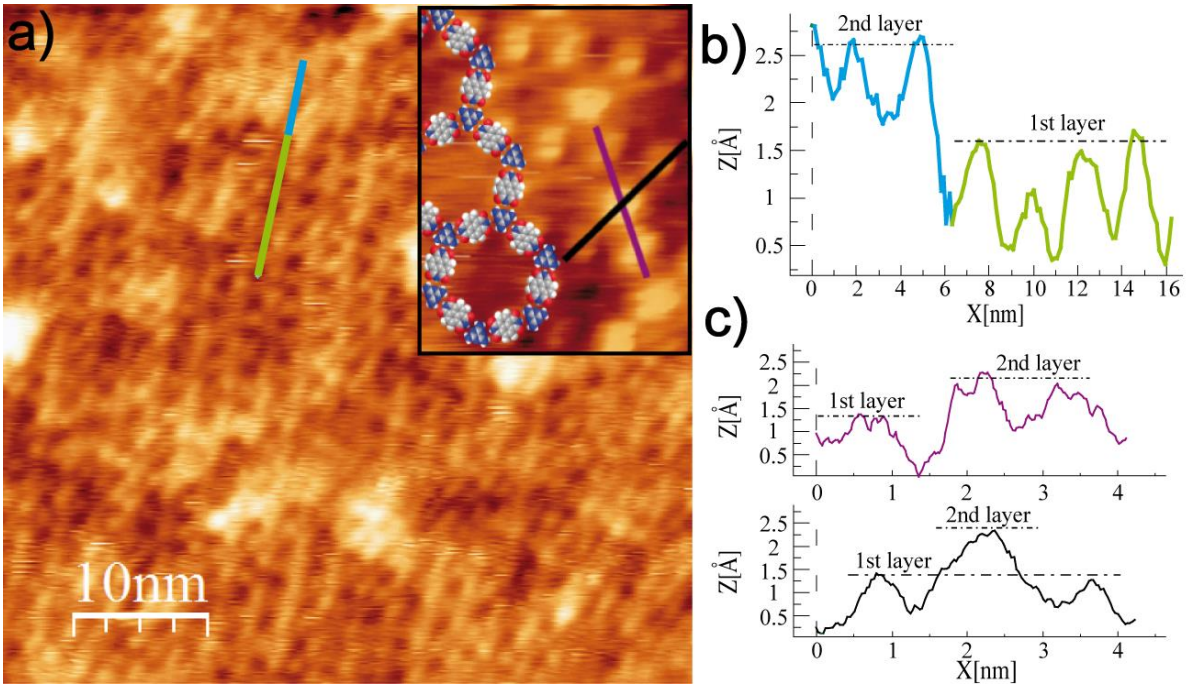

Figure 3.8 (a) STM image of bilayer melamine-NTCDI network assemblies at the solid-liquid interface on CVD-grown graphene/hydrogenated diamond surface (G/H-C(100)). Inset: a close-up STM image of network with molecular model exhibited the same pattern with those on HOPG and CVD-grown graphene/Cu. (b) Cross-sectional line profile showing different height of bilayer corresponding to the colored solid lines in (a). (c) Cross-sectional line profiles corresponding to the colored solid lines in the inset of (a) show single molecules in the second layer. Tunneling parameters: I_t = 20 pA, V_t = 200 mV. The ratios of melamine and NTCDI for both are 8 µM : 12 µM.[23]

Particularly, in this zoom-in image (Figure 3.9 (a)), even tetramers on top of the second layer, i.e. a third network layer with an apparent height of 3.5 Å, can be observed from the line profiles of Figure 3.9 (b). However, it is important to note that extended third layer crystalline networks were never identified. This phenomena is tentatively attributed to the low solution concentrations used, which are a requirement for avoiding phase separation[179]. Therefore, it is suggested that a dedicated self-assembled molecular instrumentation which controls self-assembly under macroscopic pressure, temperature, flow and stoichiometry, could provide the necessary exquisite physico-chemical control for multilayer formation or synthesis of macromolecular architectures. This work is published on *Nano Letters*.[23]

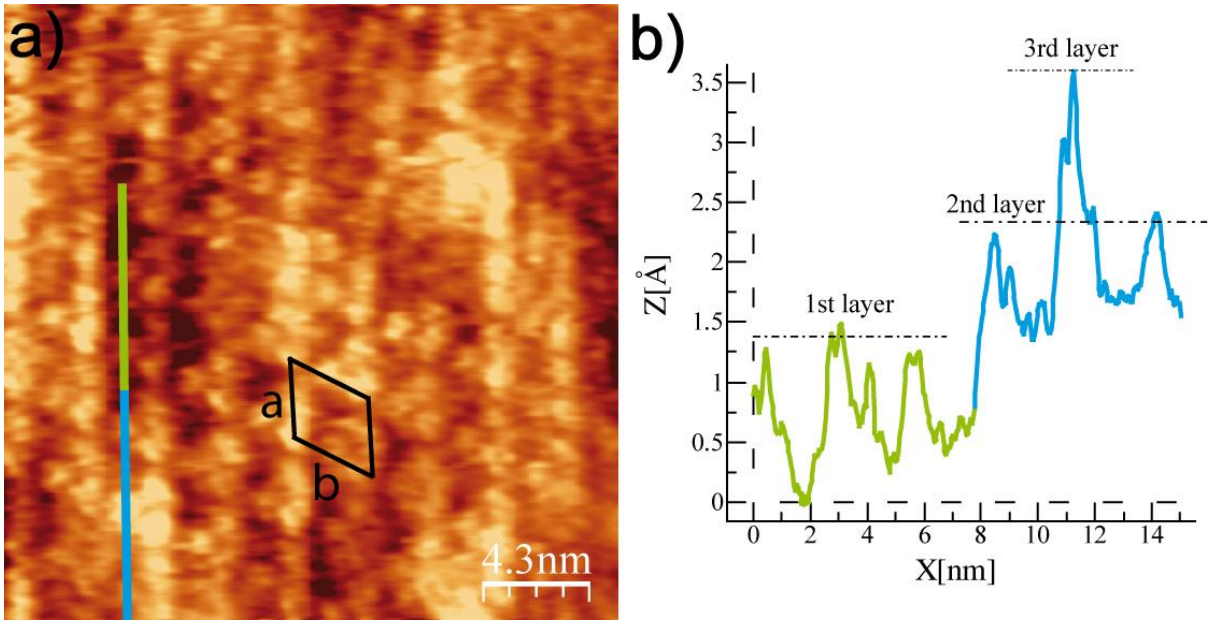

Figure 3.9 (a) STM image of multilayer melamine-NTCDI network assemblies on G/H-C(100) (without NTCDI-pairing domain boundaries). Tunneling parameters: I_t = 6 pA, V_t = -60 mV. Unit cell parameters are a = 2.7 ± 0.1 nm and b = 2.8 ± 0.1 nm. (b) Cross-sectional line profile corresponding to the colored solid lines (green: first layer; blue: multilayer) in (a). The ratio of melamine and NTCDI is 8 µM : 12 µM.

Chapter 4

Photoresponse of Melamine and TDI Self-assembled Networks

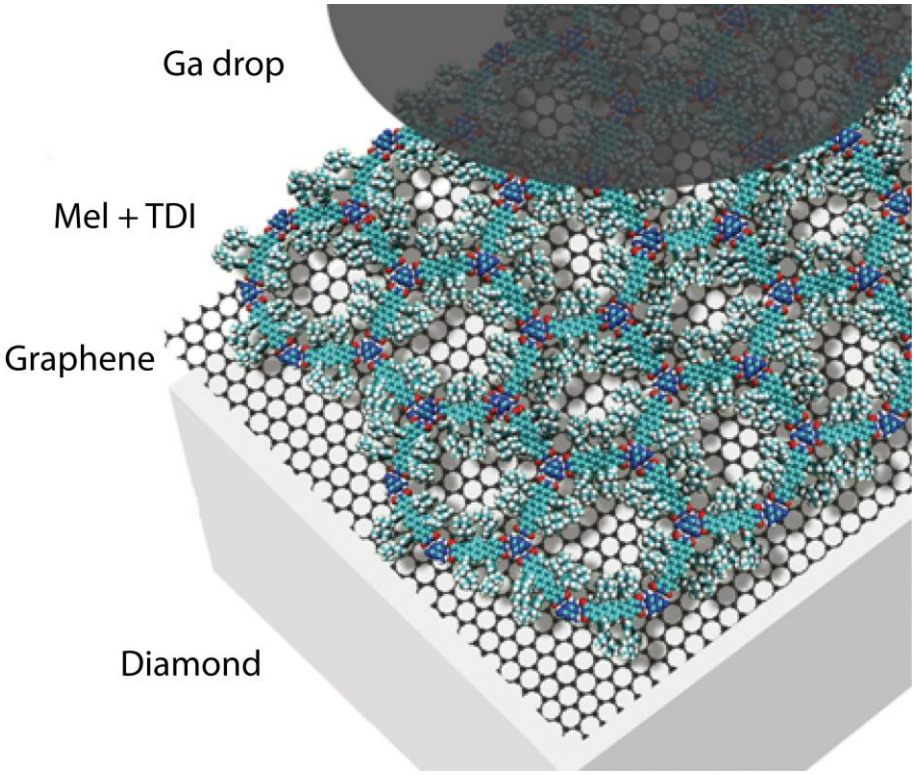

Figure 4.1 Schematic drawing of the photovoltaic device setup including the $[TDI_3Mel_1]_n$ supramolecular network.

Having verified the supramolecular network formation at the graphene/diamond interface, the larger conjugated molecules can be employed to investigate photophysical properties towards molecularly precise devices. Sensitizing interfaces with molecules was early recognized[193] as efficient means to photovoltaic charge generation. The strategy became technologically viable by optimizing the sensitizer surface area.[194] Thus, it is clear that in order to allow a transition to a second generation of device engineering exhibiting high spatio-temporal heteromolecular control, devices must be fabricated with large surface area and where the absolute location of different molecular components is mastered and precisely known *a priori*. So far, the elements of device approaching such molecular precision employ single molecule configurations[195, 196], which are not yet ready to be implemented for wide-spread technological applications. One strategy for large-area, artificial molecularly precise device fabrication is to grow molecular architectures via the bottom-up[15] technology at interfaces with solutions[197] or under vacuum. We have shown that supramolecular networks can template on a graphene-decorated, optically transparent, and atomically flat platform in an effort toward *in situ* optoelectronic molecularly precise device fabrication in Chapter 3. Here in this chapter we present the photovoltaic response of a similar bicomponent supramolecular network on transparent, graphene-decorated H-C(100) diamond (GHD) and applying a gallium droplet as a counter electrode. This time, the network is formed with a chromophore, consisting of a terrylene diimide derivative (TDI) and melamine (Mel). The scheme of the setup is shown in Figure 4.1. After initial molecular characterization by means of scanning tunneling microscope (STM), the generated photocurrents of 0.5 ± 0.2 nA and photovoltages of 270 ± 120 mV are obtained by scanning tunneling spectroscopy (STS) at 19 mW cm^{-2} irradiation intensities at 710 nm. The 0.6% incident photon to electron efficiencies (IPCE) at 710 nm is found when estimating the contact area *ex situ*, yielding photocurrent densities of 47 ± 5 µA cm^{-2}.

4.1 STM measurements

The successful formation of highly crystalline 2D supramolecular networks between melamine and TDI was investigated *ex situ* (on a model substrate) and *in situ* (in the device configuration) by means of STM under ambient conditions. Self-assembly experiments involved

applying a mixture solution of Mel : TDI in 1,2,4-trichlorobenzene (TCB) with 1 - 5% of dimethylsulfoxide (DMSO) solution, first on highly ordered pyrolytic graphite (HOPG) surface and then on a transparent platform made by CVD-grown graphene transferred to hydrogenated H-C(100) diamond (GHD). The large area of ordered network is shown in Figure 4.2 (a) and the hexagonal structures formed by triple hydrogen bonds of the zoom-in image are clearly observed in Figure 4.2 (b). The 2D Fast Fourier transform in Figure 4.2 (a) shows the high crystallinity achieved by the samples on HOPG. The hexagonal structures normally appear after a few minutes of approaching the tip to the surface at the solid-liquid interface. In the STM images, Mel molecules appear darker than the TDI chromophores due to their lower density of states[198]. Figure 4.2 (c), (d) show how the observed hexagonal structures correspond to the expected chemical models. The chemical models have been minimized with the MMFF molecular force field, the hexagonal size corresponding to the theoretical unit cell is a = b = 4.23 nm and the pore diameter is d = 4.6 nm.

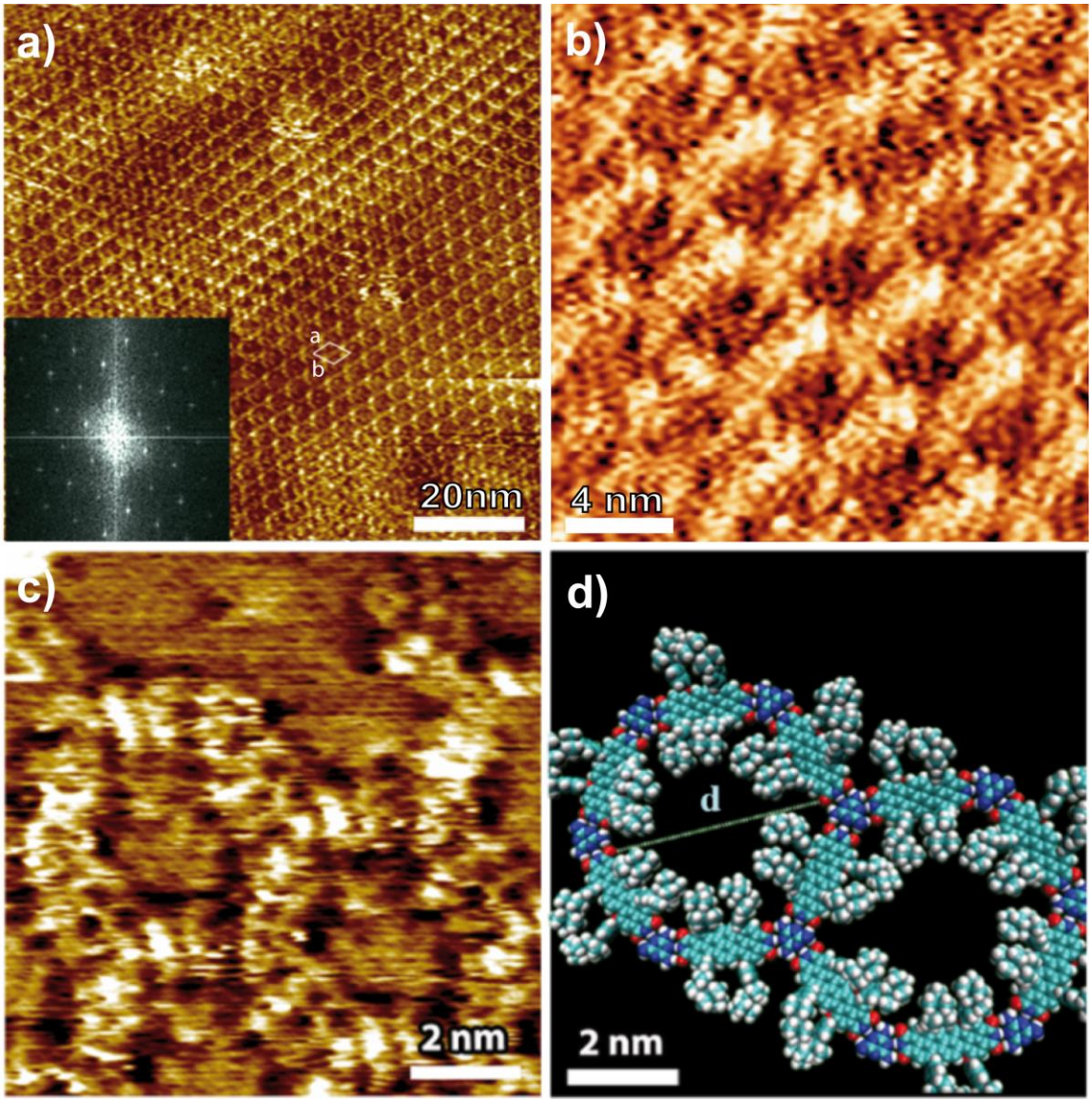

Figure 4.2 STM images showing the assembly of Mel : TDI on HOPG substrate. (a) STM large area constant current image (8 µM : 12 µM). Inset: 2D Fast Fourier transform showing the high crystallinity of the assembly on HOPG. Unit cell a = 4.1 ± 0.2 nm, b = 4.3 ± 0.2 nm and (a,b)= 65 ± 2°. (b) Zoom-in image (8 µM : 12 µM) of porous network with a pore size of 4.6 ± 0.1 nm. (c) STM constant current image of Mel : TDI (10 µM : 16 µM) and underlying HOPG interface. (d) Molecular model minimized by the MMFF force field, the hexagonal size corresponding to the theoretical unit cell is a = b = 4.23 nm and the pore diameter is d = 4.6 nm. Tunneling parameters: I_t = 20 pA, V_t = 300 mV.

After transferring graphene on hydrogenated diamond, the GHD surface seems flat for molecular self-assembles in the large area. Figure 4.3 shows the contrast 500 × 500 nm topographies of H-C(100) surface and GHD surface.

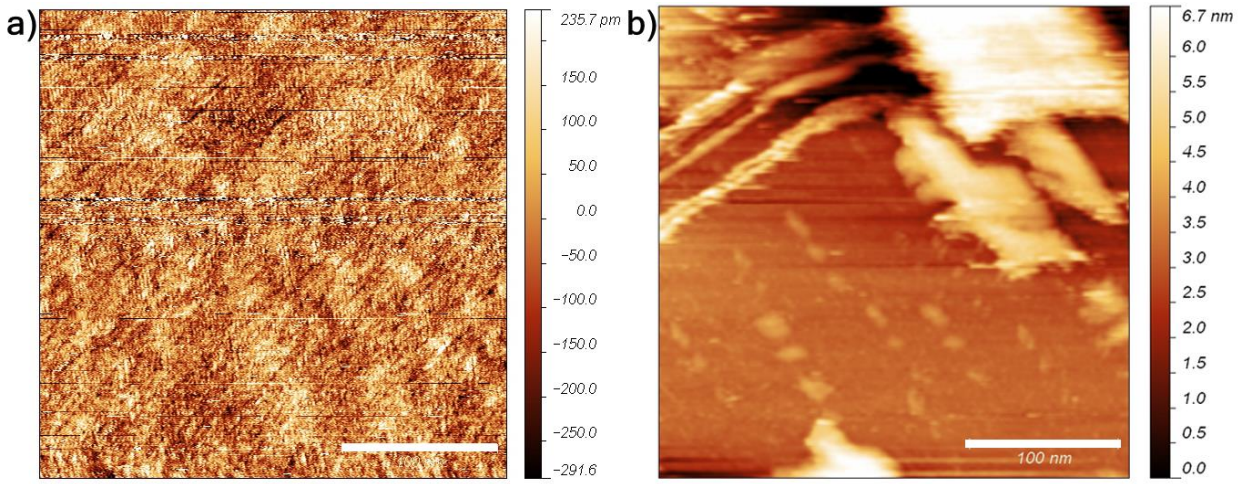

Figure 4.3 Large area STM topography of atomically flat H-C(100) diamond surface (a) before and (b) after CVD graphene transfer. Scale bar 100 nm.[2]

At GHD only nanocrystalline hexagonal domains with sizes of tens of nanometers are monitored (Figure 4.4). The higher roughness of GHD prevents the growth of a highly regular bicomponent network. Especially, defects and impurities on GHD make the extended growth of crystalline bicomponent networks challenging, as discussed below. The experimental unit cell parameters for the network formation on GHD substrate amount to a = 3.9 ± 0.2 nm and b = 4.0 ± 0.2 nm and (a,b) = 62 ± 1°, which are in good agreement with the values observed on HOPG.

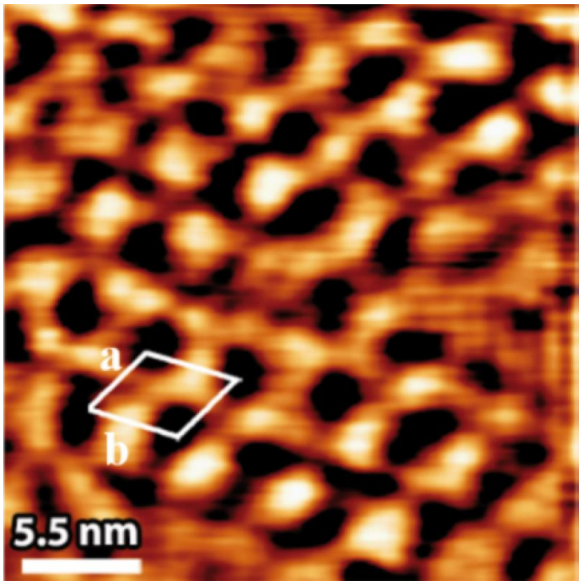

Figure 4.4 Gaussian-filtered STM constant current image of Mel : TDI (8 µM : 12 µM) on GHD. Unit cell a = 3.9 ± 0.2 nm and b = 4.0 ± 0.2 nm and (a,b) = 62 ± 2°. Area: 13.8 nm^2. Tunneling parameters: I_t = 20 pA, V_t = 300 mV.

4.2 UV-visible measurements

UV-visible measurements were performed with a UV/VIS/NIR spectrometer, *Lambda 900* (*Perkin Elmer*). The spectra were recorded at the full spectra range from 200 nm to 2000 nm with a data interval of 5 nm, and integration time of 0.32 s and 0.68 s for UV/VIS and NIR respectively. For absorption measurements, we drop-casted 5 ± 1 µL solution of Mel : TDI (8 µM : 12 µM) in 1,2,4-Trichlorobenzene (TCB, *Sigma-Aldrich*, 99.9%) on GHD and left it dry overnight in the air. The spectrum was averaged 10 times and plotted versus the wavelength for each sample. To study the concentration dependency of the self-assembled network, 5 ± 1 µL solutions of Mel : TDI (8 µM : 12 µM) in TCB are drop-casted onto the dried network surface sequentially.

With an atomically flat and transparent platform such as GHD, capable of supporting the bimolecular 2D self-assembly, it is interesting to investigate the optical spectral properties of

crystalline supramolecular layers. Thus, UV-visible absorption measurements are employed to distinguish between changes in the TDI spectrum upon hydrogen bond recognition with melamine.

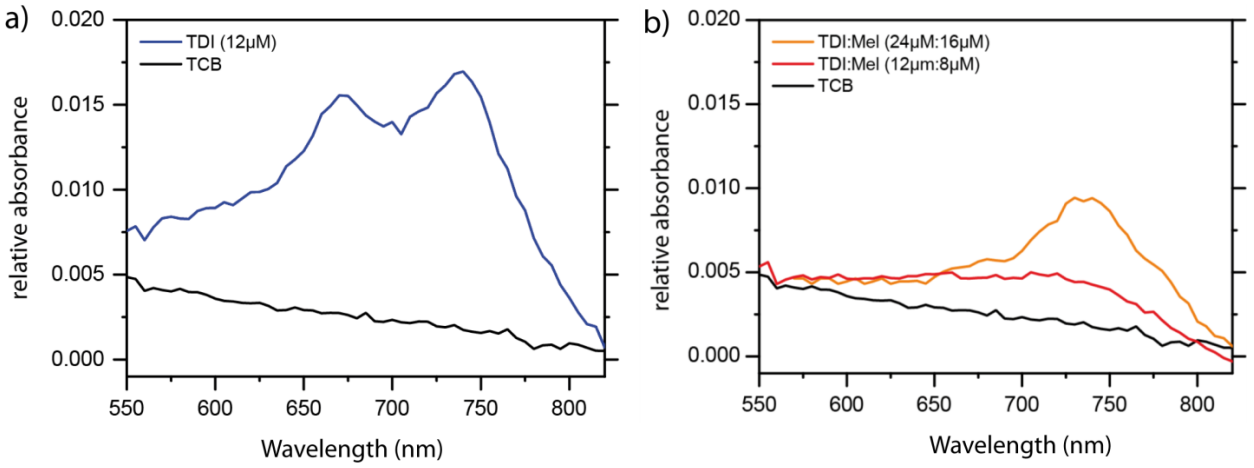

Figure 4.5 UV-visible spectra on graphene-decorated H-C(100) diamond. (a) TDI (12 μM) and pure TCB baseline spectra. (b) Mel : TDI (8μM : 12μM) and pure TCB baseline absorbance spectra. Mel : TDI (16 μM : 24 μM) is also shown as additional evidence of strong absorbance reduction upon complexation with melamine.

The absorption spectra of 5 ± 1 μL pristine TDI (12 μM) in a TCB solution and the pure TCB solvent as the reference on the graphene-decorated diamond surface are shown in Figure 4.5 (a). Two distinct absorption peaks at 665 nm and 730 nm can be distinguished. This corresponds to a bathochromic shift of 46 and 61 nm with respect to UV-visible measurements in solution (Figure 4.6). Note that the drop-casted TCB solvent as a reference shows no absorption in that wavelength range. The TDI absorption peak-to-baseline signal of 0.012 at 730 nm (cf. Figure 4.6 for absolute absorption units) is indicative of approximately a monolayer of TDI when compared to the absorbance of perylene tetracarboxylic anhydride (PDA) monolayer on graphene[199], with the value around 0.007 at 702 nm. The molar attenuation coefficient of PDAs and PDIs[200] with a value of ~ 5×10^4 M^{-1} cm^{-1} is half the one of analogue TDI derivatives[201] ~ 1×10^5 M^{-1} cm^{-1} at the respective absorbance maxima. When applying 5 ± 1 μL solutions of Mel and TDI with a concentration ratio of 8 μM : 12 μM onto the GHD, it can be observed a fivefold reduction of the

TDI signal along with a bathochromic shift of the absorbance maxium to 740 nm (Figure 4.5 (b)). We expect a 1.5-fold reduction of the absorbance at least when comparing the molecular density of TDI molecules (0.31 nm^{-1}) with that of TDI molecules in the Mel + TDI network (0.21 nm^{-1}). Incidentally, a fourfold reduction of the absorbance maximum is also prominent in π-stacks of perylenes[202] partly due to the specific surface reduction.[203, 204] Considerring the reduction of the absorbance is not an effect of variations in the dropcastted solution volume or concentration (see Figure 4.6), we can suggest that it is the combined effect of a looser packing (increased unit cell) of Mel + TDI network and its aforementioned π-stacking[23].

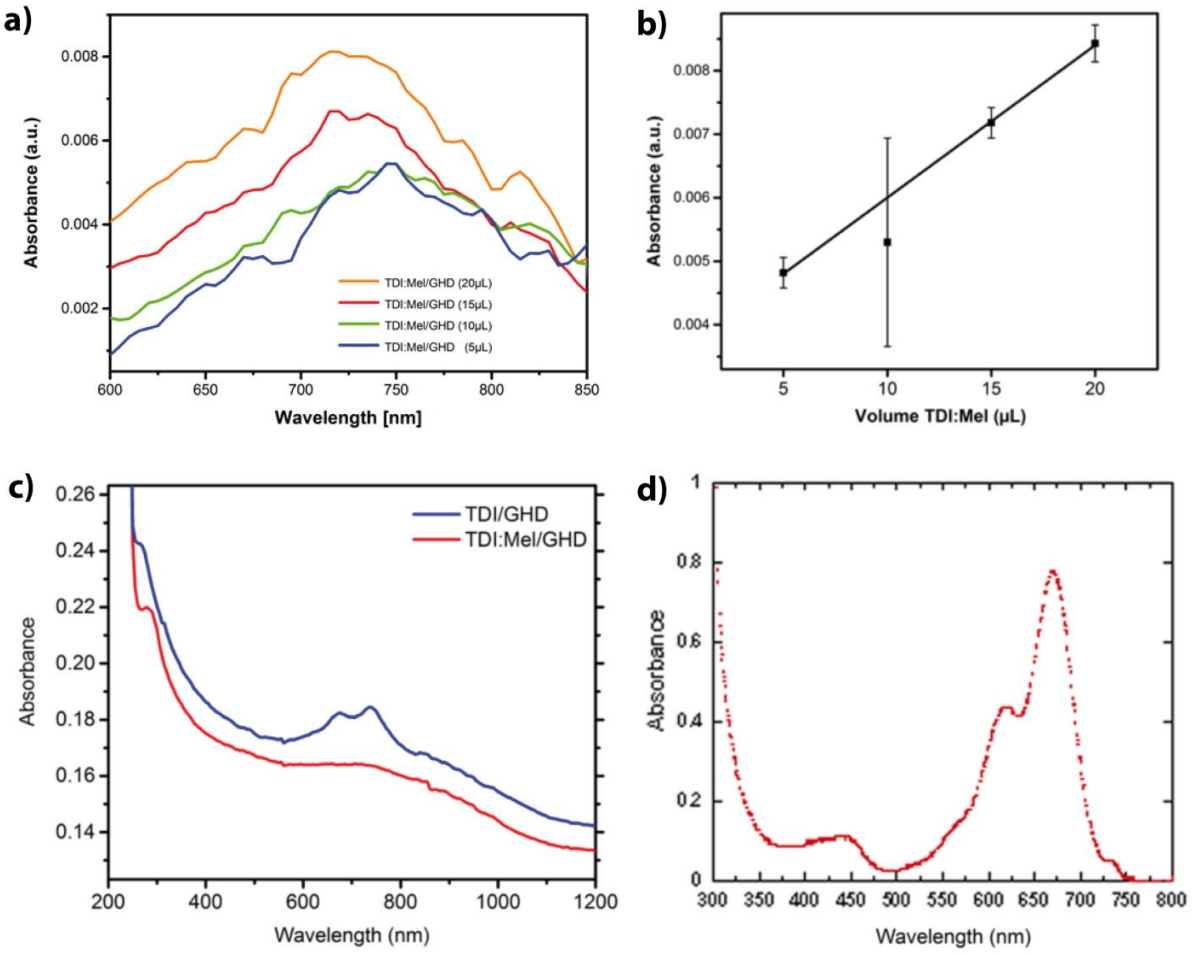

Figure 4.6 UV-visible measurements. (a) UV-Vis spectroscopy of drop-casted volume of Mel : TDI (16 µM : 24 µM) on GHD for 5 µL, 10 µL, 15 µL and 20 µL. (b) Absorbance value at 710 nm with error bars (10 averages of spectra) as a function of on the volume dropped onto the

surface. UV-Vis measurements were performed by stepwise adding 5 ± 1 µL of Mel : TDI (16 µM : 24 µM) and letting the films dry. A linear increase in absorbance at 740 nm was detected, but even after five dropcasted equivalents did not reach 0.01 absorbance units (the peak-to-baseline absorbance of 5 ± 1 µL of 12 µM pristine TDI). (c) Absolute absorbance of Mel : TDI (8 µM : 12 µM) and TDI (12 µM). Note that the overall higher absolute adsorption of TDI vs. Mel : TDI observed in over several freshly prepared samples can be potentially assigned to a decrease in the reflectivity of the atomically flat diamond crystal with Mel : TDI and does not necessarily signifies a lower absolute absorption of the GHD substrate with the Mel : TDI active layer. (d) UV-Vis measurement of TDI in quartz cuvettes in 1% DMSO in TCB solutions.

4.3 STS measurements

4.3.1 Gallium (Ga) droplet measurements

In this section, the fluorescence measurement of the gallium (Ga) droplet contact area and the current characteristics of the junction after automatic Ga droplet approach are illustrated and discussed below. A Ga droplet was prepared as employed for the photocurrent measurements of the photovoltaic device. In order to preserve pristine molecular interfaces aiming at molecular precision, the Ga dropplet was employed to soft-contact the supramolecular network on GHD substrate. The top contact was fabricated by dipping a blunt tungsten tip into a liquid gallium droplet and slowly cool down at room temperature as shown in Figure 4.7 (a). Gallium alloys have been widely applied as a replacement for mercury to create the macroscopic device contacts with molecular layers[205, 206]. Our strategy consists on approaching the gallium-coated tungsten tip to the GHD substrate with a monolayer network and stabilizing the tip to a current setpoint of 2 nA at 100 mV, with the help of a modified STM under ambient conditions. Figure 4.7 (b) shows the Ga electrode in contact with the sample prior to the tunneling spectroscopy measurements.

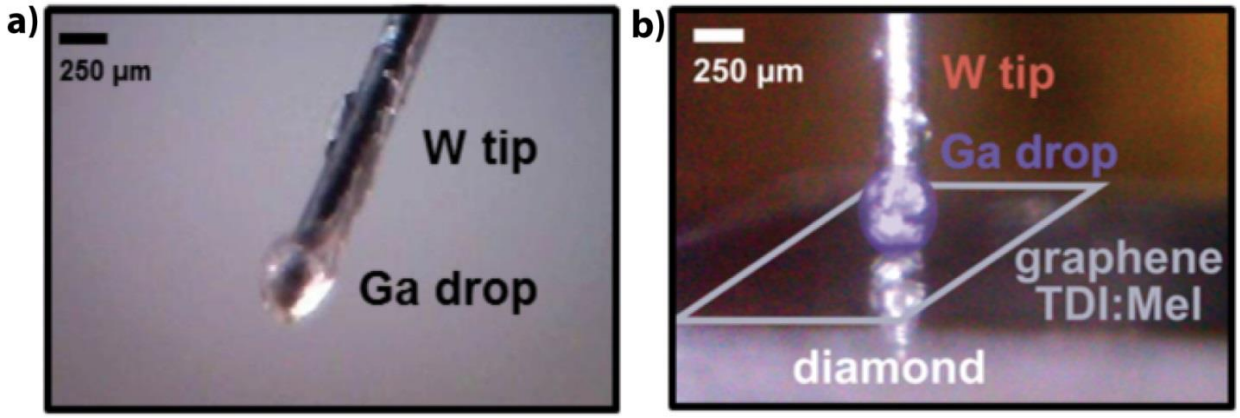

Figure 4.7 (a) Tungsten STM tip with a gallium droplet. (b) Gallium electrode in contact with the sample prior to the tunneling spectroscopy measurements.

We can infer the contact and wetting of Ga on the GHD substrate by fluorescence spectroscopy and current measurement during approaching the electrode to the surface. The Ga droplet is approached to a thin film of fluorescent dye on HOPG surface with the same tunneling contact approach and current parameters used in the STM measurement. A contact junction forms by employing a nm-thin film of an insulating dye, Rhodamin B (Radiant Dyes, *Wermelskirchen*), that implies physical contact with the monolayer. The physical contact of the Ga droplet with the Rhodamin B film leads to a higher deformation of the droplet and thus increases the contact area in comparison to the area of photoresponse measurement. Therefore, this method accurately estimates an upper bound to the tunneling contact area and a minimum current density and efficiency. In order to form the nm-thin film, we spin-coated the HOPG substrate with a rate of 480 rpm for three times with 10 µL saturated solution of Rhodamin B in acetone, and made it dry between each application. Then we retracted the tip from the surface and fixed it to a microscope slide and imaged under fluorescence conditions with a fluorescence microscope (*Leica DMI 3000B, Wetzlar*). The images of the tip obtained from the fluorescence measurement are shown in Figure 4.8 with an enhanced contrast to make the contour of the tip visible (darker area). The pixel numbers of brightness higher than a certain threshold was extracted accordingly from the raw data in grayscale. The total area corresponding to the pixels was calculated from the length scale per pixel (known from calibration). The threshold was set to a clear gap between brighter

and darker pixels in the histogram and the corresponding area in the image (Figure 4.8 (b)) was identified.

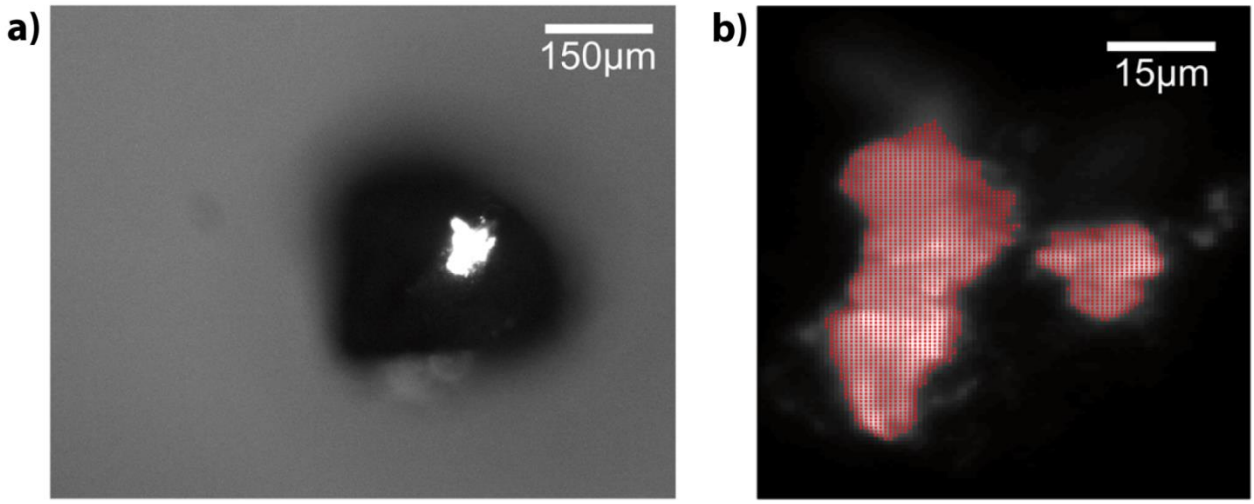

Figure 4.8 *Ex situ* fluorescence measurements estimating the tunneling contact area of the Ga droplet on a the Mel : TDI assemblies.[2] A film of Rhodamine B was spin coated on HOPG surface, brought into tunneling contact with the Ga dropplet electrode and the fluorescence image was recorded. (a) Fluorescence image of the tip with enhanced contrast. (b) Threshold image used to determine the contact area (red).

IV measurements are employed to characterize the photoresponse of the device elements and these measurements are performed with a home-built STM. A blunt tungsten tip surrounded by a heated gallium droplet was directly mounted into the tip holder of the scanner's piezo. The spectroscopy data were recorded with a forward sweep rate of 200 mV s^{-1} by using a Femto preamplifier. The current characteristics of the junction during the Ga electrode approaches to the surface are shown in different cased as Figure 4.9.

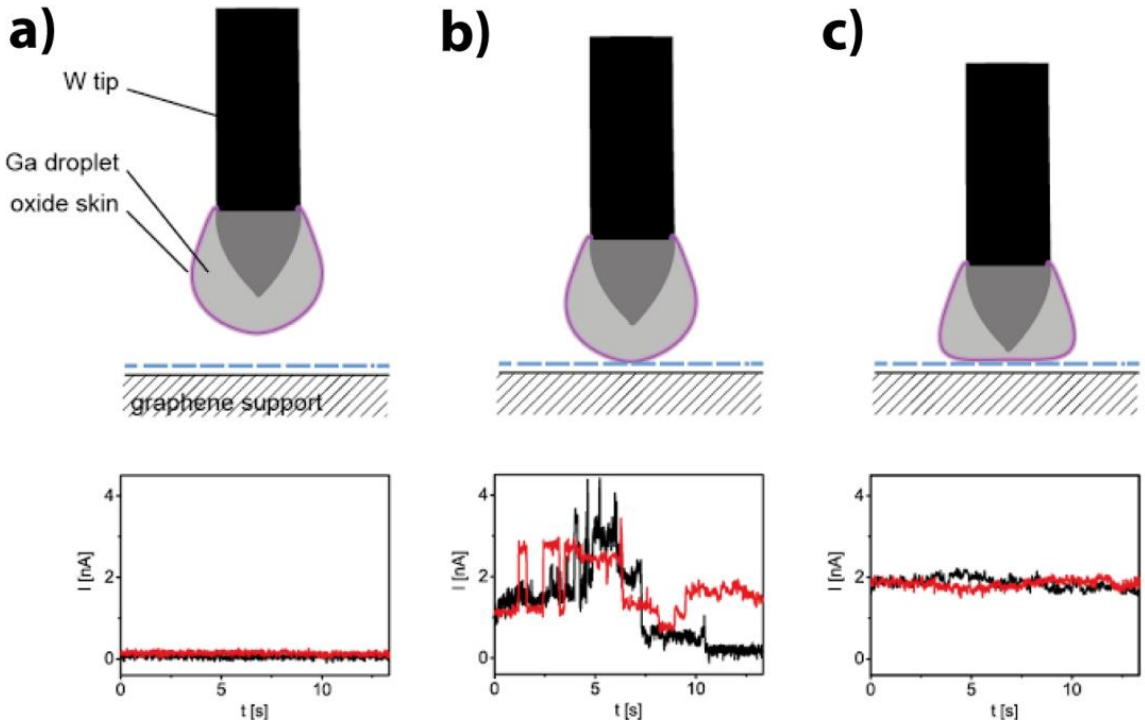

Figure 4.9 Current characteristics of the junction after automatic Ga droplet approach. (a) Current far away from the substrate. (b) Instable junction - the intermittent contact points to a small contact area; no wetting takes place. (c) Stable junction (contact regime). Setpoint: 2 nA, sample voltage: 100 mV, approach velocity: 8 nm s^{-1}.

4.3.2 Photoresponse measurements

The large-area *IV* measurements were performed on the Mel : TDI /GHD and bare GHD substrates respectively. The *IV* spectra of GHD (Figure 4.10 (a), black line) and Mel : TDI on GHD (Figure 4.10 (a), red line) were recorded with a forward sweep of 200 mV s^{-1}. The current was recorded to obtain the photoresponse characteristics under dark and illumination conditions with a red LED (λ = 710 nm) of a measured power of 19 mW cm^{-2} and a green LED (λ = 520 nm) of a power of 13 mW cm^{-2}. The spectroscopy curves obtained for GHD in dark and under illumination of 710 nm red LED are shown in Figure 4.10 (a). There is no photoresponse observed when only the bare GHD is employed. Conversely, the illuminated *IV* curve of the

TDI/GHD monolayer photoresponse exhibits characteristic features. As expected, a finite current flows at zero bias voltage under illumination, which is named short-circuit current I_{SC} (SCC). An average SCC of I_{SC} = 0.5 ± 0.2 nA and open-circuit voltage (OCV) of V_{oc} = 270 ± 120 mV are measured by illuminating the system with monochromatic light of 710 nm red LED. Typical maximum and minimum values of the current obtained from the average photoresponse characteristic are also shown as shaded areas in Figure 4.10 (a). Futhermore, *IV* curves are recorded by illuminating the Mel : TDI network on graphene-decorated diamond with monochromatic light of 520 nm green LED, where TDI does not absorb light (Figure 4.10 (a), inset). Indeed, no photocurrent is generated under 520 nm green LED irradiation conditions where TDI does not absorb. The stability of the photovoltage generated by the junctions as a function of light on-off cycles is depicted in Figure 4.10 (b). Notably, for recording these on-off cycle photovoltages, EGaIn electrodes coated with alkyl thiols were employed for increased stability. The blunt tungsten tip was dipped into EGaIn (*495425, Sigma-Aldrich*) until obtained a smooth coating and subsequently transferred the tip into a pure solution of 1-dodecanethiol (*471364, Sigma-Aldrich*) for 15 minutes. These *IV* measurements with EGaIn tip were independently performed in an *Agilent Technologies 5100* STM using a logarithmic current amplifier to avoid current saturation. Prior to each single tunneling spectroscopy measurement, the feedback vertical position of the electrode was regulated again to a tunneling current of 1 nA and a voltage of 300 mV and turned off. The data were recorded with a forward sweep rate of 20 mV s^{-1}. The photovoltaic detection limit of this modified setup is 90 mV that calculated as trice the standard deviation of the dark voltage. The acquired data in Figure 4.10 (a), (b) correspond to stable contact junctions (no observable oscillations in the junction z-piezo nor identifiable non-contact tunneling junction formation) among tenths of different area surveys on four different GHD samples. In particular, a different regime is observed in some junctions, where a clear increase in the current with 710 nm red LED irradiation occurs but no OCV nor SSC are found (Figure 4.10 (c)). Current-distance (*IZ*) spectroscopy reveals an apparent exponential dependence of the current with the distance, which means these junctions do not physically contact (wet) the substrate. Hence, this non-contant regime is attributed to a photoexcitation effect, where additional tunneling channels are opened in the molecule's photoexcited state. Altogether, the supramolecular network based on TDI and Mel molecules specifically generates a photoresponse at the designated wavelength. It is worth approximating the tunneling contact area of the Ga

droplet with a diameter value of ~ 250 µm in order to compute equivalent photovoltaic efficiencies. Through the *ex situ* contact junctions with insulating fluorescence dyes (see Figure 4.8), we can estimate an area of $(9.9 \pm 0.6) \times 10^2$ µm^2 with respect to the *in situ* experiment. This area is roughly 2% of the projected area under the Ga electrode (49×10^3 µm^2, using a radius of 125 µm). From the *IV* spectra, the current densities of 10^{-4} A cm^{-2} at 0.5 V can be estimated. These current densities are comparable to those reported devices by contacting -S-$C_{16}H_{33}$ self-assembled monolayers/metal interfaces of similar contact areas[206], indicating a soft-contact. Moreover, a monochromatic IPCE of 0.6 ± 0.25% can be estimated at 710 nm, 19 mW cm^{-2} irradiation intensites according to the values from the derived photocurrent density of J_{SC} = (47 ± 5) µA cm^{-2} and the absorptivity of the network (Figure 4.5 (b)).

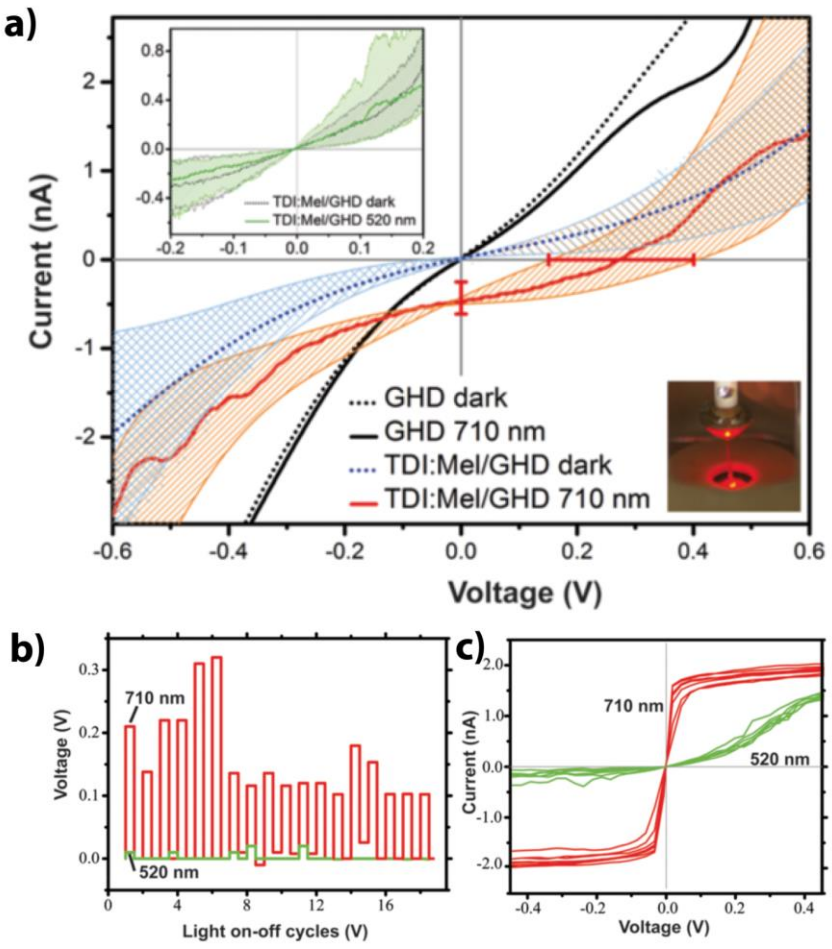

Figure 4.10 Photoresponse measurements of a supramolecular network optoelectronic device element. (a) *IV* characteristics of pristine GHD (black lines) and of Mel : TDI on GHD irradiated

at 710 nm (Inset: 520 nm photon irradiation). Approach parameters: I_t = 2 nA, V_t = 100 mV. Striped areas indicate the maximum and minimum currents observed. I_{SC} = 0.5 ± 0.2 nA, V_{oc} = 270 ± 100 mV. (b) Open circuit voltage for consecutive on-off irradiation cycles at 710 nm, followed by on-off cycles at 520 nm of Mel : TDI. Every set of six consecutive cycles is recorded with different junction (sample, electrode) preparations. The constant dark voltage background for each set is substracted (~ 0.05 V). For stability, these studies are performed with functionalized eutectic gallium-indium electrodes. (c) Scanning tunneling spectroscopy for consecutive on-off irradiation cycles at 710 nm, followed by 520 nm, showing drastic changes due to electron tunneling through photoexcited states. Setpoint parameters: I_t = 1 nA, V_t = 300 mV.

In summary, we have fabricated surface-confined bicomponent self-assemblies on GHD based on a functional TDI dye[83] absorbing at 740 nm. The active layer in the photovoltaic device ideally consists of a self-assembled terrylene diimide-based supramolecular nanoporous network exhibiting nanocrystalline hexagonal order. Because the shorter diimide-based molecules such as naphtalenes have been found to stack in the third dimension through van-der-Waals (vdW) face-to-face stacking[23], the employed system presents an avenue towards molecularly precise 3D devices. It was demonstrated how an atomically flat and transparent all-carbon GHD can serve as the photoanode and a Ga tip as top cathode electrode in optoelectronic applications. The photoresponse of our architecture exhibited a three order of magnitude increase in the SCC with a value of 0.5 ± 0.2 nA, with respect to the dark current and an OCV of 270 ± 120 mV. It is worth mentioning that average SCC and OCV for the single component TDI are measured as 0.09 ± 0.01 nA and 160 ± 60 mV, respectively. The reported OCV values are close to the electrode work function difference, being 4.5 eV[207] for graphene and 4.3 eV[208] for gallium. Such OCV correlation with the previous work function level alignment might be coincidental, as the origins of the OCV in excitonic solar cells are under intense discussion[209]. In our photovoltaic setup, a fully covered (supra)molecular monolayer was guaranteed by employing concentrations and volumes, which is equivalent to 3.8×10^{13} TDI molecules per substrate (and similar amount for melamine molecule). A monolayer was inferred to form with 5.4×10^{12} TDI molecules, considering a substrate area of 5×5 mm^2 and three TDI molecules per Mel + TDI unit cell area of 13.8 nm^2. Moreover, the peak UV-visible absorbance of 0.012 at 735 nm for pure TDI

molecules provides additional evidence of a molecular monolayer. Finally, once melamine and TDI supramolecular network formed on GHD, absorbance is greatly reduced as expected because of a lower molecular surface density generated by the assembly of a porous architecture. Formation of π-aggregates[202, 203], reducing the surface available for absorption, and hydrogen bonding[210], where charge transfer is likely to occur[211], contribute to the decrease in the absorbance.

Based on our estimation on the tunneling contact area, we can elaborate on the technological implications of photovoltaics of surface assemblies. In previous reports, the optimized thin film photovoltaic device of precursor molecule **3** blended with an organic acceptor[212] featured an IPCE[25] of 0.3% at 700 nm. The thin film was prepared by spin-coating the solution of 13mg ml^{-1}. The comparable estimation of an IPCE with a value of 0.6 ± 0.25% at 710 nm for our devices prepared by drop-casting a 5 μL solution with 1000 times more diluted (0.015 mg ml^{-1} ≈ 12 μM) suggests that the photoresponse generated from few monolayers of self-assembled (supra)molecular architectures may outperform the response from bulk spin-coated materials. This can be explained, in part, due to the higher internal quantum yields and collection efficiencies of monolayers, as reported for C_{60}-porphyrin mixed self-assembled dyes[213], natural photosystem-I[196, 214] and naturally occurring 2D crystals[215, 216]. Regarding possible charge collection mechanisms, there are two molecular interfaces in our designed configuration, one formed between molecular network and GHD while another formed between molecular network and gallium oxide out of the Ga tip. The oxide[217] tunneling barrier between the molecular network and gallium forms a blocking-layer which prevents the efficient collection of photogenerated electrons at the gallium electrode. In this regard, we suggest that the resulting photoresponsive device element is hole-only, i.e. photogenerated holes are easily collected at the graphene photoanode, while the corresponding electrons have to tunnel to the gallium counter electrode. Thus, it is expected that the efficiency of monolayer-thin optoelectronic devices will be radically improved through tuning of the work function and appropriate tunneling junction material (e.g. allowing hole-only and electron-only transport in the pertinent contacts)[218]. This work is a joint collaboration with S. Wieghold and published on *Nature Communications*.[2]

Chapter 5

Photoswitchable 2D Crystal Platform

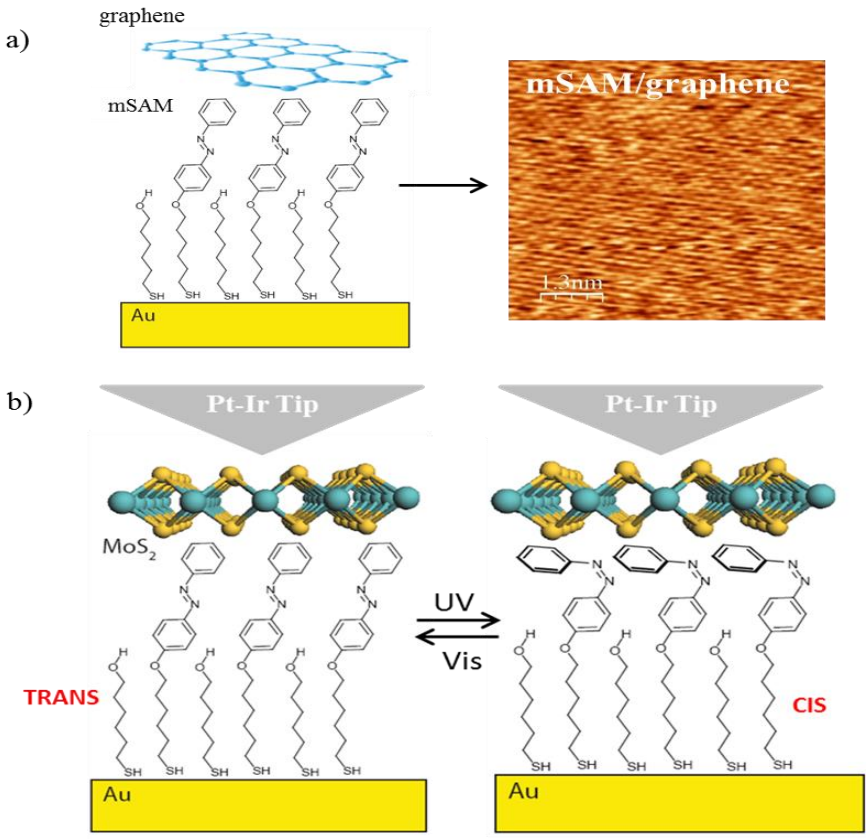

Figure 5.1 Schematics of 2D crystal-azobenzene-Au photoresponsive platforms. (a) The graphene-mSAM-Au platform with its STM image. (b) The MoS_2-mSAM-Au platform with the azobenzene molecules between *trans* (left) and *cis* (right) state by illumination.

One of the main challenges toward widespread use of molecular architectures in technology is the limited access to atomically-flat, ultra-clean platforms. It has been demonstrated[219] that thiol-terminated self-assembled monolayers (SAMs), provide means to smooth rough metallic interfaces. These interfaces can be subsequently passivated with 2D crystals such as graphene (Figure 5.1 (a)), boron nitride or MoS_2 (Figure 5.1 (a)), and pave the road to large-scale atomically-flat interfaces for technological applications. Here we study an azobenzene SAMs on gold substrates and MoS_2 as a novel prototype platform with embedded photoswitching functionality. The electronic properties between MoS_2 and the photochromic azobenzene molecules are investigated via conductive atomic force microscope (c-AFM) which is a powerful technique to record the local conductivity of the sample surface and the morphology simultaneously. We report on photoswitchable conduction measurements of mono- and multilayered MoS_2 on top of a self-assembled mSAM monolayer on gold. The self-assembled mSAM consists on 4-(1-mercapto-6-hexyloxy)-azobenezene mixed with spacer 6-(2-mercapto)-1-hexanol molecules in the ratio of 1 : 1. MoS_2 is mechanically exfoliated to allow a direct contact with the molecules. The fabricated heterojunctions show rectifier characteristics with ratios exceeding 10000 at ±1.5 V, as recorded by c-AFM. Particularly, leak currents of 0.1 pA nm^2 at -1.5 V sample bias are measured for the single-layer MoS_2/self-assembly monolayer heterostructure, with a nominal thickness below 26 Å. When the azobenzene monolayer is photoisomerized from *trans* to *cis* configuration, a transition from rectifier to symmetric conduction occurs. In this section, the characterization of all the samples both for the measurements of c-AFM and KPFM are performed using an *Asylum Research* commercial scanning probe microscope at room temperature and ambient conditions employing a *ASYELEC-01* Pt-Ir coated Si cantilever with a spring constant of ~ 2 N m^{-1} and an estimated tip radius of 28 ± 10 nm.

5.1 Electrical characterization of MoS_2-azobenzene-Au hybrid system

Point defects in atomic layer of MoS_2 are reported to lead to a native n-type or p-type of doping.[220, 221] Therefore, intuitively, either the use of photochromic molecules as electron donors/acceptors or work function modulators to functionalize the substrate, should result in the photoswitching and/or phototuning of the MoS_2 conductive properties. In this section we show that the current-voltage characteristics of single-layer MoS_2 can be optically tuned by means of photocromic azobenzene self-assembled monolayers (SAMs). Following the schematics of the hybrid system shown in Figure 5.1 (b), the MoS_2 flake is directly exfoliated on top of the functionalized sample (cf. section 2.2.1), resulting in several layer thicknesses. The thickness of the MoS_2 layers was recognized using Raman spectroscopy as shown in Figure 5.2. The Raman measurements are performed at room temperature and in air using as excitation source a green laser emitting at 514.532 nm with excitation power of 300 mW. The main Raman modes of MoS_2 are known as the in-plane (E^1_{2g}) and the out of plane (A_{1g}) modes, with characteristic positions for bulk MoS_2 centered at 383 cm^{-1} and at 408 cm^{-1}, respectively[222]. For a single layer MoS_2, the distance between the frequency modes E^1_{2g} and A_{1g} is around 18.5 cm^{-1}.[223]

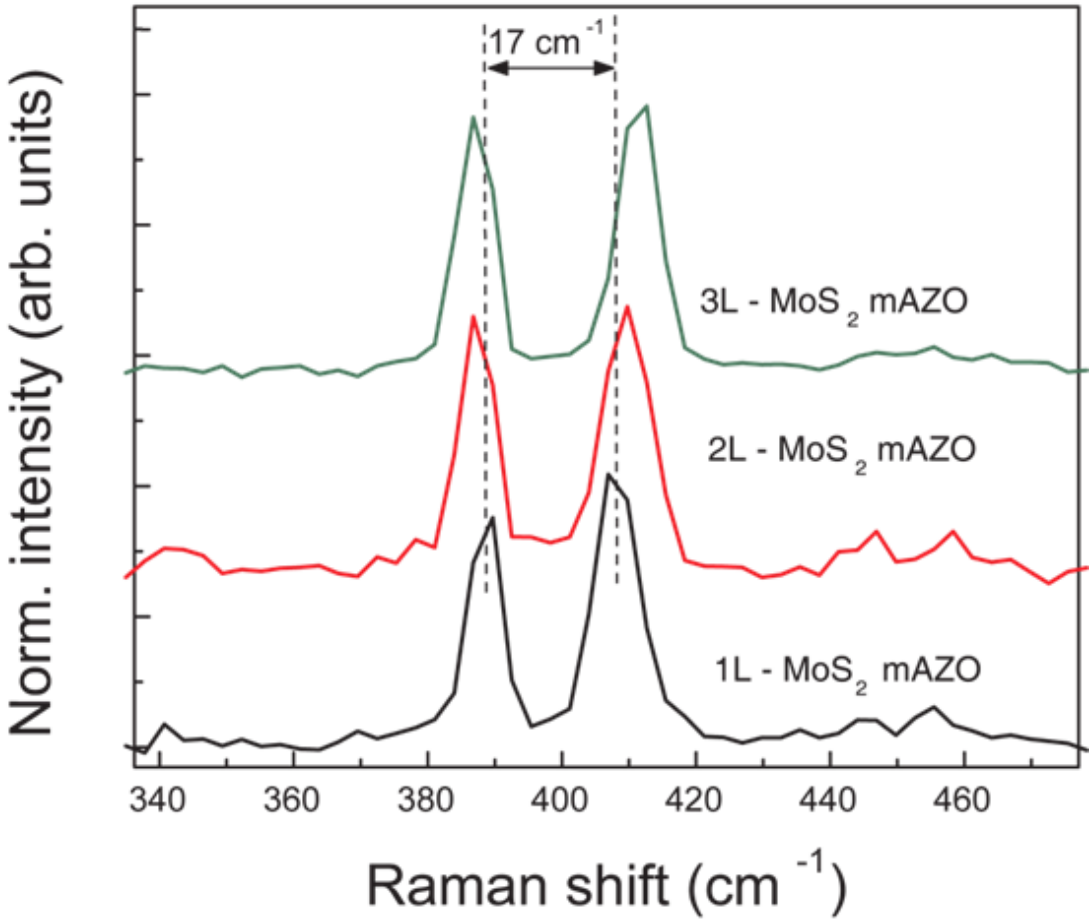

Figure 5.2 Microraman spectra of one, two and three layers MoS_2 on top of mSAM on a gold substrate.

In order to investigate the mechanism of electrical transport of MoS_2 layer on the mSAM, the *IV* traces are measured and plotted in semi-logarithmic scale as shown in Figure 5.3 (a) for a monolayer of MoS_2 directly exfoliated on *trans*-mSAM-Au substrate. The AFM morphology image of the multilayer MoS_2 exfoliated on the functionalised substrate is shown in Figure 5.3 (b). Importantly, the semi-logarithmic plot reveals that the *trans*-mSAM (Figure 5.3 (a), black line) is characterized for being a rectifier with a turn-on voltage close to 0.5 V. Additionally, heterostructures fabricated with graphene instead of MoS_2 never show similar diode-like characteristics, that signals the rectification as an exclusive property of the MoS_2 heterojunctions.[219, 224] It is worth noting that such rectification behavior is not observed in the

sample of bare *trans*-mSAM-Au shown in Figure 5.3 (c). Here, only a current enhancement when mSAM molecules switch from *trans* to *cis* state is observed. The increase in current is expected arising from the reduction of the molecular length and the subsequent lowering of the tunneling barrier length in *cis* configuration. For studying this effect, samples with different layers of MoS_2 are prepared. It is important to note that the turn-on voltages and rectification ratios can vary between samples with different layers of MoS_2 (Figure 5.3 (d)). The forward current shows an exponential behavior which can be assigned to tunnelling. In addition, the observed exponential forward currents and turn-on voltages are typical properties of electroluminescent organic devices, suggesting potential electroluminescence.[225, 226] The behavior of the turn-on voltage indicates the existence of a metal-semiconductor (MS) barrier caused by the differences in work function between the Pt-Ir tip and the MoS_2/mSAM heterostructure. In an MS barrier, a potential barrier prevents the electrons (or holes) migrating out or into the semiconductor. The migration requires an increase of bias to overcome the MS barrier. In contrast to the *trans* state, when the mSAM molecules are in metastable form (*cis* state), the rectification behavior of the MoS_2/mSAM disappears and a high current with perfect symmetric behavior between forward and reverse bias emerges. Since the MoS_2 is reported as an n-type semiconductor[221], the behavior observed when the molecules in *cis* state could be explained as a complete passivation of the point defects present in the MoS_2 multilayer. In other words, the *trans*-mSAM/gold system p-dopes the MoS_2, neutralizing the access to negative carriers.

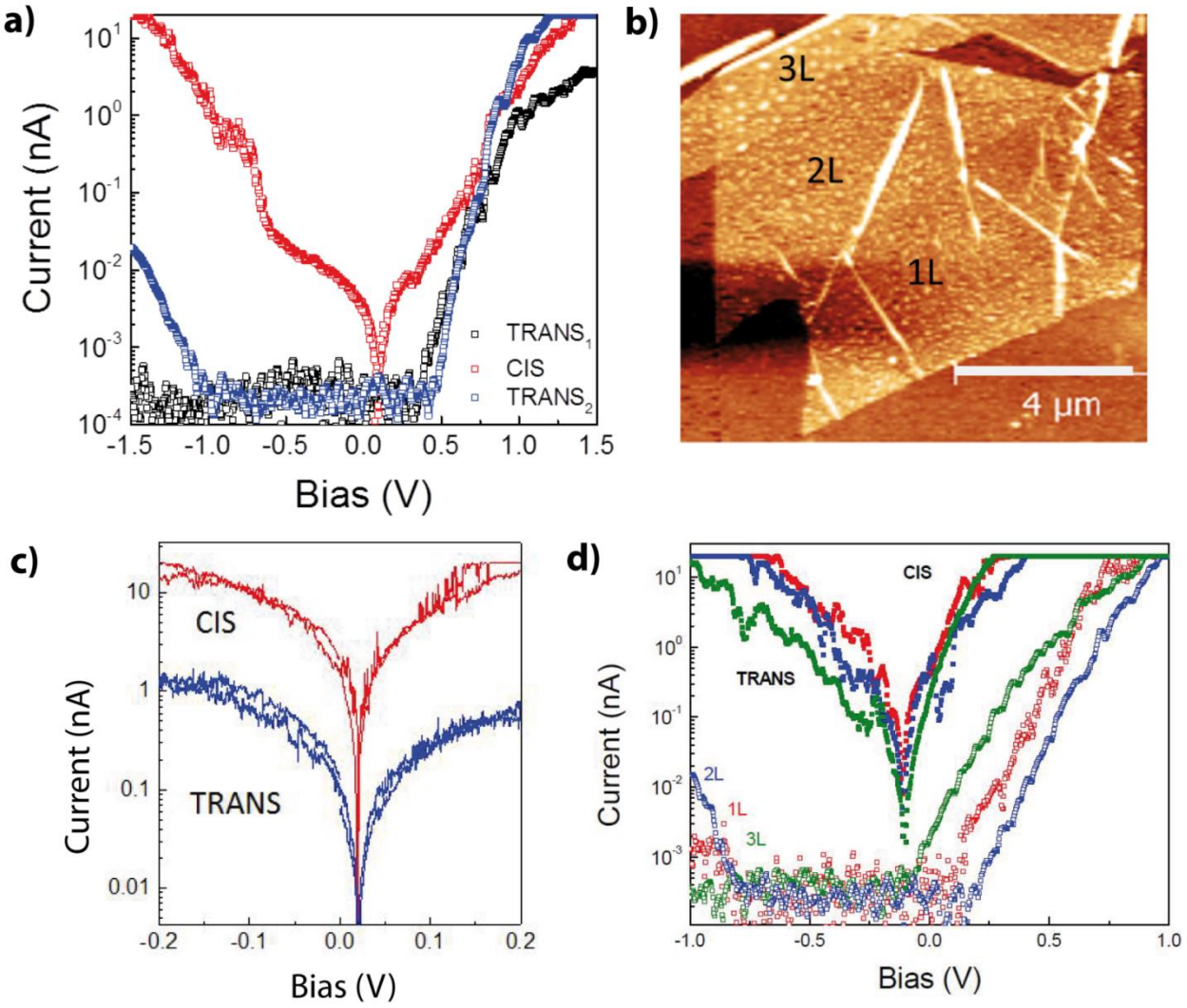

Figure 5.3 (a) *IV* characteristics in semi-logarithmic scale for 1L MoS_2/mSAM heterostructure before (*trans*$_1$), after UV (*cis*) exposure and after white light (*trans*$_2$) exposure. (b) AFM image of the multilayer MoS_2 flake exfoliated on the mSAM/Au substrate. (c) *IV* characteristics in semi-logarithmic scale for bare mSAM-Au sample from *trans* (blue trace) to *cis* (red trace) by means of c-AFM. (d) Additional *IV* spectra showing the effect of number of MoS_2 layers. For this preparation different layers are studied, the rectifier behavior for 1L and 2L is less pronounced and the forward turn-on current varies between 0 and 0.2 V.

It is worth examining some properties of the observed rectification in Figure 5.3 (a). The current changes from I_+ = 2 nA at +1.5 V to as low as I_- = 0.2 pA at -1.5 V for a ratio of 10000

on 1L MoS_2/*trans*-mSAM/Au sample. The rectifying current, or nanoscopic "leak current", is observed with a value of 5×10^{-13} A ≈ 0.1 A cm^{-2} at -1 V (considering a tip contact radius around 10 nm), which is close to the characteristic tunneling current for devices prepared with HS-$C_{10}H_{21}$ SAMs (~ 0.01 A cm^{-2} at -1 V) as reported by Whitesides *et al.*[227]. The molecules reported have comparable length as the HS-C_6 azobenzene employed in our work. Thus, we can estimate that leak current density of 1L MoS_2/*trans*-mSAM/Au hybrid system is below 0.01 pA nm^{-2}, which is exceptionally low given the low nominal thickness of the material (8.0 Å for 1L MoS_2[152] and ~ 18 Å for *trans*-mSAM[228]). Upon illuminating the sample of 1L MoS_2/*trans*-mSAM/Au with 366 nm UV-light, thus provoking conformational isomerization of the azobenzene molecules from *trans* to *cis*, the *IV* characteristics show remarkable different conductance behavior. We can observe the complete suppression of the rectification and the net enhanced current by close to 1.5 orders of magnitude in forward bias. Actually the current density of *cis*-mSAM (Figure 5.3 (a), red line) at 0.75 V is now as high as 10^3 A cm^{-2}. This tunneling current is now typical of HS-C_6H_{13} SAMs[227], which have comparable length to the spacer molecules applied in this work. This indicates that the lower forward current recorded for *trans*-mSAM is not a consequence of the insulating SAM length.

It is indicative from these observations and comparisons that the transport through the heterostructures can be explained by a combination of tunneling through an MS barrier (due to the contact resistance) and tunneling through the *trans*-mSAM layer. Notably, such tunneling characteristics are not observed on the sample of MoS_2 exfoliated directly on Au substrate (Figure 5.4), featuring negligible resistance up to 1 nA. Finally, rectification can be switched back again when illuminating the sample with a white light overnight (Figure 5.3 (a), blue line).

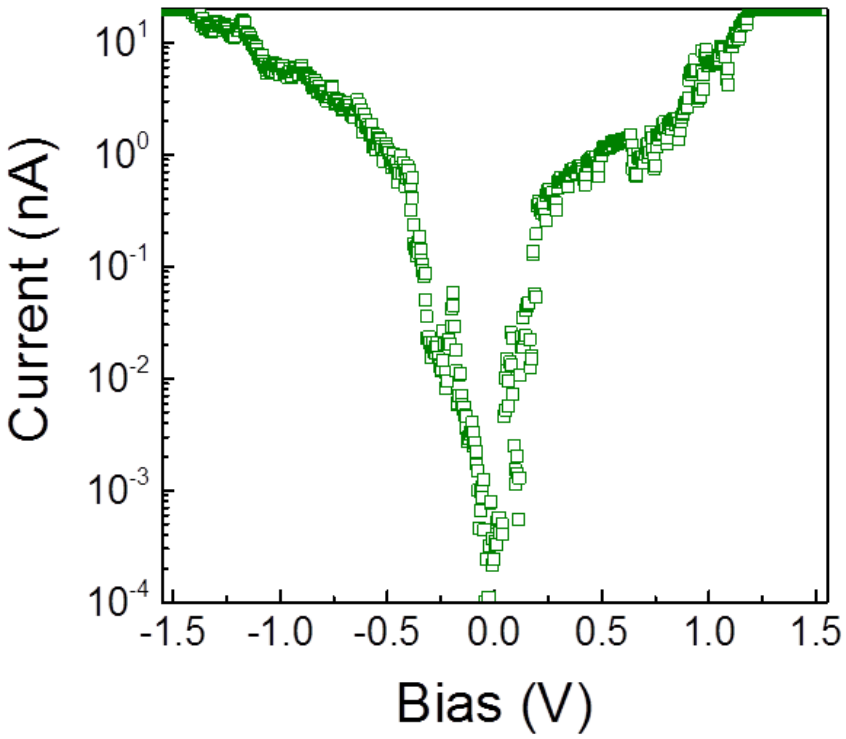

Figure 5.4 *IV* characteristics in semi-logarithmic scale for 1L MoS_2 exfoliated directly on Au substrate.

5.2 Rectifying mechanisms of MoS_2-azobenzene-Au hybrid system

Rectifying characteristics can originate from three different mechanisms: (1) an asymmetric tunneling junction[225], which is caused by different positions of the insulating and conducting units. (2) a Schottky diode, due to the MS barrier. (3) a p-n junction[229, 230] (or analogously, an Aviram-Ratner diode)[231, 232] between the 2D semiconductor and the molecules.

It is worth examining some properties of the observed rectification and reference samples in Figure 5.5. We investigate the *IV* characteristics of the samples from MoS_2 on substrates functionalized with only spacer molecules and only HS-C_6AZO molecules respectively. Figure

5.5 (a) reveals that HS-C_6AZO molecule (black line) is the component being responsible for the rectifying behavior, while the spacer molecule (grey line) shows characteristics reminiscent of the behavior of *cis*-mSAM. In order to give statistical evidence of the rectification, the c-AFM maps (Figure 5.5 (b), (c)) are performed at a voltage of 0.1 V which is lower than the turn-on voltage in *IV* data recorded on the sample of MoS_2/*trans*-mSAM/Au. As expected, we find typical leak currents values for the MoS_2/*trans*-mSAM heterostructure (10^{-12} A, blue line in Figure 5.5 (d)) and current saturation values for the plain *trans*-mSAM/Au (10^{-8} A, red line in Figure 5.5 (d)). Especially the current saturation is also observed on the sample of MoS_2/*trans*-mSAM/Au, which could be assigned to increased pressure exerted on grain boundaries of the gold substrate. This phenomenon also affects leak currents at negative voltages. In order to illustrate this effect more, we take the conductance maps at the 1L MoS_2/*trans*-mSAM boundary with plain *trans*-mSAM/Au. Figure 5.5 (e) shows complementary current measurements by c-AFM in a region of the boundary between the samples of 1L MoS_2/*trans*-mSAM/Au and bare *trans*-mSAM/Au. An obvious boundary is observed with conductivities < 1 pA (left, 1L MoS_2/*trans*-mSAM/Au) and > 10 pA (right, bare *trans*-mSAM/Au) at -1.5 V. The middle transition boundary where has the strongest c-AFM feedback contact forces, shows an increased conductivity. This reinforces the interpretation of variable rectification with forces exerted on the 1L MoS_2 flake.

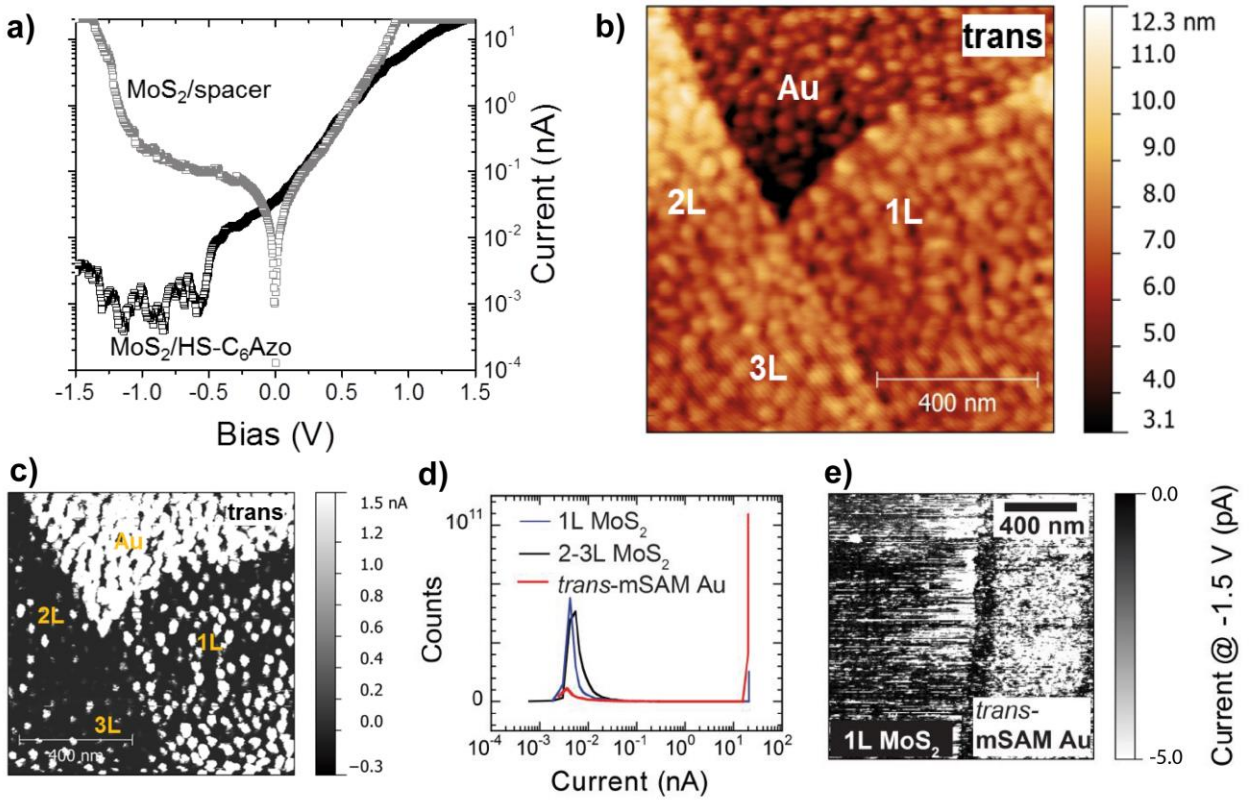

Figure 5.5 (a) *IV* characteristics for MoS_2/HSC$_6$-AZO (black line) and MoS_2/spacer (grey line). (b) AFM image of a multilayer MoS_2 exfoliated on *trans*-mSAM on Au substrate. (c) The respective conductive AFM data of (b) recorded at 0.1 V. (d) Distribution of currents in (c) showing high conduction through bare *trans*-mSAM/Au as compared to the MoS_2 overlayer. (e) Conductive AFM data recorded at -1.5 V of the boundary between 1L MoS_2/*trans*-mSAM/Au (left) and the bare *trans*-mSAM/Au (right) evidences strong rectifying behaviour of the former. The boundary appears as a central dark stripe.

Our systematic studies point out the unique interfaces and thus potential barriers between MoS_2 flake, *trans*-mSAM and gold substrate as being critical for the rectifier characteristics. Accordingly, the contact potential differences of the heterostructures are investigated by using kelvin probe force microscope (KPFM). This technique is widely used to study the surface potential of a material and therefore, to know about the material work function. By thinning the 2D material thickness, recording different number of layers from 10L down to 1L, the KPFM

gives information about the change of the surface potential induced by the electrostatic interaction between the substrate and the 2D nanosheet. Figure 5.6 (a) shows the KPFM measurements of switching series on different layers of MoS_2 flake between *trans*-mSAM (black dots), *cis*-mSAM (red dots) and back to *trans*-mSAM (blue dots) again. The contact potentials on the different samples feature small variations within the first three layers and sharply decrease for four layers. Additional evidence can be obtained from Figure 5.6 (b) as well. Importantly, reference sample of MoS_2/Au presents little to no change in the contact potential with number of layers (Figure 5.6 (c)). Unlike the case on the samples of MoS_2/SiO_x, strong changes of the contact potential have been assigned to SiO_x charging[233]. Note how unlike MoS_2/mSAMs *trans* or *cis* heterostructures, the contact potential of the reference sample prepared with MoS_2 and spacer molecule on Au follows an opposite trend: the contact potential sharply decreases for more than 3 - 4 layers shown in Figure 5.6 (d). Thus, the contact potential measured on the sample of MoS_2/mSAMs/Au is not influenced by electrostatic artifacts due to the measurement.

The highest contact potential (MS barrier) for the *trans*-mSAM system, is amounting to 1.03 ± 0.10 V. In contrast, on the sample of 1L MoS_2/*cis*-mSAM/Au, the contact potential shows a reduction of $\Delta\Phi$ = 0.36 V, to a value of 0.67 ± 0.10 V. Such contact potential change is higher than previously reported azobenzene-SAMs used for tuning the metal work function of the Au substrate.[156]

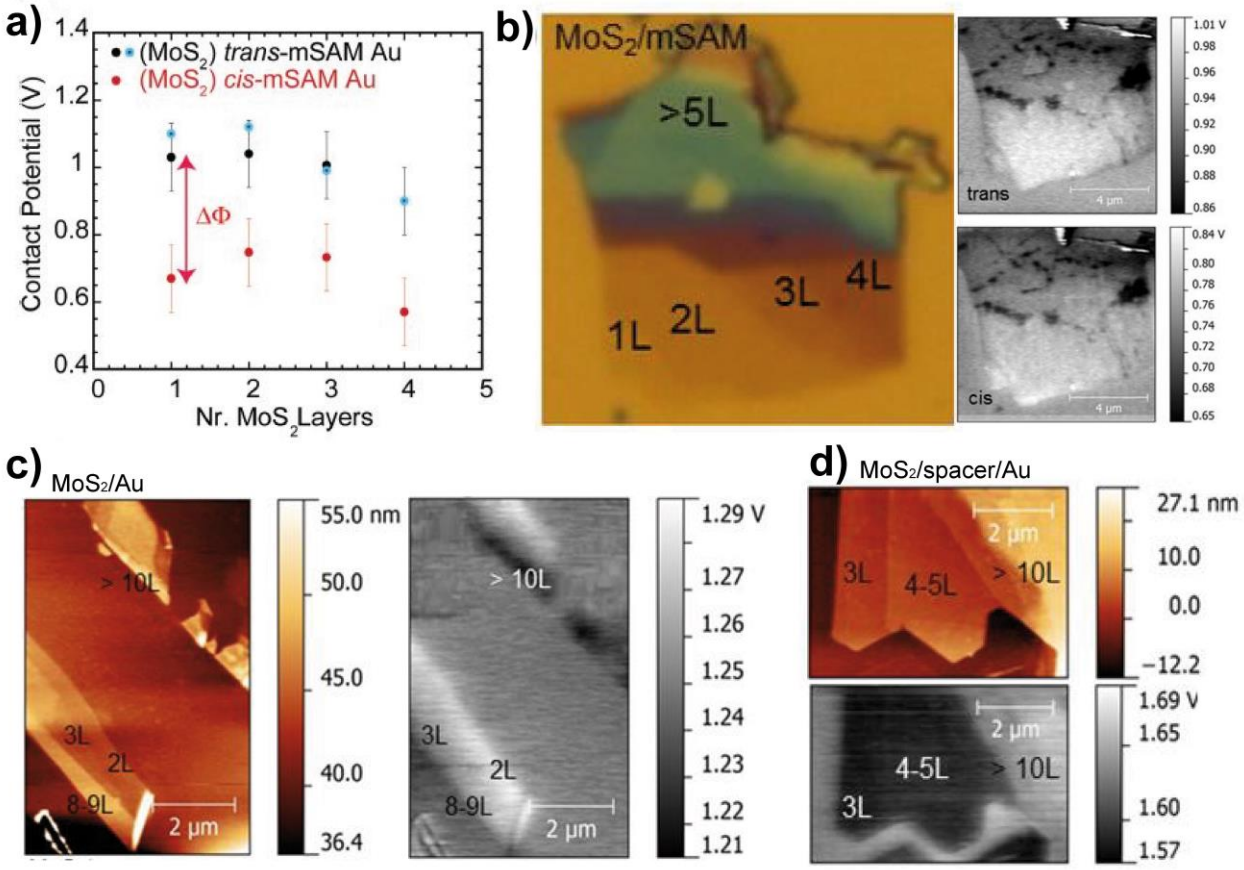

Figure 5.6 (a) KPFM measurements recorded from one, two, three and four layers of MoS_2 flake exfoliate on mSAM/Au between *trans*-mSAM (black dots), *cis*-mSAM (red dots) and back to *trans*-mSAM (blue dots) again. (b) Optical micrograph of multilayer MoS_2/mSAM on Au substrate and its corresponding KPFM measurements from MoS_2/*trans*-mSAM and MoS_2/*cis*-mSAM. (c) AFM morphology (left) and KPFM measurement (right) from multilayer MoS_2 flake exfoliated on Au substrate directly. (d) AFM morphology (top) and KPFM measurement (bottom) from multilayer MoS_2 flake exfoliated on spacer molecules alone (without HS-C_6AZO).

Explaining the photoswitchable experiment and rectification from an asymmetrical tunnelling model[225] point of view is reasonable: the lower the work function (higher contact potential) of the MoS_2, the more rectifying in the device since a larger potential drop is required to align the Au electrode and MoS_2 semiconductor Fermi levels. The energy level picture at equilibrium state is illustrated in Figure 5.7 (a), where the transport is chosen to occur mainly

through the conduction bands (E_{CB}) of MoS_2 on *trans*-mSAM (black) and *cis*-mSAM (red) for sake of simplicity. It is worth noting that valence bands can also be considered, being closer to the metals' work functions of ~ 5.7 eV for Pt-Ir electrode and ~ 5.1 eV for Au electrode.[234] A conduction or valence band transport picture between ±1.5 V can be ultimately corroborated if electroluminescence in the device is present or absent, respectively. Additionally, changes of the work function modulate the different doping levels of MoS_2[219, 235] so that transport channels might completely differ between *trans* and *cis* state. Therefore, the electron transport at forward bias occurs when the transport channel shifts downwards. And the transport channel is aligned with the left-side Pt-Ir electrode (Figure 5.7 (b)). On the other hand, rectification at reverse bias occurs until the right-hand Au electrode aligns with the upward shifting transport channel (Figure 5.7 (c)).

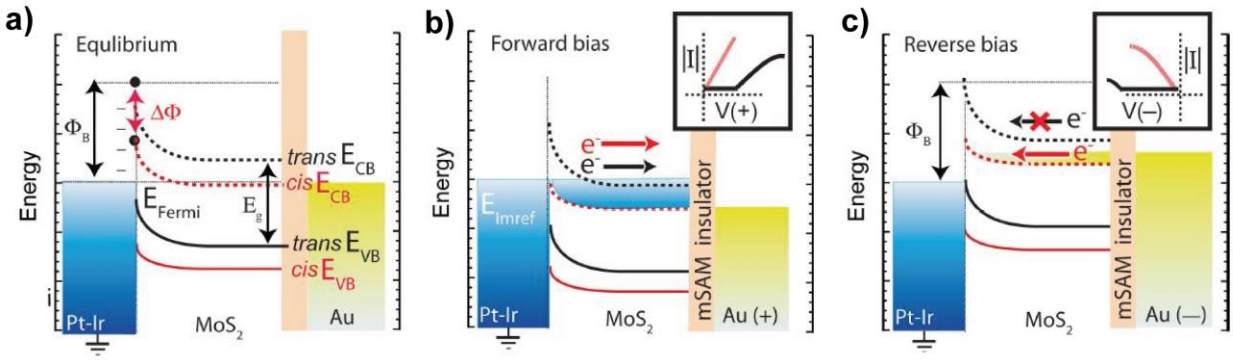

Figure 5.7 Schematics of the metal-semiconductor rectification barrier between the grounded Pt-Ir tip and the MoS_2/mSAM/Au heterostructure. In order for rectification to occur uniquely in the *trans*-mSAM device, the Fermi energy of the Pt-Ir tip must be pinned between the Fermi energies of the *trans*-mSAM and *cis*-mSAM. The transport channel of MoS_2/*cis*-mSAM is closer to the electrodes' Fermi level at equilibrium (a) and transport readily occurs at any bias. The misaligned transport channel for the MoS_2/*trans*-mSAM heterostructure at equilibrium (a) requires larger bias for transport at the corresponding polarities ((b)-(c)).

The mechanism of rectification on the right Au electrode is similar to the one reported by Kornilovitch and Williams[225], where the energy levels of the (semi)conductor is shifted up and down by a potential drop through the interfaces. The conduction band of the *cis*-mSAM

(semi)conductor lies closer to the Fermi level of the electrodes and hence could readily align and transport at any bias. Oppositely, the conduction band of the *trans*-mSAM lies far from the right Au electrode. However, unlike the mechanism proposed by Kornilovitch and Williams[225], here we suggest that the largest potential drop occurs on the left Pt-Ir electrode and not on the SAM insulator, that is contributed by the formation of a MS with screening dipoles barrier at the former. Thus, screening dipoles or depletion layers at interfaces might provide an interesting avenue to design promising ultra-thin rectifiers. It is worth to mention that the rectifier mechanism we observed in this work follows an opposite trend for both Schottky rectifiers and Aviram-Ratner rectifiers. For the former case, the MS barrier and thus depletion layer should increase at a positive sample bias. Here we suggest that in such atomically-thin MoS_2 flake, the depletion layer is small and not increased easily. For the latter case, the computed highest occupied electronic levels of MoS_2 is -5.2 eV[220] and *trans*-azobenene is -4.8 eV, which would block transport in forward bias, yet allow holes to flow from the tip ($E_F \approx$ -5.7 eV) to the sample when the Au substrate ($E_F \approx$ -5.1 eV) is biased negatively.

Since the typical diode and conductor behavior are observed on the samples of MoS_2/mSAM/Au in *trans* and *cis* state respectively, it is worth to build a 2D molecularly photogated transistor device for further study. This phototransistor is fabricated with a MoS_2 flake and mSAM made of azobenzene and spacer molecules as same as mentioned above. For simplification, the device is initially achieved by fabricating an interdigitated Au electrode by means of optical lithography and wet chemical etching as illustrated in section 2.3.1. Afterwards, we functionalise the Au electrodes with the azobenzene mSAM and transfer a nearly monolayer MoS_2 flake on top of the target electrodes. The device shows a small diode-like behavior when mSAM molecules are in *trans* state, as expected from the c-AFM studies of bare mSAMs (Figure 5.8). This work is published on *Advanced Materials*.[236]

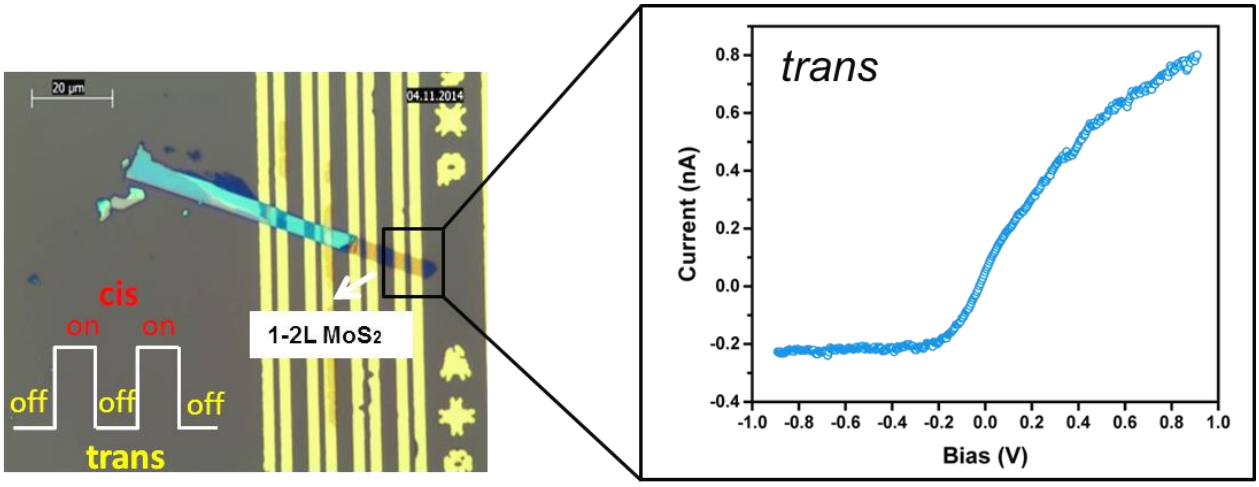

Figure 5.8 Optical micrograph of MoS_2 flake transferred on functionalized interdigitated Au electrode (left) and the *IV* characteristics showing a diode-like behavior when molecules are in *trans* (right).

Chapter 6

Conclusions and Outlook

The fabrication and characterization of optoelectronic device elements integrating molecular architectures at interfaces were presented in this thesis. The hydrogen-bonded structures of supramolecular assemblies consisting of melamine-naphthalene diimide networks were explored via scanning tunneling microscope (STM) at the solution-liquid interface under ambient conditions. Scanning tunneling spectroscopy (STS) provided insight into the optoelectronic properties of the active layer which is a self-assembled porous monolayer formed by melamine and terrylene-based dye (TDI) molecule on a transparent platform. Moreover, electrical properties of a photoswitchable platform were investigated by means of conductive atomic force microscope (c-AFM).

Regarding photoresponsive characteristics, firstly, a model 3D supramolecular framework assembled on an all-carbon sp^2-sp^3 transparent hybrid platform was fabricated under ambient conditions. The hybrid platform consisted of a commercial CVD-grown graphene transferred to a technologically relevant high-quality hydrogenated CVD diamond substrate. The bilayer nanoporous supramolecular framework consisting of melamine and 1,4,5,8-naphthalene tetracarboxylic diimide (NTCDI) was explored via STM initially at the solution-highly oriented pyrolytic graphite (HOPG) interface. Comparative studies of the nanoporous network on HOPG allowed to extract growth rates of the bilayers and showed how solvent controls the tendency of the bilayers to form boundaries, reflecting NTCDI-NTCDI interactions. Moreover, molecular mechanic studies gave insight into the preferential face-to-face vdW stacking of melamine-NTCDI dimers. This work shows how precise π-stacking of a polyaromatic molecule is possible

in a bicomponent supramolecular network. The finding is important for the fabrication and optimization of organic optoelectronic devices toward self-assembly-assisted 3D molecular architectures.

Based on the previous studies of bicomponent supramolecular bottom-up self-assembly in nanoscale, a nanoporous network featuring a chromophore absorbing in the far red as the active layer was employed, thereby opening the possibility of monolayer, sensitized, (supra)molecular photovoltaics. We successfully demonstrated this concept, showing for the first time the macroscopic photovoltaic characterization of a supramolecular surface assembly. The supramolecular assembly at the graphene-diamond interface shows a maximum absorption peak at 740 nm. A 0.5 nA photocurrent and 270 mV open circuit voltage are obtained when employing 19 mW cm^{-2} irradiation intensities at 710 nm on the molecular active layer. The non-optimized photovoltaic device element configuration yields an IPCE as high as 0.6% in air by *ex situ* estimations of the tunneling area, which is rationalized by the high intrinsic absorptivity of the monolayer (~ 1%), excellent exciton dissociation and charge transport. Particularly, through the study of the photoresponsive monolayer photovoltaic device, we highlighted how, almost a decade since the introduction of bottom-up modular self-assembly[237-239] and *in situ* on-surface synthesis[7] for atomically-precise fabrication, serious efforts are still required for molecularly precise fabrication, with high throughput dedicated analytical instrumentation simply lacking.

Finally, we employed a self-assembled monolayer to fabricate a photoresponsive hybrid platform. A photoswitchable diode device element, a hybrid system of exfoliated monolayer MoS_2 flake on a gold substrate functionalized with azobenzene molecules was fabricated and characterized by means of c-AFM. When the azobenezene molecules were in the stable state (*trans*), the behavior was similar with the absence of molecules but the rectification was much larger. On the other hand, when the azobenzene molecules were in metastable state (*cis*), the rectification behavior disappeared and a strong current enhancement with a perfect symmetry between forward and reverse bias was observed. It can be concluded that there is an abrupt change of current density from rectification to symmetric transport when photoisomerizing the azobenzene molecules from *trans* to *cis* conformation. Furthermore, measuring the surface potentials by kelvin probe force microscope (KPFM), we deduced that the photoswitchable transport characteristics can be attributed to large different contact potentials between *trans*-mSAM/Au and *cis*-mSAM/Au. This work demonstrated interesting electrical features of the

hybrid system, such as strong and controllable current enhancement by switching the azobenzene molecules which might lead to a variety of applications in future optoelectronics. Accordingly, a prototype MoS_2 transistor with an atomically photoswitchable gate was realized. However, further experiments on electrical transport measurements are still required and the performance of the device has to be optimized as well.

Altogether, photoresponsive multicomponent molecular architectures at interfaces were designed and realized. The integrated self-assembled architectures have been locally characterized with molecular precision by means of scanning probe technology. We have demonstrated important advances in establishing the field of complex molecularly precise devices. We expect to create well-defined molecularly precise devices via photo-/electron beam lithography at organic/inorganic interfaces, especially to fabricate layer-by-layer photosynthetic architecture mimics, combine the photoswitchable platform of Chapter 5 with the photovoltaic molecular architectures of Chapter 4 and study their physico-chemical and optoelectronic properties in the near future.

Bibliography

1. Barth, J. V.; Costantini, G.; Kern, K. *Nature* **2005,** 437, 671-679.
2. Wieghold, S.; Li, J.; Simon, P.; Krause, M.; Avlasevich, Y.; Li, C.; Garrido, J. A.; Heiz, U.; Samorì, P.; Müllen, K.; Esch, F.; Barth, J. V.; Palma, C.-A. *Nat Commun* **2016,** 7.
3. Whitesides, G. M.; Mathias, J. P.; Seto, C. T. *Science* **1991,** 254, 1312-1319.
4. Ball, P. *Nature* **1994,** 367, 323-324.
5. Ulman, A. *Chem. Rev.* **1996,** 96, 1533-1554.
6. Zwaneveld, N. A. A.; Pawlak, R.; Abel, M.; Catalin, D.; Gigmes, D.; Bertin, D.; Porte, L. *J. Amer. Chem. Soc.* **2008,** 130, 6678-6679.
7. Grill, L.; Dyer, M.; Lafferentz, L.; Persson, M.; Peters, M. V.; Hecht, S. *Nature nanotechnology* **2007,** 2, (11), 687-91.
8. Liu, X. H.; Guan, C. Z.; Ding, S. Y.; Wang, W.; Yan, H. J.; Wang, D.; Wan, L. J. *J. Am. Chem. Soc.* **2013,** 135, 10470-10474.
9. Lehn, J.-M. *Science* **2002,** 295, 2400-2403.
10. Bhosale, S. V.; Jani, C. H.; Langford, S. J. *J. Chem. Soc. Rev.* **2008,** 37, 331-342.
11. Sakamoto, J.; van Heijst, J.; Lukin, O.; Schluter, A. D. *Angewandte Chemie-International Edition* **2009,** 48, (6), 1030-1069.
12. Colson, J. W.; Dichtel, W. R. *Nature Chem.* **2013,** 5, (6), 453-465.
13. Braga, D.; Grepioni, F.; Desiraju, G. R. *Chem. Rev.* **1998,** 98, (4), 1375-1406.
14. Hosseini, M. W. *Acc. Chem. Res.* **2005,** 38, (4), 313-323.
15. Palma, C. A.; Samorì, P. *Nature Chem.* **2011,** 3, (6), 431-436.
16. Theobald, J. A.; Oxtoby, N. S.; Phillips, M. A.; Champness, N. R.; Beton, P. H. *Nature* **2003,** 424, 1029-1031.
17. Palma, C. A.; Björk, J.; Bonini, M.; Dyer, M. S.; Llanes-Pallas, A.; Bonifazi, D.; Persson, M.; Samorì, P. *J. Am. Chem. Soc.* **2009,** 131, (36), 13062-71.

18. Barth, J. V. *Annu. Rev. Phys. Chem.* **2007,** 58, 375-407.

19. Zwaneveld, N. A.; Pawlak, R.; Abel, M.; Catalin, D.; Gigmes, D.; Bertin, D.; Porte, L. *J. Am. Chem. Soc.* **2008,** 130, (21), 6678-9.

20. Ciesielski, A.; Cadeddu, A.; Palma, C.-A.; Gorczyński, A.; Patroniak, V.; Cecchini, M.; Samorì, P. *Nanoscale* **2011,** 3, 4125-4129.

21. Whitelam, S.; Tamblyn, I.; Haxton, T. K.; Wieland, M. B.; Champness, N. R.; Garrahan, J. P.; Beton, P. H. *Phys. Rev. X* **2014,** 4, (1).

22. Palma, C. A.; Samorì, P.; Cecchini, M. *J. Am. Chem. Soc.* **2010,** 132, (50), 17880-17885.

23. Li, J.; Wieghold, S.; Oner, M. A.; Simon, P.; Hauf, M. V.; Margapoti, E.; Garrido, J. A.; Esch, F.; Palma, C. A.; Barth, J. V. *Nano Lett.* **2014,** 14, (8), 4486-4492.

24. Halls, J. J. M.; Walsh, C. A.; Greenham, N. C.; Marseglia, E. A.; Friend, R. H.; Moratti, S. C.; Holmes, A. B. *Nature* **1995,** 376, (6540), 498-500.

25. Gunes, S.; Neugebauer, H.; Sariciftci, N. S. *Chem. Rev.* **2007,** 107, (4), 1324-1338.

26. Garcia, R.; Martinez, R. V.; Martinez, J. *Chemical Society reviews* **2006,** 35, (1), 29-38.

27. Haga, M.-a.; Kobayashi, K.; Terada, K. *Coordination Chemistry Reviews* **2007,** 251, (21–24), 2688-2701.

28. Fichou, D. *Journal of Materials Chemistry* **2000,** 10, (3), 571-588.

29. Koch, N. *Chemphyschem : a European journal of chemical physics and physical chemistry* **2007,** 8, (10), 1438-1455.

30. Grimsdale, A. C.; Müllen, K. *Angewandte Chemie International Edition* **2005,** 44, (35), 5592-5629.

31. Dincă, M.; Long, J. R. *Angewandte Chemie International Edition* **2008,** 47, (36), 6766-6779.

32. Liang, H.; He, Y.; Ye, Y.; Xu, X.; Cheng, F.; Sun, W.; Shao, X.; Wang, Y.; Li, J.; Wu, K. *Coordination Chemistry Reviews* **2009,** 253, (23–24), 2959-2979.

33. Miyashita, N.; Kurth, D. G. *Journal of Materials Chemistry* **2008,** 18, (23), 2636-2649.

34. Jeffrey, G. A. *Oxford University Press* **1997,** New York.

35. Philp, D.; Stoddart, J. F. *Angew. Chem. Int. Ed. Engl.* **1996,** 35, 1154-1196.

36. Veciana, J.; Cirujeda, J.; Rovira, C.; Molins, E.; Novoa, J. J. *J. Phys. I* **1996,** 6, 1967.

37. Eichhorst-Gerner, K.; Stabel, A.; Moessner, G.; Declerq, D.; Valiyaveettil, S.; Enkelmann, V.; Müllen, K.; Rabe, P. *Angew. Chem. Int. Ed. Engl.* **1996,** 35, 1492-1495.

38. Sijbesma, R. P.; Beijer, F. H.; Brunsveld, L.; Folmer, B. J. B.; Hirschberg, J. H. K. K.; Lange, R. F. M.; Lowe, J. K. L.; Meijer, E. W. *Science* **1997,** 278, 1601-1603.

39. Jolliffe, K. A.; Timmermann, P.; Reinhoudt, D. N. *Angew. Chem. Int. Ed.* **1999,** 38, 933-937.

40. Griessl, S.; Lackinger, M.; Edelwirth, M.; Hietschold, M.; Heckl, W. M. *Single Mol* **2002,** 3, (25).

41. Kampschulte, L.; Lackinger, M.; Maier, A. K.; Kishore, R. S. K.; Griessl, S.; Schmittel, M.; Heckl, W. M. *J. Phys. Chem. B* **2006,** 110, (10829).

42. Ye, Y.; Sun, W.; Wang, Y.; Shao, X.; Xu, X. G.; Cheng, F.; Li, J.; Wu, K. *J. Phys. Chem. C* **2007,** 111, (10138).

43. Lu, J.; Zeng, Q.-d.; Wang, C.; Zheng, Q.-y.; Wan, L.; Bai, C. *Journal of Materials Chemistry* **2002,** 12, (10), 2856-2858.

44. Shi, Z.; Lin, N. *Chemphyschem : a European journal of chemical physics and physical chemistry* **2010,** 11, (1), 97-100.

45. Auwärter, W.; Weber-Bargioni, A.; Brink, S.; Riemann, A.; Schiffrin, A.; Ruben, M.; Barth, J. V. *Chemphyschem : a European journal of chemical physics and physical chemistry* **2007,** 8, (2), 250-4.

46. Silly, F.; Shaw, A. Q.; Briggs, G. A. D.; Castell, M. R. *Applied Physics Letters* **2008,** 92, (2), 023102.

47. Barth, J. V.; Weckesser, J.; Cai, C.; Günter, P.; Günter, P.; Jeandupeux, O.; Kern, K. *Angew. Chem. Int. Ed.* **1999,** 2000, (39), 1230-1234.

48. Madueno, R.; Raisanen, M. T.; Silien, C.; Buck, M. *Nature* **2008,** 454, (7204), 618-621.

49. Pinheiro, L. S.; Temperini, M. L. A. *Surface Science* **2007,** 601, (8), 1836-1843.

50. Payer, D.; Comisso, A.; Dmitriev, A.; Strunskus, T.; Lin, N.; Wöll, C.; DeVita, A.; Barth, J. V.; Kern, K. *Chemistry – A European Journal* **2007,** 13, (14), 3900-3906.

51. Kampschulte, L.; Griessl, S.; Heckl, W. M.; Lackinger, M. *The journal of physical chemistry. B* **2005,** 109, (29), 14074-8.

52. Binnig, G.; Rohrer, H.; Gerber, C.; Weibel, E. *Applied Physics Letters* **1982,** 40, (2), 178-180.

53. Binnig, G.; Rohrer, H.; Gerber, C.; Weibel, E. *Physical Review Letters* **1982,** 49, (1), 57-61.

54. Chen, C. J. *Oxford University Press: Oxford* **2008**.

55. Technologies, A. *Agilent 5100 SPM User's Guide* **2008**.

56. Stroscio, J. A. *Academic Press, Inc.* **1993**.

57. Morita, S. *Springer Verlag* **2007**.

58. Atkins. *Wiley-VCH: Weinheim* **2001**.

59. Bardeen, J. *Physical Review Letters* **1961,** 6, (2), 57-59.

60. Tersoff, J.; Hamann, D. R. *Physical Review B* **1985,** 31, (2), 805-813.

61. Bonnell, D. A. *New York: Wiley-NCH, Inc.* **2001**.

62. Morris, V. J.; Kirby, A. R.; Gunning, A. P. *London: Imperial College Press* **1999**.

63. Lennard-Jones; Cohesion, J. E. *Proceedings of the Physical Society* **1931,** 43, 461-482.

64. Ruskell, T. G.; Workman, R. K.; Chen, D.; Sarid, D.; Dahl, S.; Gilbert, S. *APPLIED PHYSICS LETTERS* **1996,** 68, (1), 93-95.

65. Olbrich, A.; Ebersberger, B.; Boit, C. *Applied Physics Letters* **1998,** 73, (21), 3114.

66. Oh, J.; Nemanich, R. J. *Journal of Applied Physics* **2002,** 92, (6), 3326.

67. C. Manos, A. S., B. Chriss, M. Rutgers. *ORCA Conductive AFM Manual* **2008**.

68. Reichmanis, E.; Katz, H.; Kloc, C.; Maliakal, A. *Bell Labs Technical Journal* **2005,** 10, (3), 87-105.

69. Sung, C.-F.; Kekuda, D.; Chu, L. F.; Lee, Y.-Z.; Chen, F.-C.; Wu, M.-C.; Chu, C.-W. *Advanced materials* **2009,** 21, (47), 4845-4849.

70. Sirringhaus, H. *Advanced materials* **2005,** 17, (20), 2411-2425.

71. Forrest, S. R. *Nature* **2004,** 428, (6986), 911-918.

72. Tang, Q.; Li, L.; Song, Y.; Liu, Y.; Li, H.; Xu, W.; Liu, Y.; Hu, W.; Zhu, D. *Advanced materials* **2007,** 19, (18), 2624-2628.

73. Tang, C. W.; VanSlyke, S. A. *Appl. Phys. Lett.* **1987,** 51, (12), 913.

74. Tang, C. W. *Appl. Phys. Lett.* **1986,** 48, (2), 183-185.

75. Bube, R. H. *London: Imperial College Press* **1998**.

76. Becquerel, A. E. *Comptes Rendus* **1839,** 9, (561).

77. Hertwich, E. G.; Gibon, T.; Bouman, E. A.; Arvesen, A.; Suh, S.; Heath, G. A.; Bergesen, J. D.; Ramirez, A.; Vega, M. I.; Shi, L. *Proceedings of the National Academy of Sciences* **2015,** 112, (20), 6277-6282.

78. Collin, G.; Höke, H.; Talbiersky, J., Anthracene. In *Ullmann's Encyclopedia of Industrial Chemistry*, Wiley-VCH Verlag GmbH & Co. KGaA: 2000.

79. Weigert, F. **1909**, 109.

80. Pulfrey, L. D. *New York: Van Nostrand Reinhold Co.* **1978**.

81. Spanggaard, H.; Krebs, F. C. *Solar Energy Materials and Solar Cells* **2004,** 83, (2–3), 125-146.

82. Youn, H.; Park, H. J.; Guo, L. J. *Small* **2015,** 11, (19), 2228-2246.

83. Weil, T.; Vosch, T.; Hofkens, J.; Peneva, K.; Müllen, K. *Angew. Chem. Int. Ed. Engl.* **2010,** 49, (48), 9068-93.

84. Wasielewski, M. R. *The Journal of Organic Chemistry* **2006,** 71, (14), 5051-5066.

85. Sonar, P.; Fong Lim, J. P.; Chan, K. L. *Energy & Environmental Science* **2011,** 4, (5), 1558-1574.

86. Sommer, M. *Journal of Materials Chemistry C* **2014,** 2, (17), 3088-3098.

87. Müllen, K. *ACS Nano* **2014,** 8, (7), 6531-6541.

88. Mikroyannidis, J. A.; Stylianakis, M. M.; Sharma, G. D.; Balraju, P.; Roy, M. S. *The Journal of Physical Chemistry C* **2009,** 113, (18), 7904-7912.

89. N., R. P. *Nova Science Publishers* **2007**.

90. Mazzio, K. A.; Luscombe, C. K. *Chemical Society reviews* **2015,** 44, (1), 78-90.

91. Li, C.; Liu, M.; Pschirer, N. G.; Baumgarten, M.; Müllen, K. *Chemical Reviews* **2010,** 110, (11), 6817-6855.

92. Peumans, P.; Uchida, S.; Forrest, S. R. *Nature* **2003,** 425, (6954), 158-162.

93. Yu, G.; Gao, J.; Hummelen, J. C.; Wudl, F.; Heeger, A. J. *Science* **1995,** 270, (5243), 1789-1791.

94. Schmidt-Mende, L.; Fechtenkötter, A.; Müllen, K.; Moons, E.; Friend, R. H.; MacKenzie, J. D. *Science* **2001,** 293, (5532), 1119-1122.

95. Lee, M. R.; Eckert, R. D.; Forberich, K.; Dennler, G.; Brabec, C. J.; Gaudiana, R. A. *Science* **2009,** 324, (5924), 232-235.

96. van Hal, P. A.; Wienk, M. M.; Kroon, J. M.; Verhees, W. J. H.; Slooff, L. H.; van Gennip, W. J. H.; Jonkheijm, P.; Janssen, R. A. J. *Advanced materials* **2003,** 15, (2), 118-121.

97. McGehee, M. D.; Topinka, M. A. *Nat Mater* **2006,** 5, (9), 675-676.

98. Nelson, J. *Current Opinion in Solid State and Materials Science* **2002,** 6, (1), 87-95.

99. Hoppe, H.; Sariciftci, N. S. *Journal of Materials Research* **2004,** 19, (07), 1924-1945.

100. Taima, T.; Chikamatsu, M.; Yoshida, Y.; Saito, K.; Yase, K. *Applied Physics Letters* **2004,** 85, (26), 6412-6414.

101. Cao, W.; Xue, J. *Energy & Environmental Science* **2014,** 7, (7), 2123-2144.

102. Cao, Y.; Yu, G.; Zhang, C.; Menon, R.; Heeger, A. J. *Synthetic Metals* **1997,** 87, (2), 171-174.

103. Heywang, G.; Jonas, F. *Advanced materials* **1992,** 4, (2), 116-118.

104. Park, S. H.; Roy, A.; Beaupre, S.; Cho, S.; Coates, N.; Moon, J. S.; Moses, D.; Leclerc, M.; Lee, K.; Heeger, A. J. *Nat Photon* **2009,** 3, (5), 297-302.

105. Moon, J. S.; Jo, J.; Heeger, A. J. *Advanced Energy Materials* **2012,** 2, (3), 304-308.

106. Ma, W.; Yang, C.; Gong, X.; Lee, K.; Heeger, A. J. *Advanced Functional Materials* **2005,** 15, (10), 1617-1622.

107. Barito, A.; Sykes, M.; Bilby, D.; Amonoo, J.; Jin, Y.; Morris, S.; Green, P.; Kim, J.; Shtein, M. *Journal of Applied Physics* **2013,** 113, (20), 203110.

108. Xiao, X.; Zimmerman, J. D.; Lassiter, B. E.; Bergemann, K. J.; Forrest, S. R. *Applied Physics Letters* **2013,** 102, 073302.

109. Weickert, J.; Dunbar, R. B.; Hesse, H. C.; Wiedemann, W.; Schmidt-Mende, L. *Advanced materials* **2011,** 23, (16), 1810-1828.

110. He, X.; Gao, F.; Tu, G.; Hasko, D. G.; Hüttner, S.; Greenham, N. C.; Steiner, U.; Friend, R. H.; Huck, W. T. *Advanced Functional Materials* **2011,** 21, (1), 139-146.

111. Peet, J.; Kim, J. Y.; Coates, N. E.; Ma, W. L.; Moses, D.; Heeger, A. J.; Bazan, G. C. *Nat Mater* **2007,** 6, (7), 497-500.

112. Ross, R. B.; Cardona, C. M.; Guldi, D. M.; Sankaranarayanan, S. G.; Reese, M. O.; Kopidakis, N.; Peet, J.; Walker, B.; Bazan, G. C.; Van Keuren, E.; Holloway, B. C.; Drees, M. *Nat Mater* **2009,** 8, (3), 208-212.

113. He, Y.; Chen, H.-Y.; Hou, J.; Li, Y. *Journal of the American Chemical Society* **2010,** 132, (15), 5532-5532.

114. Zhou, E.; Cong, J.; Wei, Q.; Tajima, K.; Yang, C.; Hashimoto, K. *Angewandte Chemie International Edition* **2011,** 50, (12), 2799-2803.

115. Schubert, M.; Dolfen, D.; Frisch, J.; Roland, S.; Steyrleuthner, R.; Stiller, B.; Chen, Z.; Scherf, U.; Koch, N.; Facchetti, A.; Neher, D. *Advanced Energy Materials* **2012,** 2, (3), 369-380.

116. Li, H.; Kim, F. S.; Ren, G.; Jenekhe, S. A. *Journal of the American Chemical Society* **2013,** 135, (40), 14920-14923.

117. Zhou, Y.; Yan, Q.; Zheng, Y.-Q.; Wang, J.-Y.; Zhao, D.; Pei, J. *Journal of Materials Chemistry A* **2013,** 1, (22), 6609-6613.

118. Zhou, Y.; Kurosawa, T.; Ma, W.; Guo, Y.; Fang, L.; Vandewal, K.; Diao, Y.; Wang, C.; Yan, Q.; Reinspach, J.; Mei, J.; Appleton, A. L.; Koleilat, G. I.; Gao, Y.; Mannsfeld, S. C. B.; Salleo, A.; Ade, H.; Zhao, D.; Bao, Z. *Advanced materials* **2014,** 26, (22), 3767-3772.

119. Hwang, Y.-J.; Courtright, B. A. E.; Ferreira, A. S.; Tolbert, S. H.; Jenekhe, S. A. *Advanced materials* **2015,** 27, (31), 4578-4584.

120. Russew, M. M.; Hecht, S. *Advanced materials* **2010,** 22, (31), 3348-60.

121. Ferri, V.; Elbing, M.; Pace, G.; Dickey, M. D.; Zharnikov, M.; Samorì, P.; Mayor, M.; Rampi, M. A. *Angewandte Chemie International Edition* **2008,** 47, (18), 3407-3409.

122. Feringa, B. L. *Wiley-VCH: Weinheim, Germany* **2001**.

123. Sinicropi, A. *CRITICAL REVIEWS*.

124. H. Bouas-Laurent, H. D. *Pure Appl.Chem.* **2001,** 73, 639-665.

125. Szymanski, W.; Beierle, J. M.; Kistemaker, H. A.; Velema, W. A.; Feringa, B. L. *Chem Rev* **2013,** 113, (8), 6114-78.

126. Bortolus, P.; Monti, S. *The Journal of Physical Chemistry* **1979,** 83, (6), 648-652.

127. Bléger, D.; Hecht, S. *Angewandte Chemie International Edition* **2015,** 54, (39), 11338-11349.

128. Mukhopadhyay, R. D.; Praveen, V. K.; Ajayaghosh, A. *Materials Horizons* **2014,** 1, (6), 572-576.

129. Wei, Y.-b.; Tang, Q.; Gong, C.-b.; Lam, M. H.-W. *Analytica Chimica Acta* **2015,** 900, 10-20.

130. Kumar, G. S.; Neckers, D. C. *Chemical Reviews* **1989,** 89, (8), 1915-1925.

131. Xie, S.; Natansohn, A.; Rochon, P. *Chemistry of Materials* **1993,** 5, (4), 403-411.

132. Pace, G.; Ferri, V.; Grave, C.; Elbing, M.; von Hänisch, C.; Zharnikov, M.; Mayor, M.; Rampi, M. A.; Samorì, P. *Proceedings of the National Academy of Sciences* **2007,** 104, (24), 9937-9942.

133. Mativetsky, J. M.; Pace, G.; Elbing, M.; Rampi, M. A.; Mayor, M.; Samorì, P. *Journal of the American Chemical Society* **2008,** 130, (29), 9192-9193.

134. Merino, E. *Chemical Society reviews* **2011,** 40, (7), 3835-3853.

135. Shinkai, S.; Minami, T.; Kusano, Y.; Manabe, O. *Journal of the American Chemical Society* **1983,** 105, (7), 1851-1856.

136. Jousselme, B.; Blanchard, P.; Gallego-Planas, N.; Delaunay, J.; Allain, M.; Richomme, P.; Levillain, E.; Roncali, J. *Journal of the American Chemical Society* **2003,** 125, (10), 2888-2889.

137. Cacciapaglia, R.; Di Stefano, S.; Mandolini, L. *Journal of the American Chemical Society* **2003,** 125, (8), 2224-2227.

138. Higuchi, M.; Minoura, N.; Kinoshita, T. *Colloid Polym Sci* **1995,** 273, (11), 1022-1027.

139. Heinz Dürr, H. B.-L. *Elsevier Science* **2003**.

140. Renner, C.; Moroder, L. *ChemBioChem* **2006,** 7, (6), 869 - 878.

141. Merino, E.; Ribagorda, M. *Beilstein Journal of Organic Chemistry* **2012,** 8, 1071-1090.

142. Enachescu, M.; Schleef, D.; Ogletree, D. F.; Salmeron, M. *Physical Review B* **1999,** 60, (24), 16913-16919.

143. Tatar, R. C.; Rabii, S. *Physical Review B* **1982,** 25, (6), 4126-4141.

144. Nilson, K.; Åhlund, J.; Shariati, M.-N.; Schiessling, J.; Palmgren, P.; Brena, B.; Göthelid, E.; Hennies, F.; Huismans, Y.; Evangelista, F.; Rudolf, P.; Göthelid, M.; Mårtensson, N.; Puglia, C. *The Journal of Chemical Physics* **2012,** 137, (4), 044708.

145. Kibsgaard, J.; Lauritsen, J. V.; Laegsgaard, E.; Clausen, B. S.; Topsøe, H.; Besenbacher, F. *J. Am. Chem. Soc.* **2006,** 128, 13950-13958.

146. Love, J. C.; Estroff, L. A.; Kriebel, J. K.; Nuzzo, R. G.; Whitesides, G. M. *Chemical Reviews* **2005,** 105, (4), 1103-1170.

147. Nuzzo, R. G. A., D. L. *J. Am. Chem. Soc.* **1983,** 105, 4481.

148. Kadantsev, E. S.; Hawrylak, P. *Solid State Communications* **2012,** 152, (10), 909-913.

149. Coehoorn, R.; Haas, C.; Dijkstra, J.; Flipse, C. J. F.; de Groot, R. A.; Wold, A. *Physical Review B* **1987,** 35, (12), 6195-6202.

150. Wilson, J. A.; Yoffe, A. D. *Advances in Physics* **1969,** 18, (73), 193-335.

151. RadisavljevicB; RadenovicA; BrivioJ; GiacomettiV; KisA. *Nat Nano* **2011,** 6, (3), 147-150.

152. Yin, Z.; Li, H.; Li, H.; Jiang, L.; Shi, Y.; Sun, Y.; Lu, G.; Zhang, Q.; Chen, X.; Zhang, H. *ACS Nano* **2012,** 6, (1), 74-80.

153. Sundaram, R. S.; Engel, M.; Lombardo, A.; Krupke, R.; Ferrari, A. C.; Avouris, P.; Steiner, M. *Nano Letters* **2013,** 13, (4), 1416-1421.

154. Schiffrin, A.; Paasch-Colberg, T.; Karpowicz, N.; Apalkov, V.; Gerster, D.; Muhlbrandt, S.; Korbman, M.; Reichert, J.; Schultze, M.; Holzner, S.; Barth, J. V.; Kienberger, R.; Ernstorfer, R.; Yakovlev, V. S.; Stockman, M. I.; Krausz, F. *Nature* **2013,** 493, (7430), 70-74.

155. Crivillers, N.; Liscio, A.; Di Stasio, F.; Van Dyck, C.; Osella, S.; Cornil, D.; Mian, S.; Lazzerini, G. M.; Fenwick, O.; Orgiu, E.; Reinders, F.; Braun, S.; Fahlman, M.; Mayor, M.; Cornil, J.; Palermo, V.; Cacialli, F.; Samorì, P. *Physical Chemistry Chemical Physics* **2011,** 13, (32), 14302-14310.

156. Crivillers, N.; Osella, S.; Van Dyck, C.; Lazzerini, G. M.; Cornil, D.; Liscio, A.; Di Stasio, F.; Mian, S.; Fenwick, O.; Reinders, F.; Neuburger, M.; Treossi, E.; Mayor, M.; Palermo, V.; Cacialli, F.; Cornil, J.; Samorì, P. *Advanced materials* **2013,** 25, (3), 432-436.

157. Looi, H. J.; Pang, L. Y. S.; Molloy, A. B.; Jones, F.; Foord, J. S.; Jackman, R. B. *Diamond and Related Materials* **1998,** 7, (2–5), 550-555.

158. Looi, H. J.; Whitfield, M. D.; Foord, J. S.; Jackman, R. B. *Thin Solid Films* **1999,** 343–344, 623-626.

159. Looi, H. J.; Pang, L. Y. S.; Foord, J. S.; Jackman, R. B. *Solid-State Electronics* **1998,** 42, (12), 2215-2223.

160. Nimmrich, M.; Kittelmann, M.; Rahe, P.; Mayne, A. J.; Dujardin, G.; von Schmidsfeld, A.; Reichling, M.; Harneit, W.; Kühnle, A. *Phys. Rev. B* **2010,** 81, 201403.

161. Bobrov, K.; Mayne, A.; Comtet, G.; Dujardin, G.; Hellner, L.; Hoffman, A. *Phys. Rev. B* **2003,** 68, 195416.

162. Lud, S. Q.; Niedermeier, M.; Koch, P. S.; Bruno, P.; Gruen, D. M.; Stutzmann, M.; Garrido, J. a. *Appl. Phys. Lett.* **2010,** 96, 92109.

163. Yu, J.; Liu, G.; Sumant, A. V.; Goyal, V.; Balandin, A. A. *Nano Lett.* **2012,** 12, 1603-1608.

164. Ma, Y.; Dai, Y.; Guo, M.; Huang, B. *Phys. Review. B* **2012,** 85, 235448.

165. Li, X.; Cai, W.; An, J.; Kim, S.; Nah, J.; Yang, D.; Piner, R.; Velamakanni, A.; Jung, I.; Tutuc, E.; Banerjee, S. K.; Colombo, L.; Ruoff, R. S. *Science* **2009,** 324, 1312-1314.

166. Evans, S. D.; Johnson, S. R.; Ringsdorf, H.; Williams, L. M.; Wolf, H. *Langmuir* **1998,** 14, (22), 6436-6440.

167. Klajn, R. *Pure Appl. Chem.* **2010,** 82, (12), 2247-2279.

168. Zhang, X.; Chen, T.; Chen, Q.; Wang, L.; Wan, L.-J. *J. Phys. Chem. Chem. Phys.* **2009,** 11, 7708-7712.

169. Theobald, J. A.; Oxtoby, N. S.; Phillips, M. A.; Champness, N. R.; Beton, P. H. *Nature* **2003,** 424, (6952), 1029-31.

170. Whitelam, S.; Tamblyn, I.; Haxton, T. K.; Wieland, M. B.; Champness, N. R.; Garrahan, J. P.; Beton, P. H. *Phys. Rev. X* **2014,** 4, (1), 011044.

171. Palma, C. A.; Samorì, P.; Cecchini, M. *J. Am. Chem. Soc.* **2010,** 132, (50), 17880-17885.

172. Palma, C. A.; Björk, J.; Bonini, M.; Dyer, M. S.; Llanes-Pallas, A.; Bonifazi, D.; Persson, M.; Samorì, P. *J. Am. Chem. Soc.* **2009,** 131, (36), 13062-71.

173. Wöll, D.; Braeken, E.; Deres, A.; De Schryver, F. C.; Uji-i, H.; Hofkens, J. *Chem. Soc. Rev.* **2009,** 38, (2), 313-28.

174. Chen, L.; Li, C.; Müllen, K. *J. Mater. Chem. C* **2014,** 2, (11), 1938.

175. Li, G.; Zhu, R.; Yang, Y. *Nature Photon.* **2012,** 6, (3), 153-161.

176. Nolde, F.; Qu, J. Q.; Kohl, C.; Pschirer, N. G.; Reuther, E.; Müllen, K. *Chem. Eur. J.* **2005,** 11, (13), 3959-3967.

177. Avlasevich, Y.; Li, C.; Müllen, K. *J. Mater. Chem.* **2010,** 20, (19), 3814-3826.

178. Würthner, F. *Pure Appl. Chem.* **2006,** 78, (12), 2341-2349.

179. Palma, C.-a.; Björk, J.; Bonini, M.; Dyer, M. S.; Llanes-pallas, A.; Bonifazi, D.; Persson, M.; Samorì, P. *J. Am. Chem. Soc.* **2009,** 131, 13062-13071.

180. Blunt, M. O.; Russell, J. C.; Gimenez-Lopez, M. D. C.; Taleb, N.; Lin, X.; Schröder, M.; Champness, N. R.; Beton, P. H. *Nat. Chem.* **2011,** 3, 74-78.

181. Teyssandier, J.; Battaglini, N.; Seydou, M.; Anquetin, G.; Diawara, B.; Sun, X.; Maurel, F.; Lang, P. *J. Phys. Chem. C* **2013,** 117, 8737-8745.

182. Karmel, H. J.; Chien, T.; Demers-Carpentier, V.; Garramone, J. J.; Hersam, M. C. *J. Phys. Chem. Lett.* **2014,** 5, 270-274.

183. Wang, Q. H.; Hersam, M. C. *Nat. Chem.* **2009,** 1, 206-211.

184. Jarvinen, P.; Hamalainen, S. K.; Banerjee, K.; Hakkinen, P.; Ijas, M.; Harju, A.; Liljeroth, P. *Nano Lett.* **2013,** 13, 3199-3204.

185. Li, B.; Tahara, K.; Adisoejoso, J.; Vanderlinden, W.; Gendt, S. D.; Tobe, Y.; Feyter, S. D. *ACS nano* **2013,** 7, 10764-10772.

186. Cisternas, E.; Stavale, F.; Flores, M.; Achete, C.; Vargas, P. *Phys. Rev. B* **2009,** 79, 205431.

187. Allen, M. J.; Tung, V. C.; Kaner, R. B. *Chem. Rev.* **2010,** 110, 132-145.

188. Park, S.-I.; Quate, C. F. *Appl. Phys. Lett.* **1986,** 48, 112-114.

189. Childress, L.; Dutt, M. V. G.; Taylor, J. M.; Zibrov, A. S.; Jelezko, F.; Wrachtrup, J.; Hemmer, P. R.; Lukin, M. D. *Science* **2006,** 314, 281-285.

190. Hartl, A.; Schmich, E.; Garrido, J. A.; Hernando, J.; Catharino, S. C. R.; Walter, S.; Feulner, P.; Kromka, A.; Steinmuller, D.; Stutzmann, M. *Nat. Mater.* **2004,** 3, 736-742.

191. Wu, Y.; Lin, Y. M.; Bol, A. A.; Jenkins, K. A.; Xia, F.; Farmer, D. B.; Zhu, Y.; Avouris, P. *Nature* **2011,** 472, 74-78.

192. Garrido, J. A.; Härtl, A.; Dankerl, M.; Reitinger, A.; Eickhoff, M.; Helwig, A.; Müller, G.; Stutzmann, M. *J. Am. Chem. Soc.* **2008,** 130, 4177-4181.

193. Vlachopoulos, N.; Liska, P.; Augustynski, J.; Gratzel, M. *J. Am. Chem. Soc.* **1988,** 110, (4), 1216-1220.

194. Oregan, B.; Gratzel, M. *Nature* **1991,** 353, (6346), 737-740.

195. Park, H.; Park, J.; Lim, A. K. L.; Anderson, E. H.; Alivisatos, A. P.; McEuen, P. L. *Nature* **2000,** 407, (6800), 57-60.

196. Gerster, D.; Reichert, J.; Bi, H.; Barth, J. V.; Kaniber, S. M.; Holleitner, A. W.; Visoly-Fisher, I.; Sergani, S.; Carmeli, I. *Nature Nanotech.* **2012,** 7, (10), 673-676.

197. Rabe, J. P.; Buchholz, S. *Science* **1991,** 253, (5018), 424-7.

198. Teyssandier, J.; Battaglini, N.; Seydou, M.; Anquetin, G.; Diawara, B.; Sun, X.; Maurel, F.; Lang, P. *The Journal of Physical Chemistry C* **2013,** 117, (17), 8737-8745.

199. Huang, S.; Ling, X.; Liang, L.; Song, Y.; Fang, W.; Zhang, J.; Kong, J.; Meunier, V.; Dresselhaus, M. S. *Nano Lett.* **2015,** 15, (5), 2892–2901.

200. Würthner, F.; Stepanenko, V.; Chen, Z. J.; Saha-Moller, C. R.; Kocher, N.; Stalke, D. *J. Org. Chem.* **2004,** 69, (23), 7933-7939.

201. Pschirer, N. G.; Kohl, C.; Nolde, T.; Qu, J. Q.; Müllen, K. *Angew. Chem. Int. Ed. Eng.* **2006,** 45, (9), 1401-1404.

202. Chen, Z. J.; Stepanenko, V.; Dehm, V.; Prins, P.; Siebbeles, L. D. A.; Seibt, J.; Marquetand, P.; Engel, V.; Würthner, F. *Chem. Eur. J.* **2007,** 13, (2), 436-449.

203. Spano, F. C. *Acc. Chem. Res.* **2010,** 43, (3), 429-439.

204. Weigand, R.; Rotermund, F.; Penzkofer, A. *J. Phys. Chem. A* **1997,** 101, (42), 7729-7734.

205. Nijhuis, C. A.; Reus, W. F.; Siegel, A. C.; Whitesides, G. M. *J. Am. Chem. Soc.* **2011,** 133, (39), 15397-15411.

206. Nijhuis, C. A.; Reus, W. F.; Barber, J. R.; Whitesides, G. M. *J. Phys. Chem. C* **2012,** 116, (26), 14139-14150.

207. Giovannetti, G.; Khomyakov, P.; Brocks, G.; Karpan, V.; van den Brink, J.; Kelly, P. *Phys. Rev. Lett.* **2008,** 101, (2), 026803.

208. Srisonphan, S.; Jung, Y. S.; Kim, H. K. *Nature Nanotech.* **2012,** 7, (8), 504-8.

209. Gregg, B. A. *J. Phys. Chem. B.* **2003,** 107, (20), 4688-4698.

210. Llanes-Pallas, A.; Palma, C. A.; Piot, L.; Belbakra, A.; Listorti, A.; Prato, M.; Samorì, P.; Armaroli, N.; Bonifazì, D. *J. Am. Chem. Soc.* **2009,** 131, (2), 509-20.

211. Reece, S. Y.; Nocera, D. G. *Annu. Rev. Biochem.* **2009,** 78, 673-699.

212. Gorenflot, J.; Sperlich, A.; Baumann, A.; Rauh, D.; Vasilev, A.; Li, C.; Baumgarten, M.; Deibel, C.; Dyakonov, V. *Synth. Met.* **2012,** 161, (23-24), 2669-2676.

213. Imahori, H.; Fukuzumi, S. *Adv. Func. Mat.* **2004,** 14, (6), 525-536.

214. Carmeli, I.; Frolov, L.; Carmeli, C.; Richter, S. *J. Am. Chem. Soc.* **2007,** 129, (41), 12352.

215. Bernardi, M.; Palummo, M.; Grossman, J. C. *Nano Lett.* **2013,** 13, (8), 3664-3670.

216. Lee, C. H.; Lee, G. H.; van der Zande, A. M.; Chen, W. C.; Li, Y. L.; Han, M. Y.; Cui, X.; Arefe, G.; Nuckolls, C.; Heinz, T. F.; Guo, J.; Hone, J.; Kim, P. *Nature Nanotechnol.* **2014,** 9, (9), 676-681.

217. Cechal, J.; Matlocha, T.; Polcak, J.; Kolibal, M.; Tomanec, O.; Kalousek, R.; Dub, P.; Sikola, T. *Thin Solid Films* **2009,** 517, (6), 1928-1934.

218. Shieh, J. T.; Liu, C. H.; Meng, H. F.; Tseng, S. R.; Chao, Y. C.; Horng, S. F. *J. Appl. Phys.* **2010,** 107, (8), 084503.

219. Margapoti, E.; Strobel, P.; Asmar, M. M.; Seifert, M.; Li, J.; Sachsenhauser, M.; Ceylan, Ö.; Palma, C.-A.; Barth, J. V.; Garrido, J. A.; Cattani-Scholz, A.; Ulloa, S. E.; Finley, J. J. *Nano Letters* **2014,** 14, (12), 6823-6827.

220. Das, S.; Chen, H.-Y.; Penumatcha, A. V.; Appenzeller, J. *Nano Letters* **2013,** 13, (1), 100-105.

221. Dolui, K.; Rungger, I.; Sanvito, S. *Physical Review B* **2013,** 87, (16), 165402.

222. Li, H.; Zhang, Q.; Yap, C. C. R.; Tay, B. K.; Edwin, T. H. T.; Olivier, A.; Baillargeat, D. *Advanced Functional Materials* **2012,** 22, (7), 1385-1390.

223. Lee, C.; Yan, H.; Brus, L. E.; Heinz, T. F.; Hone, J.; Ryu, S. *ACS Nano* **2010,** 4, (5), 2695-2700.

224. Seo, S.; Min, M.; Lee, S. M.; Lee, H. *Nat Commun* **2013,** 4, 1920.

225. Kornilovitch, P. E.; Bratkovsky, A. M.; Stanley Williams, R. *Physical Review B* **2002,** 66, (16), 165436.

226. Brütting, W.; Berleb, S.; Mückl, A. G. *Organic Electronics* **2001,** 2, (1), 1-36.

227. Baghbanzadeh, M.; Simeone, F. C.; Bowers, C. M.; Liao, K.-C.; Thuo, M.; Baghbanzadeh, M.; Miller, M. S.; Carmichael, T. B.; Whitesides, G. M. *Journal of the American Chemical Society* **2014,** 136, (48), 16919-16925.

228. Liu, N.; Chen, Z.; Dunphy, D. R.; Jiang, Y.-B.; Assink, R. A.; Brinker, C. J. *Angewandte Chemie International Edition* **2003,** 42, (15), 1731-1734.

229. Jariwala, D.; Sangwan, V. K.; Wu, C.-C.; Prabhumirashi, P. L.; Geier, M. L.; Marks, T. J.; Lauhon, L. J.; Hersam, M. C. *Proceedings of the National Academy of Sciences* **2013,** 110, (45), 18076-18080.

230. Sutar, S.; Agnihotri, P.; Comfort, E.; Taniguchi, T.; Watanabe, K.; Ung Lee, J. *Applied Physics Letters* **2014,** 104, (12), 122104.

231. Stokbro, K.; Taylor, J.; Brandbyge, M. *Journal of the American Chemical Society* **2003,** 125, (13), 3674-3675.

232. Aviram, A.; Ratner, M. A. *Chemical Physics Letters* **1974,** 29, (2), 277-283.

233. Y. T. Gonzalez, C. E. G., B. J. Robinson, N. D. Kay, O. Kolosov, O. Kazakova. *www.npl.co.uk/publications/science-posters (accessed January 2015).*

234. Haynes, W. M. *CRC Press: Boca Raton, FL* **2006**.

235. Li, J.; Wierzbowski, J.; Ceylan, Ö.; Klein, J.; Nisic, F.; Anh, T. L.; Meggendorfer, F.; Palma, C.-A.; Dragonetti, C.; Barth, J. V.; Finley, J. J.; Margapoti, E. *Applied Physics Letters* **2014,** 105, (24), 241116.

236. Margapoti, E.; Li, J.; Ceylan, Ö.; Seifert, M.; Nisic, F.; Anh, T. L.; Meggendorfer, F.; Dragonetti, C.; Palma, C.-A.; Barth, J. V.; Finley, J. J. *Advanced materials* **2015,** 27, (8), 1426-1431.

237. Theobald, J. A.; Oxtoby, N. S.; Phillips, M. A.; Champness, N. R.; Beton, P. H. *Nature* **2003,** 424, (6952), 1029-1031.

238. Stepanow, S.; Lingenfelder, M.; Dmitriev, A.; Spillmann, H.; Delvigne, E.; Lin, N.; Deng, X.; Cai, C.; Barth, J. V.; Kern, K. *Nat Mater* **2004,** 3, (4), 229-233.

239. Barth, J. V. *Annual Review of Physical Chemistry* **2007,** 58, (1), 375-407.

List of Figures

List of Publications

1. Sarah Wieghold, Juan Li (co-first author), Patrick Simon, Maximilian Krause, Yuri Avlasevich, Chen Li, Jose A. Garrido, Ueli Heiz, Paolo Samorí, Klaus Müllen*, Friedrich Esch*, Johannes V. Barth*, Carlos-Andres Palma*, Photoresponse of supramolecular self-assembled networks on graphene-diamond interfaces, ***Nat. Commun.***, 2016, 7:10700.
2. Juan Li, Sarah Wieghold, Murat Anil Öner, Patrick Simon, Moritz V. Hauf, Emanuela Margapoti, Jose A. Garrido, Friedrich Esch, Carlos-Andres Palma*, Johannes V. Barth*, Three-dimensional bicomponent supramolecular nanoporous self-assembly on a hybrid all-carbon atomically flat and transparent platform, ***Nano Lett.***, 2014, 14 (8), 4486- 4492.
3. Juan Li, Jakob Wierzbowski, Özlem Ceylan, Julian Klein, Filippo Nisic, Tuan Le Anh, Felix Meggendorfer, Carlos-Andres Palma, Claudia Dragonetti, Johannes V. Barth, Jonathan J. Finley, Emanuela Margapoti*, Tuning the optical emission of MoS_2 nanosheets using proximal photoswitchable azobenzene molecules, ***Appl. Phys. Lett.***, 2014, 105, 241116.
4. Emanuela Margapoti*, Juan Li, Özlem Ceylan, Max Seifert, Filippo Nisic, Tuan Le Anh, Felix Meggendorfer, Claudia Dragonetti, Carlos-Andres Palma*, Johannes V. Barth, Jonathan J. Finley, A 2D semiconductor–self-assembled monolayer photoswitchable diode, ***Adv. Mater.***, 2015, 27, 1426-1431.
5. Emanuela Margapoti*, Philipp Strobel, Mahmoud M. Asmar, Max Seifert, Juan Li, Matthias Sachsenhauser, Özlem Ceylan, Carlos-Andres Palma, Johannes V. Barth, Jose A. Garrido, Anna Cattani-Scholz, Sergio E. Ulloa, Jonathan J. Finley, Emergence of photoswitchable states in a graphene-azobenzene-Au platform, ***Nano Lett.***, 2014, 14 (12), 6823–6827.

Acknowledgements

First of all, I would like to thank Prof. Dr. Johannes V. Barth for giving me the opportunity to work at E20 in this interesting and interdisciplinary field. Your kindly support and suggestions made me self-confident and helped me a lot in the new realm. Many thanks also to my supervisor Dr. Carlos-Andres Palma, for your countless discussions and advices at any time during my PhD study. I am really affected by your encyclopedic knowledge and enthusiasm for science. I am very thankful to Prof. Dr. Jonathan J. Finley for offering me the collaboration opportunity to work in your group at the Walter Schottky Institut. I am extremely thankful to Dr. Emanuela Margapoti. Thank you for your theoretical guidance and always helping me to solve any problems from experiments and administrational trivia when I was an interim member at E24. I would also thank Dr. Friedrich Esch and Dr. Jose A. Garrido being our collaborators for scientific supports and discussions.

Furthermore, I would like to thank Sarah Wieghold for your good scientific discussions and the pleasant time we worked together. Many thanks to Patrick Simon for your selfless and friendly help. Thanks to Dr. Özge Sağlam for discussing some problems of device fabrication. Thanks the people from my office, Alissa, Felix, Martin, Li, Bodong, Chao, for all your warmly help and mental support. I am grateful to my colleagues and friends, Peng, Wei, Yuxiang, Yuanyuan, Yuanqin, Yinying, Xumin, thank you all for sharing the good discussions, nice conference experiences and the enjoyable time with me.

I am very thankful to Viktoria Blaschek, Max Glanz, Karl Eberle and Karl Kölbl for the administrational and technical support. Thanks for all of your constant and prompt help.

Finally, I specially want to thank my family. To my parents, your infinite love and support is the most valuable treasure in my life. To my boyfriend, Dr. Canyang Zhang, thank you for your love, understanding and always believing in me and encouraging me. Every people of my whole family, thanks all for supporting and trusting me in these years.